nucleartechnology®

CONTENTS / JUNE 1978—VOL. 39, NO. 1

(Continued)

CONTENTS / JUNE 1978–VOL. 39, NO. 1

(Continued)

ANALYSIS

DEPARTMENT

AUTHORS — JUNE 1978

ENERGY MODELING AND FORECASTING

ENERGY FORECASTING IN THE PREPARATION OF FRENCH PLAN VII

Marc Alinhac

Marc Alinhac (Hautes Etudes Commerciales, Paris, 1967) is currently an economist under the general direction of Electricité de France (Paris). His current research interests are in the economy of electricity and energy forecasting methodology. He has worked on various scenarios of energy consumption for the years 1985 and 2000.

ENERGY MODELING AND FORECASTING AT THE U.S. ENERGY RESEARCH AND DEVELOPMENT ADMINISTRATION

Richard H. Williamson
Edward J. Hanrahan

Richard H. Williamson (top) (PhD expected, economics, North Carolina State University, 1978) is deputy associate director for program analysis in the U.S. Department of Energy (DOE) Office of Energy Research. Previously, he directed the energy systems analysis and modeling efforts for the U.S. Energy Research and Development Administration (ERDA). His current interests are energy planning, research and development strategies, and energy technology commercialization. **Edward J. Hanrahan** (MS, nuclear engineering, New York University, 1963) is director of fuel cycle evaluation in the Nuclear Energy Office at DOE. Previously, he directed the Office of Analysis in ERDA. His current interests are nuclear fuel cycles and nonproliferation alternatives.

NUCLEAR SAFETY ANALYSIS

RISK ANALYSIS OF RADIOACTIVE WASTE MANAGEMENT SYSTEMS IN GERMANY

Hans J. Wingender

Hans Joerg Wingender (doctor, nuclear physics, Goethe Universität, Frankfurt, 1971) has studied at Goettingen, Bonn, and Frankfurt. He is head of the Safety Technology Group in the Department of Nuclear Engineering of NUKEM Company, Hanau, Federal Replublic of Germany (FRG). His current interest is the efficacy of safety engineering. As a member of the project management, he is involved in a project for the risk analysis of the waste management facilities planned for the nuclear center in the FRG.

CONTRIBUTIONS TO THE RISK EVALUATION OF A HIGH-LEVEL WASTE SOLIDIFICATION PLANT

H. Brücher

Heiner Brücher (doctor, nuclear engineering, Technical University of Aachen, 1977) has worked at the Nuclear Research Center at Jülich since 1974. His interests include safety-related investigations in the light water reactor fuel cycle with emphasis on high-level waste treatment. At present, he is conducting conceptual design and risk analyses of separation, storage, and final disposal of radioactive ^{85}Kr, as well as tritium treatment.
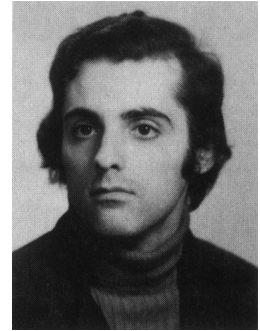
REACTORS

TRANSIENT ANALYSES OF A 1000-MW GAS-COOLED FAST REACTOR

Dirk Wilhelm

Dirk Wilhelm (Dipl. Ing., mechanical engineering, Technical University of Munich, 1969; PhD, mechanical engineering, Technical University of Karlsruhe, 1976) has been a research scientist since 1969 at the Institut für Neutronenphysik und Reaktortechnik of Kernforschungszentrum Karlsruhe. He works on safety studies for the gas-cooled fast breeder reactor, with special interest in the development of computer codes for transient analyses.

CONTAINMENT NEGATIVE PRESSURE EVALUATION

Stephen W. Webb

Stephen W. Webb (BS, mechanical engineering, Clarkson College, 1971; MS, nuclear engineering, Pennsylvania State University, 1972) has been engaged in thermal-hydraulic analysis of nuclear power plants as the thermofluid staff specialist in the Applied Engineering Analysis Department of Gilbert Associates, Inc. His interests include thrust and jet impingement analysis, subcompartment pressurization modeling, and containment accident analysis techniques.
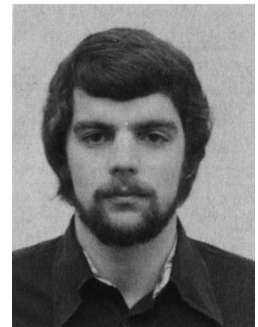
FUEL CYCLES

OPTIMUM FUEL LOADING AND OPERATION PLANNING FOR LIGHT WATER REACTOR POWER STATIONS. PART I: PRESSURIZED WATER REACTOR CASE STUDY

Tsutomu Hoshino

Tsutomu Hoshino (Dr. Eng., electrical engineering, Kyoto University, 1967) is an associate professor at Institute of Atomic Energy, Kyoto University. Since 1960, including his stay at the Institutt for Atomenergi, Kjeller, Norway (1971-1972) as a postdoctrate fellow of NTNF, he has been engaged in research on nuclear reactor dynamics, control, and optimization problems. His current interests include planning and optimization of nuclear energy systems and computer applications.
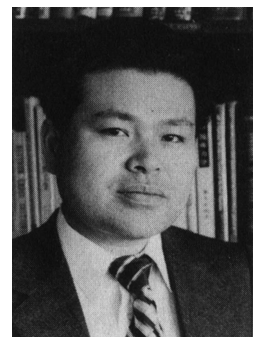
ELECTROCHEMICAL EXTRACTION OF HYDROGEN FROM MOLTEN LiF-LiCl-LiBr AND ITS APPLICATION TO LIQUID-LITHIUM FUSION REACTOR BLANKET PROCESSING

W. F. Calaway

Wallis F. Calaway (BA, chemistry, The College of Wooster, 1970; PhD, chemical physics, Indiana University, 1975) has been an assistant research chemist in the Chemical Engineering Division of Argonne National Laboratory since 1975. His present interests include the thermodynamics and physical chemistry of liquid-metal systems, and liquid-lithium purification as applied to fusion reactor blankets.

CORROSION AND MECHANICAL BEHAVIOR OF IRON IN LIQUID LITHIUM

T. A. Whipple
D. L. Olson
W. L. Bradley
D. K. Matlock

Thomas A. Whipple (top right) (MS, metallurgical engineering, Colorado School of Mines, 1976) is an assistant engineer with Westinghouse Electric Corporation. He is interested in mechanical metallurgy and testing. **David L. Olson** (top left) (PhD, materials sc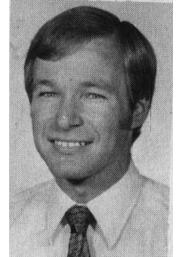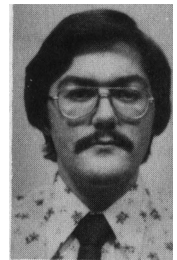ience, Cornell University, 1970) is associate professor at the Colorado School of Mines. He performs research in corrosion and welding metallurgy. **Walter L. Bradley** (bottom right) (PhD, materials science, University of Texas, 1969) is associate professor at Texas A&M University. He is involved with research in the areas of mechanical behavior of materials and phase transformation. **David K. Matlock** (bottom left) (PhD, materials science, Stanford University, 1972) is associate professor at the Colorado School of Mines. He performs research in mechanical metallurgy and forming processes.

EUROPIA AS A NUCLEAR CONTROL MATERIAL

Paul C. S. Wu

Paul C. S. Wu (PhD, metallurgy, Iowa State University, 1972) worked at Ames Laboratory from 1967 to 1972 in the areas of sodium technology and nuclear materials. He has been with the Westinghouse Advanced Reactors Division since 1972, working in the areas of liquid-metal fast breeder reactor (LMFBR) related materials development programs, especially the high-temperature mechanical behaviors of LMFBR structural alloys. His current interests are in the areas of material problems in an LMFBR fuel reprocessing plant.
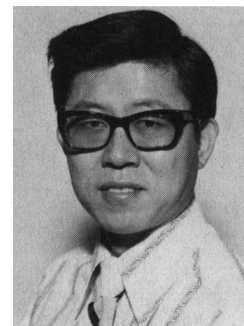
ANALYSIS OF FISSILE MATERIALS BY CYCLIC ACTIVATION OF DELAYED NEUTRONS

John M. Jamieson
Geoffrey G. Eichholz

John M. Jamieson (top) (PhD, nuclear engineering, Georgia Institute of Technology, 1976) has been chief engineer at Technical Analysis Corporation since 1974, in charge of engineering development of computer systems for various technical applications. **Geoffrey G. Eichholz** (PhD, physics, University of Leeds, 1948) is regents' professor of nuclear engineering at the Georgia Institute of Technology, where he has conducted research over a broad spectrum of radiation technology, including radiation detectors, radiotracer methodology, environmental aspects of nuclear power, and radiation effects on materials.

ENERGY FORECASTING IN THE PREPARATION OF FRENCH PLAN VII

MARC ALINHAC *Electricité de France, General Economic Studies*
2, rue Louis Murat, 75008 Paris, France

In the framework of the procedure governing the preparation and adjustment of France's Plan VII, which is scheduled to cover the period from 1976 to 1980, an energy committee was appointed by the French government to survey the main lines of the energy policy from now until 1985, based on guidelines laid down in early 1975 by the government.

The committee elaborated forecasts for 1985 and 2000 and, on this basis, developed propositions for an energy policy whose main features are a high energy savings program and an important development of nuclear energy.

INTRODUCTION

A reexamination of France's long-term energy requirements was called for by the new energy and economic environment that now has a heavy influence in Europe and in the world. They are

1. on the one hand, the sudden boost in the price of oil and its repercussions, not only on the energy economy—more particularly, in connection with the relative costs of the various energies—but also on the nation's economy in general (balance of payments, inflation problems, and the like)

2. on the other hand, the existence of persistent economic unbalances within the international economy (monetary system) and within France itself (reduced growth trends, problems of unbalances in external trade, and preservation of the nation's energy and technological independence, etc.).

FORECASTING METHODS AND CRITERIA

Main Criteria

In the first place, the overall framework of the forecasting procedure was laid down by a number of *criteria* governing the energy policy, of which some of the main ones are

1. minimizing the overall cost of the energy policy for the economy, with particular attention to the problem of financing the capital investment

2. aiming at the least possible dependence, both political and economic, with respect to other countries and the safeguarding of the supply sources

3. ecological and social aspects of the energy development.

Two-Fold Approach

For 1985, the energy committee, working under the auspices of France's Plan VII, based its energy projections on an analysis of the results of the year 1975 and an attempt at forecasting demand for the year 2000. The 1985 forecast, in turn, consisted of a dual approach to energy requirements, one global and the other analytical.

Global Approach

This was based on (a) 1974 as reference year, and (b) the growth curve taken into account in the calculation of Plan VII, that is, a growth in the Gross National Product (GNP) of 5.5% per annum during 1975 to 1980 and 5.0% per annum during 1980 to 1985.

1. It is assumed that energy demand will grow in proportion to the growth in the GNP. This leads to a

consumption figure of 285 million oil-equivalent tons (oet) for 1985, which is an upper limit to conceivable consumption, since it represents an elasticity of 1, meaning a growth rate with constant parameters without any particular tendency toward energy savings. (In practice, no country has an elasticity greater than 1.)

2. The economy's "intrinsic requirements" of 285 million oet will then have to be covered

    a. in part by effective consumption of primary energy

    b. in part by energy savings.

The share of each of the above terms will then depend on *the cost of energy in 1985*. The higher the cost of energy, the greater the required energy savings (see Fig. 1).

3. Supposing a price level requiring very great energy savings, plus an appropriate voluntary policy, a "minimum load" of energy consumption is laid down, below which it is not feasible to drop. This then is the bottom limit of the spread based on the assumption of high energy costs. The minimum load is estimated to be 232 million oet.

4. Moreover, the state Agency for Energy Savings (in French, AEE) has meanwhile identified fairly accurately a certain volume of savings achievable between 1974 and 1985 without prejudice to national growth. The amount of these is estimated at 45 million oet, of which 5 million were achieved in
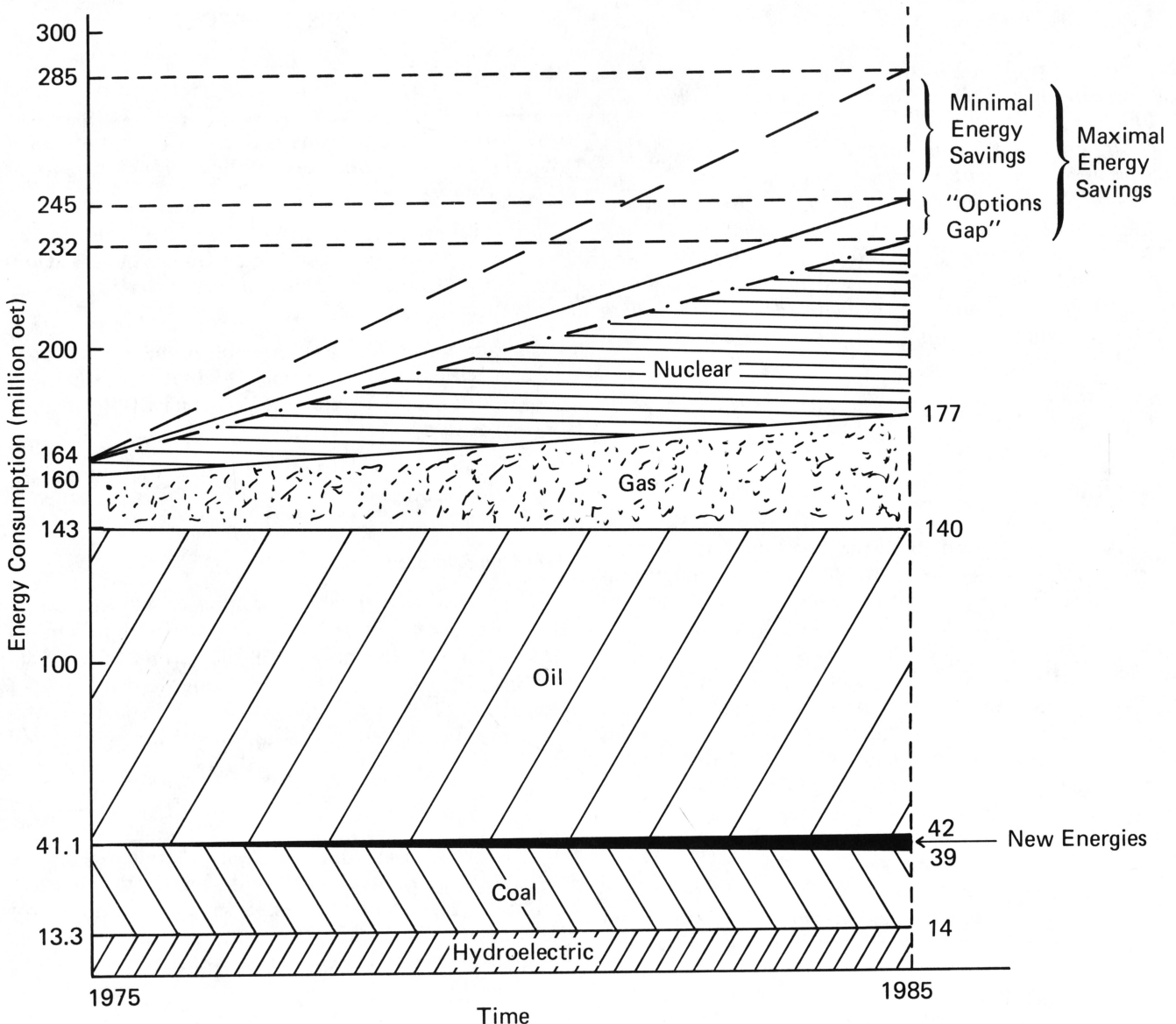

Fig. 1. Primary energy forecast for 1985.

1975. Consequently, we have to achieve 40 million oet in energy savings from now until 1985.

5. Given the above, the *upper limit* of the range will come to 285 − 40 = 245 million oet. The interval between the bottom limit and that upper limit (namely, 13 million oet) is known as the "options gap" or "adjustable increment." It will have to be spread out among the various forms of energy and the energy savings, depending on the effective energy supply costs.

Analytical Approach

This consisted in surveying each of the major sectors of consumption: steelmaking, industrial (except steelmaking), residential, commercial, and transportation.

1. *Steelmaking* was the subject of a separate and relatively more detailed approach in conjunction with the trade. The approach consisted first in determining the likely specific consumption per ton of steel between now and 1985, under the impact of new technologies, and second, in taking into account the assumed production that year, compatible with the overall growth trends in the economy.

2. In *industry*, two assumptions were made:

   a. first, a continuation of the trend of decreasing consumption per unit of production at its former rate (minus 10% in ten years)

   b. second, an acceleration of that reduction through a policy of technical progress that would foster energy saving (minus 25% in the next ten years, instead of 10%).

3. Regarding *residential and commercial* requirements, their appraisal took into account the energy savings anticipated to result from regulations governing the insulation of new buildings published by the French government in March 1974; the required reduction in the average heating temperature in apartments and buildings (not more than 20°C); and, lastly, various assumptions made about technical advances, leading to economizing energy in existing residences (for example, heat pump).

4. Finally, as to *transportation*, high and low assumptions on energy savings according to the growth in economic activity were studied whereby the transports of goods and of persons were kept strictly apart.

Comparison

This second approach allowed a comparison with the global figure, which determined the safety margins available in each sector; these margins should contribute toward meeting the targets defined above.

Planning Procedure

This so far has taken place in two phases, as indeed for the preparation of the plan itself:

1. First, the committee identified the *major* lines of the energy policy, and specified the *choice criteria* the policy had to observe. At the same time, it investigated the problems of compatibility between overall growth and energy consumption, between a call for one or another energy resources and national independence, etc.

2. During the second phase, the forecasts were discussed again and "action orientations" were set forth, mainly consisting of "priority action programs."

Problems of Equivalence

Before submitting the results, it should be noted that in France, failing precise data on all of the equivalences between effective energies at the consumption level, we accept the following at the *production* level: 1000 kWh = 0.222 oet.

RESULTS: THE OUTLOOK FOR 1985

Major Assumptions

1. Economic growth: 5.5% of the GNP during 1976 to 1980 and 5.0% of the GNP during 1980 to 1985.

2. Cost of fuels: US $8 to $12 per barrel of oil equivalent, i.e., at $1 = FF 4.50, FF 280 to 420 per ton crude CIF (on January 1, 1976).

3. Electricity = *decrease* in average production cost per kWh starting in 1980, resulting from the growing contribution of nuclear power (with lower costs) to electrical production.

Consumption Forecasts

Consumption by Sector

Tables I, II, and III list energy consumption data.

Primary Energy Consumption by Energy Source

As we saw earlier, the committee identified overall a minimum load of 232 million oet and an "adjustable increment" of 13 million oet. Thus, the strategy suggested by the committee covered the following:

1. First, the requirement not to exceed 245 million oet, involving a minimum energy saving effort of 40 million oet (which is already a stiff figure if one considers that the

TABLE I

Consumption in 1975 by the Consumer Sector

(Corrected for Climate)

	Million oet		
	1975	Savings Made in 1975[a]	(1974)
Steel industry	12.8	---	(15.7)
Industrial (except steel)	42.5	---	(47.2)
Residential, commercial, and agricultural	56.7	9.5	(59.6)
Transportation	31.4	1.5	(30.9)
Energy conversions and losses	21.0	1.5	(22.2)
Total	164.4	12.5	175.6

[a]Compared with energy savings trends prior to the oil crisis, corrected to take account of effective trends in economic activity.

TABLE II

Consumption Forecasts for the Year 2000 According to a High and a Low Assumption for Economic Development

	Million oet	
	High	Low
Industrial and steelmaking	135	107
Residential, commercial, and agricultural	147	128
Transportation, including bunkers	78	67
Final demand	360	302
Producers, conversions, and losses	40	33
Primary energy input	400	335

TABLE III

Consumption Forecast for 1985

	Million oet
Steelmaking	16.8
Industrial	63.0
Residential, commercial, and agricultural	83.7
Transportation	44
Final demand	207.5
Energy conversions and losses	24.5
Primary energy input	232.0

energy consumption in France per inhabitant, or per dollar of GNP, is already one of the lowest among the industrial countries).

2. Second, the necessity to immediately set up the required provisioning of the minimum load of 232 million oet.

Strategy Relating to Each Energy Source

As Table IV shows, the main thrust of the strategy is the development of nuclear energy. This essential direction will be accompanied by the stabilization of both coal and oil consumption, a strong upturn in gas consumption (mainly imported gas from various countries), and the beginning of not unimportant developments in new energy forms.

Nuclear Penetration

The strategy will be powerfully backed up by the development of nuclear power plants for the generation of electricity; indeed, the outlets for nuclear energy other than electrical will remain small in 1985. The committee is hopeful, however, that the progress of electricity will take place "in the observance of the overall necessity for saving energy and at a rate that will not tend to render more difficult the development of new forms of energy."

With regard to electricity production, the committee estimates that despite some pressure toward higher costs, the competitiveness of nuclear energy will be assured for the greatest share of the production of electricity. The development of the nuclear sector is targeted to obtain an optimum population of power stations in 1985 [that means, according to the tarification theory used by Electricité de France (EdF), a population in which the short-term marginal cost equals the long-term marginal cost]. In any

TABLE IV

Proposed Breakdown Between Energy Forms Based on Criteria Laid Down by the Committee

	1975		1985 Minimum Load	
	Million oet	%	Million oet	%
Coal	28	17	25	11
Gas	17	10.5	37	16
Oil	102	62	98	42
Nuclear	4	2.5	55	24
Hydroelectric	13	8	14	6
New energy forms	---	---	3	1
Total	164	100	232	100

event, up to that date, the development costs of nuclear energy will have remained below the marginal cost of conventional thermal stations.

The committee estimates that this optimum will come to around 55 million oet, equivalent to 247.5 TWh, against a total electricity consumption of 365 TWh (compared with 181 TWh in 1975).

Development of Other Energy Sources

1. For *coal*, the suggested figure presupposes some redeployment of coal in industry, but takes into account the specific difficulties in using this fuel and of a slowing down in the use of thermal stations after 1980.

2. The committee reaffirms the interest there is in sustained growth of *gas*, but proposes that supplies are adequate for a genuine diversification and that increased safety can be achieved by the installation of strategic underground reservoirs.

3. With regard to *oil*, the committee puts forward a figure that corresponds, for the "white" products, to the uppermost limit of the feasible effort at energy saving, and, for the "black" products, that avoids excessive unbalance of the refining structure. However, this trend raises a two-fold problem in France's oil sector:

   a. First, there is likely to remain a permanent refining overcapacity with respect to needs. (French refineries can currently process some 160 million tons of crude annually.)

   b. Next, the reconversion of the refining capabilities—more white products, less black ones—poses fresh problems of financing over the coming years. (Today the share of fuel as such is only 13% of the French oil balance sheet.)

4. As to *new energy forms*, mainly geothermal and solar, the target set presupposes a voluntary development policy for such new energies.

Capital Spending During the Period of Plan VII

The full extent of France's "energy mutation" is evident in the size of the investments provided for on the nation's territory during the period of Plan VII. The overall capital outlay will amount to FF 130 billion, meaning an increase of 45% as compared with that of Plan VI (which covered the years from 1971 to 1975). Thus, during the life of Plan VII, the energy sector should average around 9 to 10% of the overall investments made by the nonfinancial firms, as against 7 to 8% during Plan VI.

Investment in the electricity and nuclear energy sector should grow by over 75%; that for coal and gas will also increase considerably. And to foster energy saving, the appropriate investment will amount to FF 10 billion.

As regards oil, investment in France will decrease appreciably despite the setting up of conversion plants in the refining industry. But in this sector, the increased costs of prospection and development will remain located mostly outside of France, and will involve spending on the order of FF 45 billion by the French oil groups during Plan VII.

Priority Action Programs

In the concluding part of its work, the committee was led to examine what actions it would be necessary to include in the "priority action programs" covered in Plan VII, whatever the effects of possible fluctuations in the economic situation.

The committee considered that the choice of energy priority programs should be aimed to enable the energy policy to move away from its present tendencies and be oriented toward the new targets. The program of light water nuclear plants, the development of which is in any case the major element of Plan VII in the energy sector, is now considered to be launched. Hence four "priority actions" are now proposed:

1. energy saving, by placing stress on operations of demonstration and by the appropriate capital outlay to back these up

2. developing the technology of hydrocarbon prospection and operation in offshore areas, more particularly by pursuing the deep water program already launched

3. developing the future nuclear plants, especially those of the breeder reactor type

4. developing the technology of new energy forms (solar, hydrogen, and heat upgrading, and especially the direct utilization of nuclear heat).

ENERGY MODELING AND FORECASTING AT THE U.S. ENERGY RESEARCH AND DEVELOPMENT ADMINISTRATION

RICHARD H. WILLIAMSON and EDWARD J. HANRAHAN
U.S. Department of Energy
Office of the Assistant Administrator for Planning and Analysis
Washington, D.C. 20545

The application of a combined set of energy and economic models describing the complex interactions of the nation's energy system improved the planning processes at the U.S. Energy Research and Development Administration for new technology development. The models include econometric techniques for macroeconomic projections, input-output techniques for sector detail, linear programming approaches for resource allocation, and accounting tools for other physical constraints. Comparison studies on the use of energy prices alone versus a combination of energy prices and new technology show that new technology permits higher gross national product growth rate, more jobs, lower delivered energy prices, and improved energy-economic efficiency.

INTRODUCTION

During its two-and-one-half years of operation, the U.S. Energy Research and Development Administration (ERDA) made significant improvements in planning processes for new technology development. An important contributor to the planning procedures was the application of a group of economic and energy models that enhanced ERDA's capability toward understanding the complex interactions of the nation's future energy systems. This paper describes the planning, modeling, and forecasting efforts used by the Office of the Assistant Administrator for Planning and Analysis.

The role of the modeling and forecasting program can best be demonstrated by briefly describing the ERDA planning system. The planning system was derived from the ERDA mission to create energy options for the future. The analytical work of the agency examined those energy options through a 25-yr period to provide a reasonably comprehensive picture of the most promising alternatives. The results from the modeling work fed directly into the other aspects of the planning process.

ERDA PLANNING SYSTEM

The legislation that established ERDA gave broad responsibilities for the development and demonstration of new energy technologies. To carry out the legislative mandate and to achieve the goals of national energy policy, ERDA had to be very diligent and careful in the planning of its activities. ERDA's planning responsibilities extended beyond those needed to formulate its own programs. The legislation required that ERDA annually prepare a comprehensive energy research, development, and demonstration (RD&D) plan. This requirement was fulfilled by the publication of three reports[1-3] entitled "A National Plan for Energy Research, Development, and Demonstration." The first report (ERDA 48) was published on June 30, 1975; the second (ERDA 76-1) was published on April 15, 1976; the third (ERDA 77-1) was published on April 21, 1977.

To carry out these responsibilities, ERDA developed an integrated planning system. The objectives of this system were to provide five items:

1. a disciplined method to analyze U.S. energy needs

2. a formulation of the federal government role in addressing those needs

3. the design of programs to fulfill the government role

4. the allocation of resources consistent with the program design

5. an effective program management.

The planning system addressed such major issues as the energy technologies to be pursued by the nation; the role of the private sector; the federal government role in research and development (R&D) as well as regulatory, fiscal, and institutional matters; the specific program goals; the cost-effective management of program plans; and budget decisions. The system comprised analytical, planning, resource allocation, program implementation, and program evaluation activities (Fig. 1).

The analytical activities provided support to the planning activities, which in turn guided the resources allocation and program implementation activities. Program evaluation served to check actual progress against planned progress and provided a basis for updating and changing planning goals. It should be noted from the outset that environmental planning was a key part of the ERDA planning system. Environmental issues (including occupational and human health, safety, and ecology) were thoroughly considered and weighed throughout the analysis and decision-making process. Environmental planning was embodied in the planning structure to ensure that environmental R&D

priorities were maintained and that ERDA resources were allocated to produce environmentally acceptable energy technology.

The first element and step in the planning system was to determine what ought to be done. The identified actions were based on a number of analytic inputs and policy assumptions. These analyses involved the development of alternative future scenarios and the use of models that replicate the dynamic behavior of the energy system. The series of cases spanned the range of likely future conditions by making assumptions about various factors such as resource availability, technological developments, absolute and relative costs of various fuels and technologies, environmental standards, status of control technologies, population distribution and makeup, gross national product (GNP) and its components, capital availability, labor productivity, and lifestyles.

Examination and comparison of the cases provided insights into policies, technologies, or other factors that are important regardless of the nation's future direction. The analysis also identified problems common to potential futures, defined common needs, and indicated the probable market size and likely timing range for new technologies. The reasonableness of these cases could be tested and the impact compared for any inhibiting constraints (e.g., resources, manpower, financial requirements, regulatory processes, national interests and security, legal restrictions, institutional barriers, and prevailing sociopolitical moods).
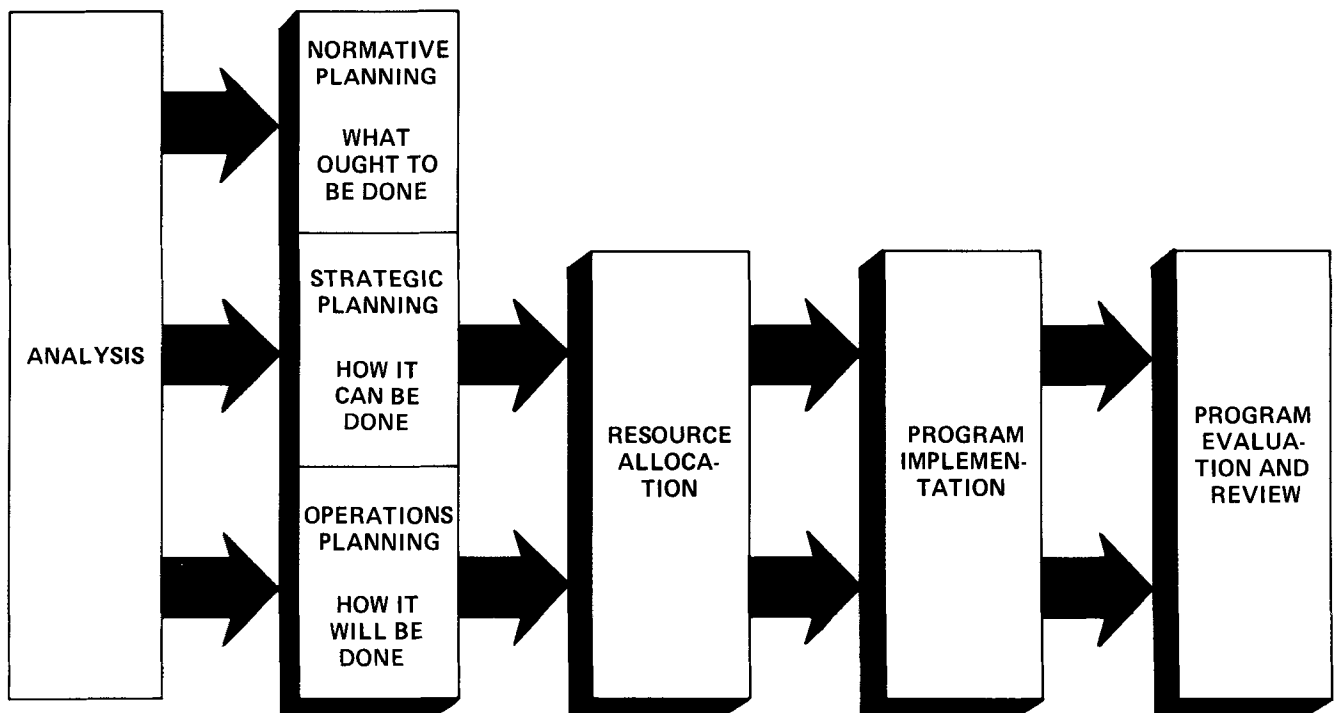

Fig. 1. ERDA's approach to planning, budgeting, and review.

Once consequences of alternative cases had been assessed, choices could be made and action directed toward the ends that such choices dictated. Thus, this element of the planning system was not directed toward prediction, but rather toward goal setting. It was this activity that provided the basis for the annual National Energy RD&D Plan.

The next element of the planning system dealt with how the established goals could be achieved most effectively. An important part of this activity was to determine the roles of the private sector and the government sector in achieving the goals. This activity was directed at individual programs to develop specific energy systems. A strategy was developed to describe and justify the federal role in the energy RD&D of any given technology. This strategy contained the rationale for pursuing a technology nationally, identified the private sector role, and described federal RD&D program goals and managers (Fig. 2).

The development of this strategy required analysis of the energy system options and the constraints to market penetration. The keystone of this analysis was the replication of the private sector decision-making process to determine appropriate private and public sector roles. To the maximum extent possible, the analysis was based on a quantitative assessment of benefits, costs, and risks. Furthermore, the analysis employed decision criteria and rules appropriate for the market sector in which the energy system option would be introduced.

Government RD&D involvement will be restricted to those energy technologies for which (a) private returns are too low or market barriers too high to induce private sector activity, and (b) public returns are sufficiently high to justify government role. If the private rate-of-return and other figures-of-merit for an energy system option do not meet requirements, the venture will not be considered for private funding. If the venture does not meet the requirements and it seems likely that the private sector will fund the venture, then the government will perform only its legislated regulatory functions.

If factors that preclude sponsorship of the venture in the private sector are identified (e.g., high risk, high exposure, and market fragmentation), it was necessary to determine if the public rate-of-return was sufficiently high to justify government involvement. If the public rate-of-return is judged to be high, it must then be determined what type of government involvement is appropriate. The federal government could use various incentives (e.g., guaranteed loans, capital grants, price supports, R&D funding) to induce the private sector to innovate or accelerate the rate of introduction of new products in the marketplace. The most effective incentive(s) could be determined by repeating the private sector decision analysis and determining which incentives result in
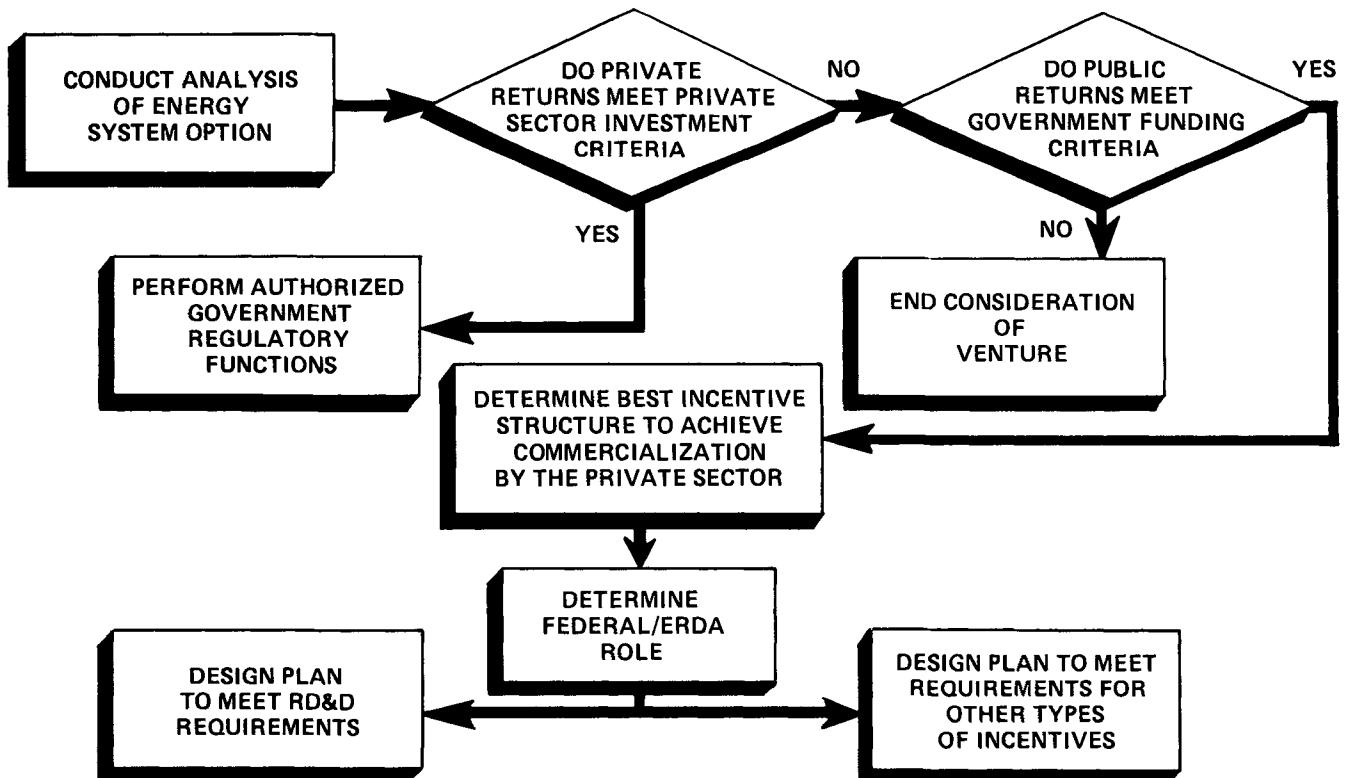

Fig. 2. Strategic planning logic.

the venture meeting the private sector's investment criteria. Those incentives most likely to induce private sector participation at the least cost to the government could then serve to define the primary government role.

Program plans were developed to identify the requirements for executing the federal role justified in the strategy. The program plan set forth objectives, key decision points, and milestones. It includes schedules and resource requirements. These program plans were supported by trade-off analyses based on the cost/effectiveness of alternative program designs.

Resource allocation is the decision-making process by which the ERDA budget was developed. Resource allocation activities were based on

1. federal role and objectives

2. relative program priorities and long-term resource requirements based on plans and an estimate of future budget constraints

3. status of the current program (e.g., study phase, pilot operations, demonstration plant), including the work to be done, as described through program planning and the degree of private sector cost-sharing being achieved

4. size and relative priorities of the federal budget, as determined by the President and Congress based on total budget constraint and competing demands for federal funds.

On the basis of this information, trade-offs aimed at allocating ERDA resources to the most important activities were defined.

Program implementation activities focused on the development of an operating plan that delineated the specific activities to be accomplished within approved budgets. Through program implementation, ERDA management

1. approved program execution, including annual operation plans for specific programs

2. established the controls that govern implementation by the operating elements

3. established the milestones or other means for management review considered essential to control the program

4. prescribed the framework for timely reporting against these milestones.

ECONOMIC AND ENERGY MODELS

Having set forth the basic elements of ERDA's planning system and the relative place for analytical tasks within that system, we proceed to identify the five models used by ERDA. These economic and energy models have been individually developed by

different energy modeling groups and were combined into an integrated model set under ERDA's direction.

The Data Resources Incorporated Macroeconomic Growth Model[4] was used to specify the annual values for the GNP and its component parts as well as relative prices and shares for capital and labor. The growth model was used to estimate the nominal and real values of consumption, investment, government spending, and net exports over time through the year 2000, given exogenously specified population and productivity estimates, and aggregate production and utility functions.

This model has the important feature of combining both the aggregate supply and the aggregate demand aspects of growth within a single framework. The supply side of economic growth depends on three general forces: productivity improvement and gains in input efficiencies, increases in the quantity and quality of labor input, and increases in the quantity and quality of capital input. Each of these forces is explicitly treated in the growth model. Together these components permit the derivation of production or output capacity of the economy.

The next step was to forecast the level and pattern of demand. This involved the endogenous estimation of the demand for consumption expenditures and the demand for investment goods, and the exogenous specification of government demand and export demand. Together these components gave the total demand for the production of the economy.

If the total productive capacity and total planned demand were initially not in equilibrium, a series of demand-supply imbalances that lead to adjustment in prices occurred. For the long-run growth model, the assumption was made that markets have time to reach a position of consistency between demand and supply. The overall result was that the macroeconomic forecasts reflected both supply and demand aspects of economic activity that were brought into equilibrium at all points in time by market adjustments in prices and quantities.

The second model was the Hudson-Jorgenson Long-Term Interindustry Transactions nine-sector econometric model.[4,5] This model is based on a system of accounts for nine private domestic sectors of the U.S. economy, including final demand, primary input, and interindustry transactions in current and constant prices. The U.S. economy is divided into nine industry groups, including five groups within the energy sector—coal mining, crude petroleum and natural gas, petroleum refining, electric utilities, and gas utilities. The model also includes three categories of primary inputs—capital services, labor services, and imports—and four categories of final demand—consumption, investment, government purchases, and exports.

Through this accounting system, the process of production for energy and nonenergy products can be

traced from the purchase of primary inputs through all stages of intermediate processing to deliveries to final demand. Conversely, any final demand purchase could be traced through the production structure to find its requirements in terms of intermediate use of each type of product and, in turn, the primary input requirements for all these intermediate inputs.

The econometric model of interindustry transactions includes models of producer behavior for each industrial group included in the model and a model of consumer behavior that allocates personal consumption expenditures among the commodity groups included in final demand. An important feature of the production models is the characterization of producer behavior through technical coefficients that are functions of prices of output and of primary and intermediate input. The technical coefficients change through time in response to price changes giving a flexibility that permits the substitution of inputs by producers such as shifts in demand for energy inputs.

The two economic models were linked to provide a detailed analysis of the pattern of economic activity at each point in time. For a specific energy policy analysis, the interindustry model may provide results that were not consistent with the macroeconomic projections. Therefore, the values of the interindustry model were fed back to the macroeconomic model in an iterative mode until a completely consistent set of values for all parameters was determined.

The third model used in this process was the Brookhaven-University of Illinois Input-Output Model,[6] which was used to estimate functional end-use energy requirements such as space heat, air conditioning, motive power, and petrochemical feedstocks. This model consists of a 110 X 110 matrix of input-output coefficients and a 110-order vector of final demands. A significant feature is that the output of the energy sectors is not measured in dollars but in energy units. The output of these sectors, termed energy supply-conversion sectors, is not distributed directly to other sectors of the economy. Instead, their output is distributed to the functional end use, or energy product, sectors.

Energy input to nonenergy sectors is respecified in terms of these functional energy product categories rather than in the usual manner of generated electricity and specific fuels. By specifying input requirements in terms of such energy products as space heat, substitution among fuel supplies is permitted. Technological change associated with fuel substitution can be incorporated in the production functions of the energy supply-conversion sectors.

The results from the Hudson-Jorgenson model and the macroeconomic growth model were fed to the Brookhaven-Illinois model. An allocation algorithm disaggregated the 9 sectors to the 110 sectors, so that a more detailed representation of energy activities was developed. This process was an inter-

mediation step required to provide the estimates of end-use energy demands to be used as constraints in the linear programming model.

The fourth model was the Brookhaven Energy System Optimization Model[7,8] (BESOM), a linear programming (LP) energy allocation model. The model is based on the Reference Energy System, a network representation of energy flows from alternative resources through various energy conversion and delivery activities to specific end uses. Each link in the network represents a process or mix of processes used for a given activity. Cost, efficiency, and emission coefficients may be associated with each link. An Energy Model Data Base that includes these values for 400 supply processes and 200 end-use processes supports the modeling work.

Thus, the optimization model includes provision for the full range of interfuel substitution, including substitution between electric and nonelectric energy forms. It has provision for 27 types of energy supply forms and 22 types of energy demand categories. Both existing and new technologies can be represented in the model, permitting an evaluation of the potential introduction and application of new energy forms.

The optimization of the energy system is usually performed with respect to cost, and the objective is to minimize the annual cost of energy service, subject to policy, economic, environmental, or other constraints that may be represented in the objective functions and constraint equations. However, the model can also be operated to minimize other factors such as resource use or an environmental index. Multi-objective applications have been investigated. New features recently added to the model include the description of costs of end-use devices such as heat pumps or electric autos, which can be factored into the cost objective function, and an ability to adjust energy supply and demand constraints based on pre-specified price elasticities.

The energy end-use demands for the BESOM model were provided by the Input-Output Model. The constraints on energy supplies were exogenously specified, being derived from estimates of energy supply curves modeled by other researchers. After solution of the linear programming model, a check was made to determine if the energy values were consistent with the energy coefficient values used initially in the Input-Output Model. If not, the new LP values were inserted into the Input-Output Model and the procedure continued until a convergent solution was obtained. The integration process for the models is shown in Fig. 3.

The final model used was the Bechtel Energy Supply Planning Model.[9] The model translates the output of the energy flows established by the Brookhaven Models into a listing of energy and transportation facilities required to satisfy the specified energy
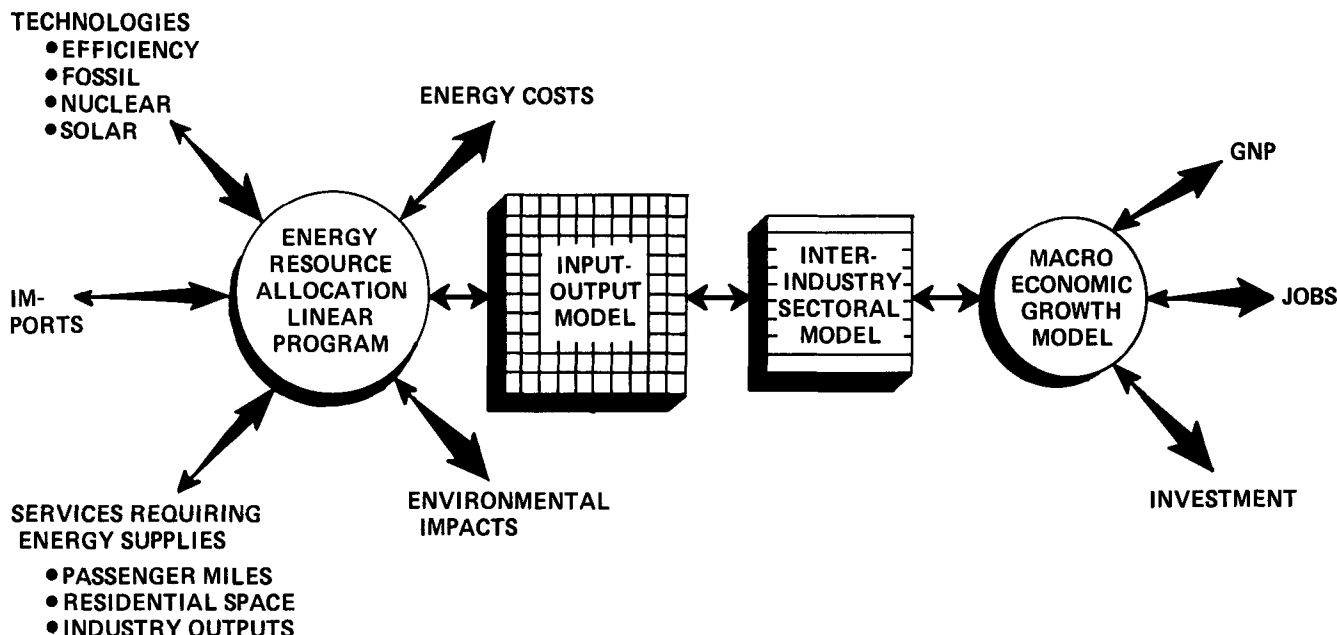
Fig. 3. Energy-economic model integration.

inputs. For each of 66 energy facilities and 25 transportation modes, a data set describes the quantities of capital and operating costs, selected materials and equipment, and various kinds of manpower necessary to provide these activities. For an aggregate energy scenario, the model provides an annual time-phased quantification of total requirements for each category of physical resources, accounting for lead times in construction and delivery of supplies.

The model is useful for identifying potential constraint areas in implementing an energy future, such as potential shortages in critical manpower or equipment, and quantifying the total capital costs associated with a given energy future.

APPLICATION OF THE MODELING TOOLS

These models in an integrated form were applied to examine alternative supply and demand policies in preparation of the National Energy RD&D Plan.[2,3] The integration of these tools marked the first time that a macroeconomic model, two interindustry models, an energy technology resource allocation model, and a requirements model for resources other than energy had been linked together to examine the energy system. These analytic tools also marked the first time that changes in future economic activity have been analyzed based on the probable introduction rates of new technology.

It was possible to operate the models in the conventional manner of determining macroeconomic values to provide inputs to the interindustry models that provided inputs into the energy allocation model. These steps included provisions for feedback of

values at various steps of the process to obtain consistent values by iterative solution techniques. More importantly, it was also possible to apply the models in a reverse mode. By inserting new technologies or deriving different energy mixes in the resource allocation model, the new values were fed forward to the interindustry models and to the macroeconomic model to evaluate changes in the entire set of economic parameters.

Although there still remain some definitional and procedural difficulties in the linking of the models, the procedure was sufficiently developed to permit ERDA to examine alternative policies and technologies for their effects on economic growth and on reducing dependence on foreign energy supplies. The time period examined in these studies was 1985 to 2000, using the Federal Energy Administration's projections through 1985 as a starting point. This period is the time that many of our RD&D projects will begin having a major impact on the country.

The initial policy cases examined were:

1. A supply policy was based on the introduction of new technologies including oil shale, coal liquefaction and gasification, geothermal energy, and solar electric and direct solar applications. The estimates of the maximum energy flows that could be expected from the new technologies were based on the technical calculations provided by ERDA program divisions. Import target levels were set as a declining percentage of total domestic energy use.

2. A demand policy was based on rising energy prices (via taxes and tariffs only). Demand measures (rising energy prices) were used to eliminate any

supply-demand gap still remaining after the introduction of new technologies. The procedure used was to increase the prices of energy supplies gradually (which resulted in lower demands) until the specified import target levels were reached. The 1985 import target level was 10% of total energy consumption, and the 2000 target level was 5%.

The effects of these policies on energy supply and demand to achieve the specified targets for oil imports are shown in Fig. 4. The results obtained for these policies relative to the base case have some important implications for R&D activities and for the implementation of new technology in the marketplace (Fig. 5):

1. The introduction of new energy-producing technology has a significant positive effect on the level of GNP and on the economic well-being of the country. The discounted value of future GNP restored by adding to supplies (through technology introduction), instead of increasing prices to reduce demand, is several-fold larger than the discounted value of the accumulated expenditures on RD&D.

2. Higher prices (30% above those otherwise expected in 2000) could be required to achieve the specified energy demand reductions, and this appears to be an undesirable cost to the nation. Implementation of more efficient energy using and producing devices would be the preferable way to achieve the import reduction. The price increases needed to achieve a sufficient demand reduction are half as large when new supply technology is available as when it is

not available. Energy demands are rather inelastic, with a 10% increase in price required to produce a 2.5% demand reduction in 1985 and a 4.5% demand reduction in 2000.

3. Increases in the inflation rate occur as a result of energy price changes. In addition to the introduction of new technology, high taxes and tariffs (over 150% on oil and 20% on gas) are required to achieve the specified lower demands. This situation leads to a long-term increase in the general inflation rate of ~0.3 percentage points.

4. The effects of higher prices and new technology result in a slowing of the rate of increase in the output of the domestic economy. The rate of increase in real GNP declines, resulting in a small drop in the level of real GNP (~2% lower in 1990 and 3% lower in 2000).

5. Changes in labor requirements result in an increase in unemployment. A lower real GNP produces a lower demand for labor inputs to the economy. The restructuring of the economy to reduce energy use offsets this somewhat through increased demands for labor as a substitute for energy inputs. The overall result is a long-term increase in the unemployment rate (for both policy alternatives) of from 0.5 to 1 percentage point higher than for the base case.

6. New technologies are only marginally competitive with existing technology in the short run, but compete successfully by the end of the century. New
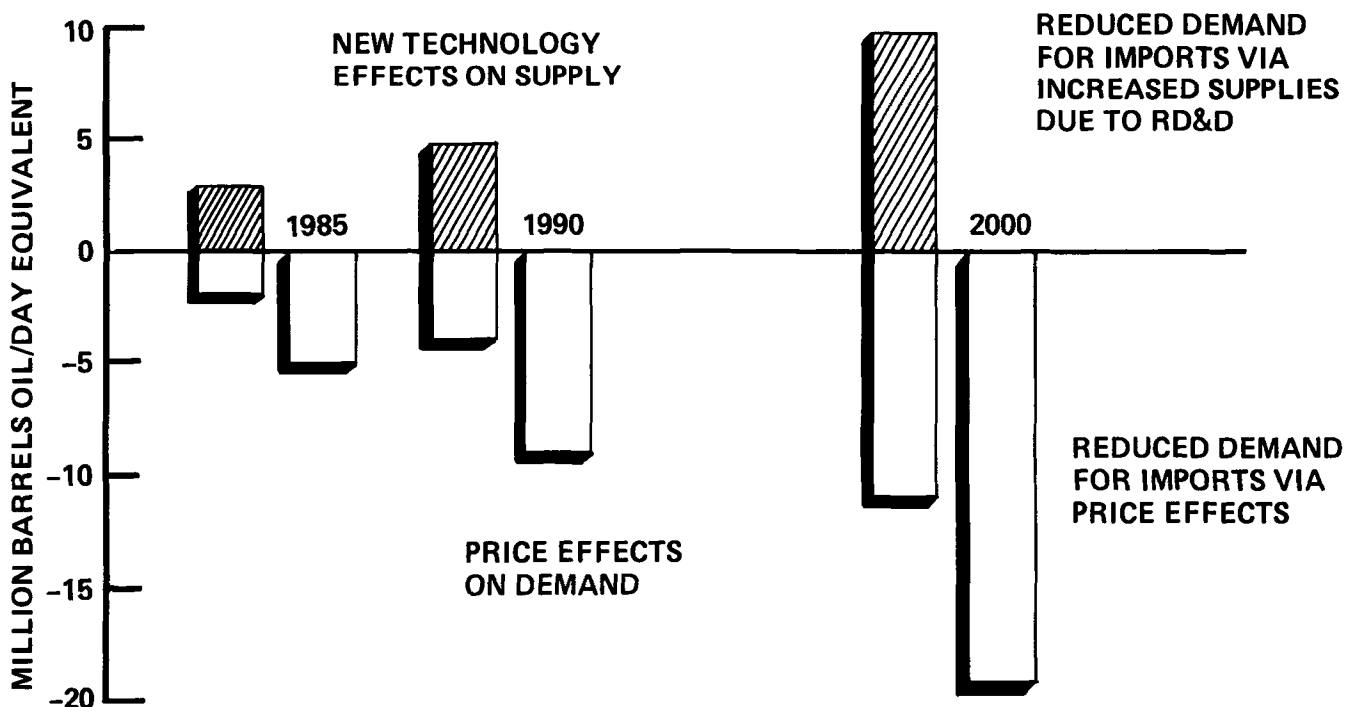

Fig. 4. Effect of policies on energy supply and demand to achieve fixed-level imports.

THIS STUDY COMPARES USE OF PRICING
POLICIES ALONE TO PRICING POLICIES
COMBINED WITH ENERGY RD&D

NEW TECHNOLOGY AVAILABILITY PERMITS:
- **INCREASED GROWTH RATE IN GNP**
- **MORE JOBS**
- **LOWER ENERGY PRICES**
- **REDUCTION IN INFLATIONARY PRESSURE**
- **CONSEQUENT IMPROVED ECONOMIC
  WELL-BEING**
- **IMPROVEMENT IN ENERGY-ECONOMIC
  EFFICIENCY AS MEASURED BY THE
  ENERGY/GNP RATIO**

Fig. 5. Effect of policies on energy supply and demand to achieve a fixed import level.

technologies (primarily oil shale, geothermal, and direct solar) may account for 16% of total energy in 2000 as compared to only 4% in 1985.

7. There is an improvement in energy-economic efficiency (as measured by the energy/GNP ratio). The model results indicate a 2 to 3 percentage point improvement for each 10% change in energy prices.

These efforts were an integral part of the planning, program, and budget review process within ERDA. These results provided guidance for the strategic and operational planning in preparation for each year's National Plan on RD&D.

REFERENCES

1. "A National Plan for Energy Research, Development, and Demonstration: Creating Energy Choices for the Future," ERDA 48, U.S. Energy Research and Development Administration (1975).

2. "A National Plan for Energy Research, Development, and Demonstration: Creating Energy Choices for the Future," ERDA 76-1, U.S. Energy Research and Development Administration (1976).

3. "A National Plan for Energy Research, Development, and Demonstration," ERDA 77-1, U.S. Energy Research and Development Administration (1977).

4. E. A. HUDSON and D. W. JORGENSON (1974a), "U.S. Energy Policy and Economic Growth, 1975-2000," Report to the Office of Energy and Natural Resources, U.S. Department of the Treasury; published in *Bell J. Econ. Manage. Sci.*, 5, 2, 461 (1974); see also, *Proc. IIASA Working Seminar on Energy Modeling*, Laxensburg, Austria, pp. 174-278, International Institute for Applied Systems Analysis.

5. R. DULLIEN, "User's Guide to the DRI Long-Term Inter-industry Transactions Model," Interim Report to the U.S. Department of the Interior, Washington, D.C. (1976).

6. D. J. BEHLING, W. MARCUSE, M. SWIFT, and R. G. TESSMER, "A Two-Level Iterative Model for Estimating Inter-Fuel Substitution Effects," BNL 19863, Brookhaven National Laboratory (1975).

7. K. C. HOFFMAN, "Unified Framework for Energy System Planning," in *Energy Modeling*, M. F. SEARL, Ed., Resources for the Future, Washington, D.C. (1973).

8. E. A. CHERNIAVSKY, "Brookhaven Energy System Optimization Model," BNL 19569, Brookhaven National Laboratory (1974).

9. M. CARASSO, J. M. GALLAGHER, K. J. SHARMA, J. R. GAYLE, and R. BARANY, *The Energy Supply Planning Model*, Vols. I and II, Bechtel Corporation (1975).

RISK ANALYSIS OF RADIOACTIVE WASTE MANAGEMENT SYSTEMS IN GERMANY

HANS J. WINGENDER *NUKEM GmbH, P.O. Box 11 00 80 D-6450 Hanau 11, Federal Republic of Germany*

Within the scope of a system study, "Radioactive Wastes in the Federal Republic of Germany," performed from 1974 through 1976, the questions of risk assessment were investigated. A risk analysis of a high-level waste (HLW) management system was performed. The results of the HLW tank storage are that the risk expectation value is 700 nJ/kg × RBE (7 × 10⁻⁵ rem) per year for atmospheric release. The discussion of the main contributing accidents shows the possibility of reducing the risk by technical means. A qualitative comparison on a release basis with the results of the WASH-1400 report shows significant differences that can be explained by the different methodologies applied.

The risk analysis activities have led to a comprehensive risk assessment project, which was recently started. The project includes research and development tasks concerning nuclide migration and transport to the ecosphere, nuclide mobilization by various mechanisms, methodology problems, data collection, computer code development, as well as risk analyses of waste management facilities. It is intended to round off the project with risk analyses of spent fuel element transport, storage, and reprocessing.

HISTORY

In the period from 1974 through 1976, a study of the overall situation and the further development in the field of radioactive waste in the Federal Republic of Germany (FRG) was performed.[1] The study was directed by the NUKEM Company under a contract with the Federal Ministry for Research and Technology. (See Appendix A.) It was performed in cooperation with seven other institutions engaged in nuclear technology.

Within the study, a risk analysis group consisting of members of the participating institutions reviewed the applicability of risk assessment methodologies, for at the very outset of the study the question of risk assessment arose and became a serious problem. Risk analysis experts familiar with waste management were not available. Moreover, risk analysis of power plants is rather different from risk analysis of waste management systems. The differences refer to the fact that far more nuclear power plants than waste management plants have been built and operated. There is more experience with the design and the operation of reactors. It also refers to the different inventories of radioactive materials, pressures, temperatures, and—very important—different time scales.

On the basis of the approaches and results made and obtained by Lambert,[2] Rasmussen,[3] and Smith et al.,[4] and supported by the gratefully accepted help of the Battelle Pacific Northwest Laboratories, a uniform concept of risk assessment was obtained.[5] It was applied to a high-level radioactive waste (HLW) management system (Fig. 1).

It should be emphasized that the task of the risk assessment group was to demonstrate either the applicability or the inapplicability of the probabilistic risk assessment concept on waste management systems. Because of the lack of actually built and fully designed plants, the system analyzed by the group was of necessity in many respects a rather hypothetical one, although it was intended to approach reality as closely as the shortness of time allowed.

HLW TANK STORAGE RISK ANALYSIS

Since the risk analysis of HLW tank storage has already been published,[5] only a summary is given here. The course of the analysis consists of five steps:

```
┌─────────────────────────────────────┐
│                                     │
│   LIQUID TANK STORAGE               │
│                                     │
│   VITRIFICATION PLANT               │
│                                     │
│   INTERIM SURFACE STORAGE           │
│     FOR VITRIFIED WASTE             │
│                                     │
│   TRANSPORT TO ULTIMATE STORAGE     │
│                                     │
│   ULTIMATE STORAGE IN SALT          │
│                                     │
└─────────────────────────────────────┘
```

Fig. 1.   HLW management system.

1. preliminary analysis

2. identification of the system failures

3. fault-tree evaluation

4. risk assessment

5. risk reduction.

In the preliminary analysis phase, the system, the sources of radioactive material, the barriers preventing release, and the undesired event were defined in detail. The accidental release of radioactive material from the storage confinement was chosen as the undesired event.

The hypothetical, i.e., not intended to be built as described here, tank storage facility is designed for a capacity of 5000 m^3 of HLW arising from light water reactor (LWR) fuel reprocessing. The capacity corresponds to 7500 Mg of reprocessed uranium or the 5-yr throughput of a 1500 Mg/yr reprocessing plant. The following assumptions were made with regard to the fuel:

1. pressurized water reactor (PWR) fuel (3% enriched)

2. burnup: 2.59 PWs/Mg of uranium (30 GWd/t)

3. precooling time: 1.30×10^7 s (150 days).

The waste is stored in ten tanks (plus one standby tank). The specific activity of the material in a tank depends on the age of the waste and varies from 1.3×10^{17}/s·m^3 (3.5×10^6 Ci/m^3) to 2.1×10^{16}/s·m^3 (5.8×10^5 Ci/m^3). The maximum value of thermal power per tank due to the decay heat is ~8 MW.

The component materials to the risk analysis are the cooling system, the ventilation system, the off-gas system, and the system of barriers preventing release. They are briefly described below.

Cooling System

The heat is removed by eight cooling loops (W 20/1 to W 20/8) per tank (three of them standby tanks), each with a capacity corresponding to 20% of the maximum heat generation per tank. The loops can be independently valved off. They are part of the two primary cooling circuits (one circuit standby). The primary circuits are independently operated by one pump each (one standby per circuit), providing a slight overpressure against the liquid waste.

Each primary circuit is connected to both secondary circuits (one of them standby) via three heat exchangers W 1, W 2, W 3 (two of them standby), or via W 4 (one for each tank). The secondary circuits are operated by one pump each (one standby per circuit), providing a slight overpressure against the primary coolant and pumping the secondary water through a single wet cooling tower. Makeup water is taken from a river. If river water is not available, the makeup water is taken from a water reservoir (lake). If neither of the secondary cycles is available, it is possible to use purified lake water directly for the primary circuits. If both primary circuits are out of order, the tank off-gas can be condensed in W 4 using water from the reservoir. If no cooling is available, it lasts at least 4 h until the waste starts to boil.

The instrumentation shown in Fig. 2 is not described here.

Ventilation System

The ventilation system maintains a slight underpressure against the atmosphere. The air for the hot cells is taken from the operational zone of the facility via a filter. The air inlet and outlet of each cell can be shut. Having passed through the cell, the air is led through two filters in line, each of them with an interchangeable standby. Pressure differences are measured at the filters and between intake and outlet points. Three fans (two of them standby) maintain the pressure differences and force the air to the stack. The air is monitored for radioactivity at several points of the system.

Off-Gas System

The off-gas from the tanks is cleaned in a line consisting of a condenser, three scrubbers, and a heater. Downstream of the heater there are a filter, a fan, and another filter, each of them having a standby parallel to and interchangeable with it. After the last filter, the off-gas is mixed with the air and released to the stack. The off-gas is efficiently monitored for pressure, temperature, and radioactivity.

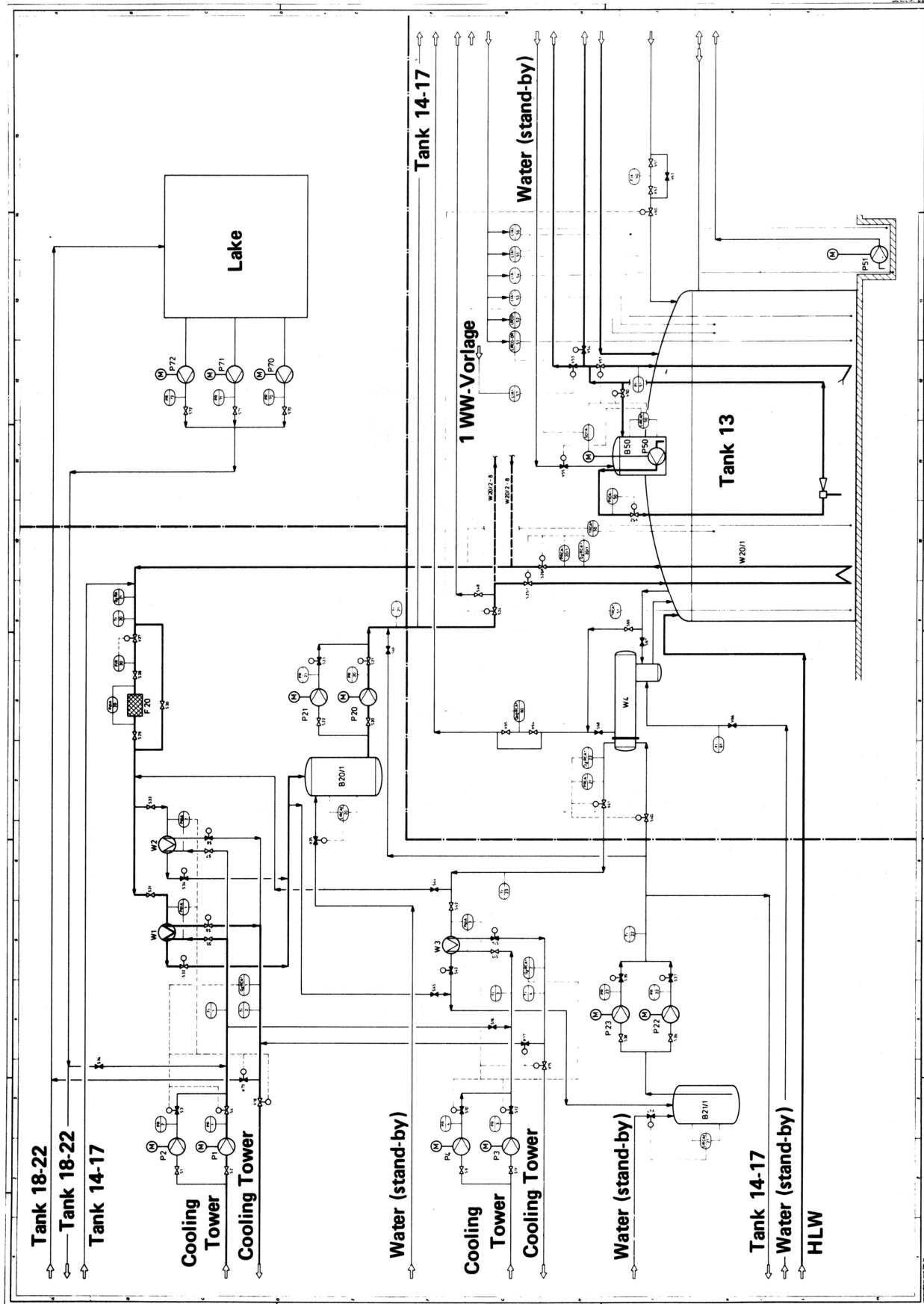It is possible to bypass the cleaning line, to reclean the off-gas, and to shut the outlet.

Fig. 2.   Instrumentation of the cooling system.

System of Barriers

There are several barriers to prevent release of HLW to the environment:

1. stainless-steel walls of tanks and pipes

2. stainless-steel drip trays beneath tanks and pipes

3. leakage sumps

4. pumps pumping leakage to the reserve tank

5. leakage alarm system

6. concrete walls of the cells.

The barriers are penetrated by coolant pipes, the ventilation system, the off-gas system, and electrical cables. The construction of such passages prevents radioactive material from escaping except in form of aerosol and gas. Therefore, the systems described above are equipped with retaining devices like filters and valves, and with additional barriers such as pressure steps and coolant separation by heat exchangers.

The identification of the system failures comprised the development of the fault trees, the determination of the component data, and of the release fractions for a sequence of barrier failures. The fault-tree method has been chosen because of the more systematic and more inquisitive way of analysis compared with the event-tree method.

Since the fault trees comprise ~20 000 possible system failures, they cannot be shown here. A zero approximation review of these accidents with respect to frequencies and consequences revealed ~100 events deserving to be subjected to further examination. A detailed study of the triggering events, the transport mechanisms of radioactive materials to the environment, and an investigation of the probabilities of the basic events involved were performed for the 100 accidents. Release values >3.7 X 10^{16}/s (10^6 Ci) appeared only with frequencies lower than 10^{-12}/yr. This figure is meaningless, because major impacts on the plant caused by natural phenomena such as earthquakes were not taken into consideration. However, 3.7 X 10^{16}/s (10^6 Ci) releases caused by technical failures attain frequencies of ~10^{-7}/yr. The release to the atmosphere does not exceed 3.7 X 10^{14}/s (10^4 Ci). Finally, the average expectation value of failure induced "release rates" is ~1.9 X 10^{11}/s (5 Ci) per year.

To assess the risk of the system, the dose to humans has to be determined. At this point a rather rough approximation has to be superimposed on the sophisticated fault-tree method. This especially concerns the migration and the transport through deep layers and surface soils. Therefore, only the dose caused by accidental release to the atmosphere is shown here (Fig. 3).
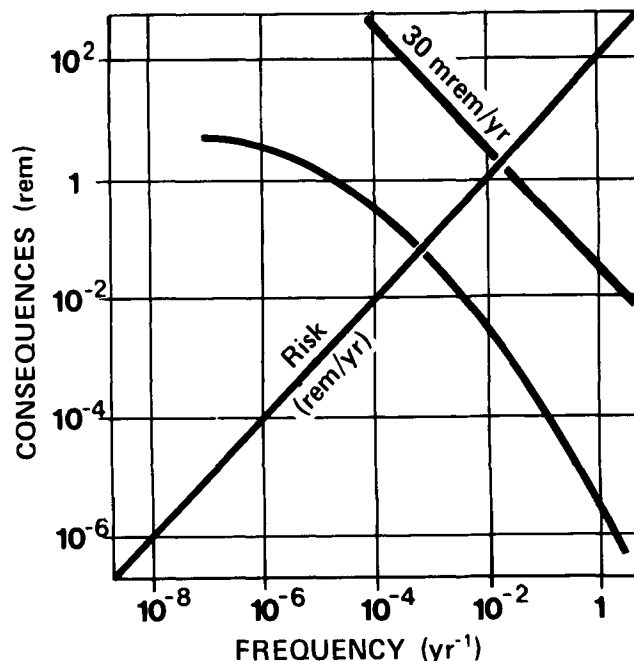
Fig. 3.   Risk of HLW liquid tank storage (atmospheric release.

The expectation value of the risk amounts to ~700 nJ/kg X RBE (7 X 10^{-5} rem) per year. This figure is far below the operation limit of 300 μJ/kg X RBE (3 X 10^{-2} rem) per year as defined by law in the FRG, and also significantly below the 10 μJ/kg X RBE (10^{-3} rem) per year, applied as working limit for nuclear facilities during normal operation. (The comparability of risk expectation values and normal operation dose rate is not discussed here.)

As mentioned above, radionuclides released into the ground beside or below the facility could not yet be traced with the accuracy desired for the confident assumption of dose values. But because of the very low frequencies of the more severe accidents with underground release, it is not expected that these contributions will significantly change the results.

To reduce the risk of the storage, the main contributing accidents had to be examined. Three of them are briefly discussed. Some data are listed in Table I.

Accident No. 1 is caused by simultaneous occurrence of the following events:

1. pipe rupture in a coolant loop and in a heat exchanger

2. coolant pressure being lower than the static pressure of the waste

3. pressure and radiation monitors of the cooling system fail.

In this case, HLW will be transported to the cooling tower.

TABLE I

Main Contributions to the Risk of the HLW Tank Storage

	Failure Number		
	1	2	3
F (yr^{-1})	2×10^{-5}	1×10^{-1}	1.4×10^{0}
C (mJ/kg $\times$ RBE)	6	0.006	3×10^{-5}
C (rem)	6×10^{-1}	6×10^{-4}	3×10^{-6}
Release to	Atmosphere	Atmosphere	Atmosphere
Release via	Cooling tower	Ventilation	Ventilation
Caused by	Pipe and alarm failures	Pipe break	Design failure

Accident No. 2 is caused by a rupture in the recirculating system on the top of the tank (Fig. 2). Because of the pressure in the recirculation system, the aerosol production at the fracture may be very considerable. The failure can be prevented by a design modification in favor of an air-jet pulsator system.

Accident No. 3 is caused by hydrogen concentration rising above 4 vol% in the air volume of a tank. The air flow removing the hydrogen generated by radiolysis is monitored for hydrogen amount and flow rate. The hydrogen monitor actuates the air valve in both senses and reduces the air flow in case of reduced hydrogen generation. This may result in a further decreasing hydrogen amount at the monitoring point and a feedback signal to decrease the air flow, etc. If the air flow alarm simultaneously fails, the hydrogen concentration may exceed the 4-vol% limit.

To prevent the accident, the monitoring system has to be changed. It has to monitor for hydrogen concentration instead of for amount, and an additional flow rate monitor has to be put into the line immediately after the hydrogen monitor.

Systematic investigations of the critical accidents in more detail than shown here reduced the risk figures by a factor of 10. It was encouraging to see how easily failures can be traced through the process flowsheets and how effectively they can be reduced or avoided by technical modifications or maintenance.

A preliminary and rather qualitative comparison with the results of the Rasmussen report was made. Figure 4 shows the comparison on a release basis: The maximum releases of both studies are equalized, and the frequency scale is original to both cases. This is possible because of the near-zero slope at low frequencies.
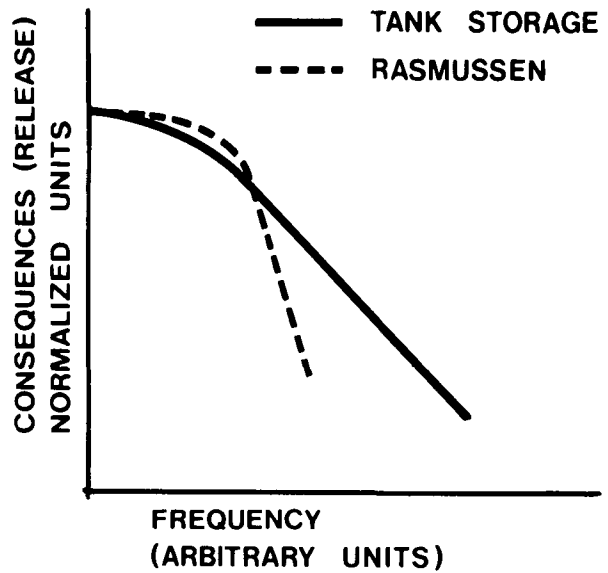
Fig. 4.   Qualitative comparison: tank storage, Rasmussen report.

The difference in the upper part of the graph is not significant. At higher frequencies, however, the Rasmussen results show a significantly steeper slope. The author supposes that this difference is caused by the difference in methodologies used and by the different objectives. The *Reactor Safety Study* is mainly concerned with well-known and well-operating plants and their possible severe accidents. These are defined by event trees and are specified by initiating events. Therefore, by an adequate method, the study has obtained a special class of accidents, which corresponds to the objectives. However, the tank storage analysis deals with a hypothetical plant. Here no experience exists. It cannot be said from

experience what the main sources of failures will be or how they will develop into accidents. Therefore, the objective was to identify all possible accidents as far as possible. The suitable tool for this task is the fault tree. In the end, the more frequent but less severe accidents are more realistically represented here.

CONCLUSIONS AND FURTHER ACTIVITIES

The results of the activities thus far described, which are of a fundamental rather than a quantitative nature, consist not only of the conclusions drawn but also of further activities in the field of risk assessment engendered by the insights gained. The conclusions include:

1. Risk analysis is a powerful tool to obtain a detailed knowledge about the possible failure behavior and, in consequence, a feedback to the further development of system design.

2. The efficacy of risk analyses is determined by the extent of the detailed knowledge of a system; therefore, the system to be analyzed should be in a stage of design, where basic engineering is about to be finished.

3. There are some problems connected with risk analysis that have to be solved:

a. methodology problems; for instance, common cause identification, impossible event identification, and computer code implementation

b. data problems; for instance, component failure data collection, component failure data critique, and release data determination

c. pathway problems; for instance, migration of nuclides in geologic strata, migration of nuclides in surface soils, transport of nuclides to the ecosphere, and development and mutual adaptation of models for these processes.

Therefore, it was proposed that the Federal Ministry for Research and Technology launch a comprehensive project including the solution, as far as possible, of the problems listed above and risk analyses of well-advanced systems in the waste management area.

An interaction scheme of the tasks within the project is shown in Fig. 5. The uppermost box represents a subproject including research and development (R&D) work in methodology, data collection, code development, and central compilation. The information needed will be transferred as indicated by the arrows. The arrow at the upper left means data transfer from outside the project. For
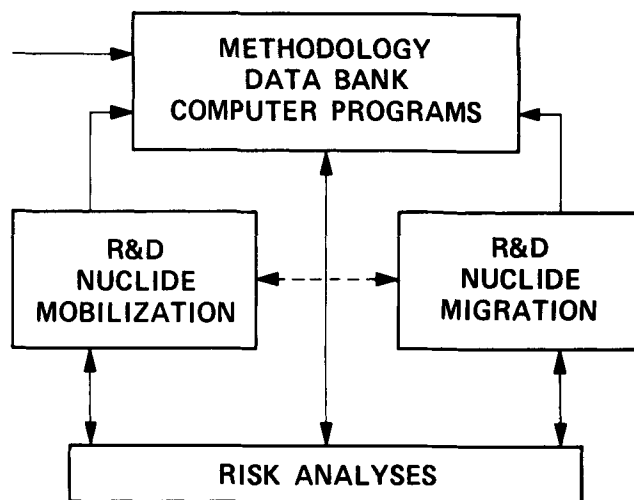
Fig. 5.   System of R&D concerned with risk analysis.

instance, there is a study for data collection and evaluation under way at the Karlsruhe reprocessing plant (scale: 35 Mg of uranium per year).

The two boxes in the center line of Fig. 5 represent a second subproject. It deals with mobilization, i.e., leaching and volatilization from fixation or solidification products and with the transport through media outside a facility to the ecosphere. The activities will be implemented by literature studies concerning the transport via food chains, etc. In this figure, this subproject is split in two boxes because the transport within plant limits has to be added. However, transport mechanisms within the system are specific for the system, and therefore they have to be evaluated within the risk analysis. The adaptation of all three processes will be performed in the first subproject. In the end, models of the transport supported by experimental data will be available.

A third subproject is represented by the lower box. At present it comprises risk analyses of about eight facilities from tank storages for liquid high- and intermediate-level wastes up to concepts for final disposal in geologic formations. It is intended to constitute a fourth subproject, which will be concerned with risk analyses of spent fuel element transport, storage, and reprocessing.

The whole project is named Project Risikoanalyse Entsorgung (PRE), where "Entsorgung" stands for the whole time from spent fuel element transport up to ultimate storage of wastes. There are at least three reasons for the close connection of R&D with risk analyses within one project:

1. Risk analyses are needed and can be performed for many facilities, because the basic engineering is under way or nearly finished in some cases.

Fig. 6.   Project structure of PRE.

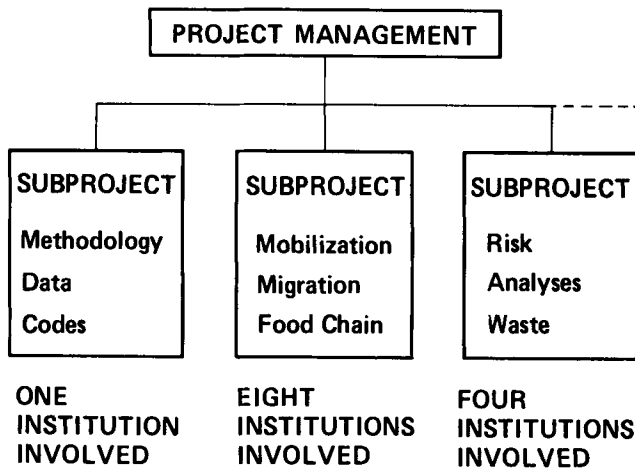2. Risk analyses have to be performed in a co-ordinated manner so as to obtain compatible results useful for detail engineering.

3. R&D tasks, data collection, etc., have to be performed with regard for the demands and the properties of risk analyses; therefore, the most effective way to do R&D is in close connection with risk analyses.

The organizational structure of the project (Fig. 6) is adapted to the tasks. At present, the project management consists of three persons, one for each subproject. The institutions participating in the project are represented in a project committee by one member each. (See Appendix B.) The time scale extends to the end of 1980. Within the two first subprojects, some activities were begun in 1976. The whole project starts at about this time.

APPENDIX A

INFORMATION ABOUT THE STUDY "RADIOACTIVE WASTES IN THE FEDERAL REPUBLIC OF GERMANY"

Sponsor: Bundesminister für Forschung und Technologie, Bonn

Participating Institutions:

Gesellschaft für Kernforschung, Karlsruhe
Gesellschaft für Strahlen- und Umweltforschung, Neuherberg
Gesellschaft zur Wiederaufarbeitung von Kernbrennstoffen, Leopoldshafen

Hahn-Meitner-Institut, Berlin
Kernbrennstoff-Wiederaufarbeitungsgesellschaft, Frankfurt
Kernforschungsanlage, Jülich
NUKEM (Project leader), Hanau
Vereinigung Deutscher Elektrizitätswerke, Frankfurt

APPENDIX B

INFORMATION ABOUT THE PROJECT RISK ANALYSIS "ENTSORGUNG" PRE

Sponsor: Bundesminister f. Forschung und Technologie, Bonn

Participating Institutions:

Bundesgesundheitsamt, Berlin
Gesellschaft für Kernforschung, Karlsruhe
Gesellschaft für Strahlen- und Umweltforschung, Neuherberg und Clausthal-Zellerfeld
Hahn-Meitner-Institut, Berlin
Institut für Kerntechnik, Technische Universität, Berlin
Institut für Hydrologie, Freie Universität, Berlin
Institut für Geologie, Universität, Clausthal
Institut für Geologie, Universität, Kiel
Kernforschungsanlage, Jülich
NUKEM, Hanau

REFERENCES

1. *Systemstudie Radioaktive Abfälle in der Bundesrepublik Deutschland*, Vol. 1-6, available from Bundesminister fuer Forschung und Technologie, Bonn, Germany (1977).

2. H. E. LAMBERT, "Systems Safety Analysis and Fault Tree Analysis," UCID-16238, University of California (1973).

3. N. RASMUSSEN, *Reactor Safety Study*, WASH-1400, U.S. Atomic Energy Commission (1974).

4. T. H. SMITH et al., "A Risk Based Fault Tree Analysis Method for Identification, Preliminary Evaluation, and Screening of Potential Accidental Release Sequences in Nuclear Fuel Cycle Operations," BNWL-1959, Battelle Pacific Northwest Laboratories (1976).

5. H. J. WINGENDER, "Systemstudie Radioaktive Abfälle in der Bundesrepublik Deutschland," Band 5, "Methodik und Anwendung der probabilistischen Risikoanalyse," SRA-5, available from Bundesminister für Forschung und Technologie, Bonn, Germany (1976).

CONTRIBUTIONS TO THE RISK EVALUATION OF A HIGH-LEVEL WASTE SOLIDIFICATION PLANT

H. BRÜCHER *Kernforschungsanlage Jülich GmbH*
Institute for Chemical Technology, D-5170 Jülich
Federal Republic of Germany

An analysis has been made dealing with the evaluation of risk of a high-level waste solidification plant. Fault-tree methodology was used to identify all possible accidents and to evaluate their probability of occurrence. The analysis shows that with regard to risk, the most important accidents occur during off-gas cleaning. Furthermore, the routine risk is of the same order of magnitude or greater than the most important accident risks.

INTRODUCTION

Since Rasmussen[1] published his *Reactor Safety Study*, the public interest in quantitative risk analysis has grown more and more. The analysis is expected to make a major contribution to the objectiveness of discussions on the safety of nuclear technology.

In the Federal Republic of Germany, corresponding efforts are being made, e.g., in connection with the system study, "Radioactive Waste in the Federal Republic of Germany." Details of this study are reported, for instance, by Wingender,[2] who presents a corresponding paper in this issue of *Nuclear Technology*. A contribution made to this study by Kernforschungsanlage Jülich, a government-sponsored establishment, involves the risk analysis of a model of a high-level liquid waste solidification plant.

SYSTEM DEFINITION

In this solidification plant, the high active waste from reprocessing light water reactor fuel is vitrified after a 5-yr interim liquid storage and is converted into a form suitable for final disposal. The solidification process consists of the following steps:

1. denitration with HCOOH (formic acid)

2. sampling and mixing with glass-forming additives

3. drying and calcining in a spray calciner

4. melting to borosilicate glass at temperatures of ~1375 K

5. filling into stainless-steel cylinders, cooling, and sealing.

Table I shows the assumed properties of the solidification plant. Some 1000 m³/yr of liquid waste are converted into 1500 glass blocks. The volume of each block is ~0.07 m³. The facility works with two lines of 50% capacity each.

Figure 1 shows schematically the containment/confinement system of the solidification plant. The waste is separated from the environment by several barriers that are independent of each other. The first barrier for both gaseous and liquid radionuclides consists of the process vessels, interconnecting piping, and off-gas treatment equipment. This equipment provides negative pressure versus hot-cell pressure and consists of a condenser, three washing columns, and two redundant stages of HEPA filters, installed in a series. The overall decontamination factor of the off-gas treatment system is assumed to be 10^5 for aerosols and 2×10^3 for ruthenium.

The second and third barriers for gaseous and particulate radionuclides are composed of the hot cell, the process building, and the ventilation confinement system. The ventilation system provides confinement by directing air and maintaining pressure differentials between zones. Ten air changes per hour is the assumed cell ventilation rate. The system consists of two redundant stages of HEPA filters for cell ventilation and one redundant stage for building ventilation. Treated process off-gas and cell ventilation air are released via a 100-m stack.

CONCEPT OF RISK

The purpose of the analysis was to evaluate the risk for the environment following the uncontrolled release of radioactivity. The analysis has been con-

TABLE I

Assumed Properties of the Waste Solidification Plant

Facility	
Capacity, heavy metal	1500 ton/yr
Cell size, vitrification	1800 m³
Cell size, denitration	730 m³
Cell ventilation rate, air changes	10/h
Off-gas treatment	
Total off-gas flow rate	1500 m³/h
Aerosol concentration	10 mg/m³
Ruthenium volatility	0.1%
High-level liquid waste concentrate (HAWC)	
Concentration per ton of heavy metal	0.65 m³ HAWC/ton
Total radioactivity	22 PBq/m³
Inhalation dose factor (aerosol)	2 nJ·m³/kg
Inhalation dose factor (ruthenium)	0.7 pJ·m³/kg
Dilution factor	2 μs/m³

fined to emissions into the atmosphere, because only for this release pathway are reliable dispersion models available; an extension is proposed.

The risk for the population in the vicinity of nuclear facilities can be represented as follows:

$$R = A \times B \times C \times D , \qquad (1)$$

where

R = risk, J/kg·yr

A = accident frequency, yr^{-1} (Both accident sequence and accident frequency were determined by fault-tree analysis.)

B = release, s^{-1} (For the dominant, that is, highest risk accidents, detailed release calculations were made with regard to the accident sequence.)

C = inhalation dose factor, J·m³/kg

D = dilution factor, s/m³.

The inhalation dose factor was calculated for aerosol release and for release of ruthenium. For this purpose, the radiation properties of the reference waste were computed using the ORIGEN code.[3] Based on 0.5% uranium and plutonium loss to the waste, a 150-day cooling period, and a liquid storage period of 5 yr, an overall radioactivity of ~2.2 × 10¹⁶ Bq/m³ liquid waste was calculated. From this value
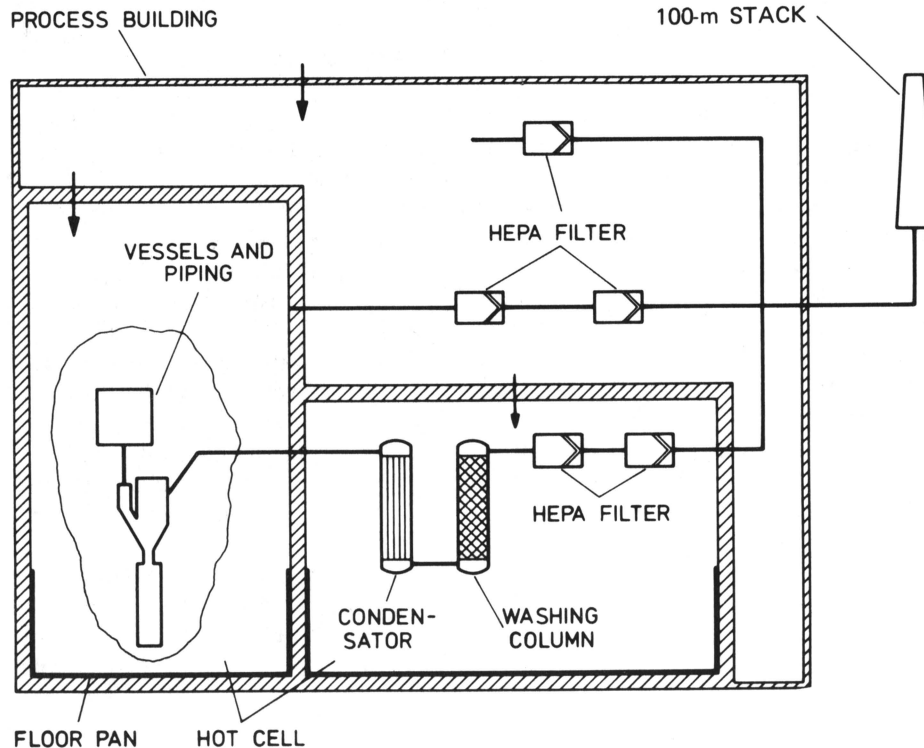

Fig. 1.   Solidification containment/confinement system.

and from the corresponding radiotoxicity, the inhalation dose factors of the mixed radionuclides were evaluated. The data are also given in Table I. Substantial contribution to the radiotoxicity is made by the bone-seeking actinides as well as ^{90}Sr (Ref. 4).

A sort of annual average dilution factor was chosen for the purpose of risk assessment. It is given in Table I for a 100-m stack and for the point of highest intake.[5]

FAULT TREE

Fault-tree methodology was used for solidification plant analysis. A fault tree is a logic diagram depicting component failures and other fault events that can produce system failure. It is a binary model, convertible to a probabilistic model by means of Boolean algebra.

Figure 2 shows the basic structure of the fault tree developed for solidification plant analysis. Release of radioactivity to the environment beyond limits was chosen as the top event. The tree was divided into partial fault trees according to the physically possible release pathways:

1. release with the off-gas

2. release with ventilation air

3. release to the ground.

The partial fault trees are independent of each other. Other possible pathways are release with cooling water and with steam supply. These pathways, as well as release due to environmental impact such as earthquakes, were not considered.

RESULTS

The fault trees were evaluated with an analytical computer program called SUPERSTAR (Ref. 6). By the aid of this program, some thousands of cut sets were identified, and their frequency of occurrence was calculated. Each cut set represents one accident sequence. Only those cut sets contributing more than a certain amount to the overall risk were taken into account. This was achieved by means of a certain derived cutoff on sequence probability for each partial fault tree, as described, for instance, in Ref. 7.

The essential results of the analysis are displayed in Fig. 3. It shows the inhalation dose as a function of frequency for the most important solidification accidents. The straight lines represent those of constant risk.

The data shown in this figure illustrate the fact that major accidents occur during off-gas cleaning. The most serious ones are fire in the HEPA filter banks (G-12, 13, and 15) and failures in condenser operation (G-4 and 5). On the other hand, effects of explosions in the process equipment (e.g., hydrogen-air reaction) do not contribute very much to the overall risk.

In Fig. 3, these accident data are being compared with the annual dose commitment resulting from routine discharge of the solidification plant. Within
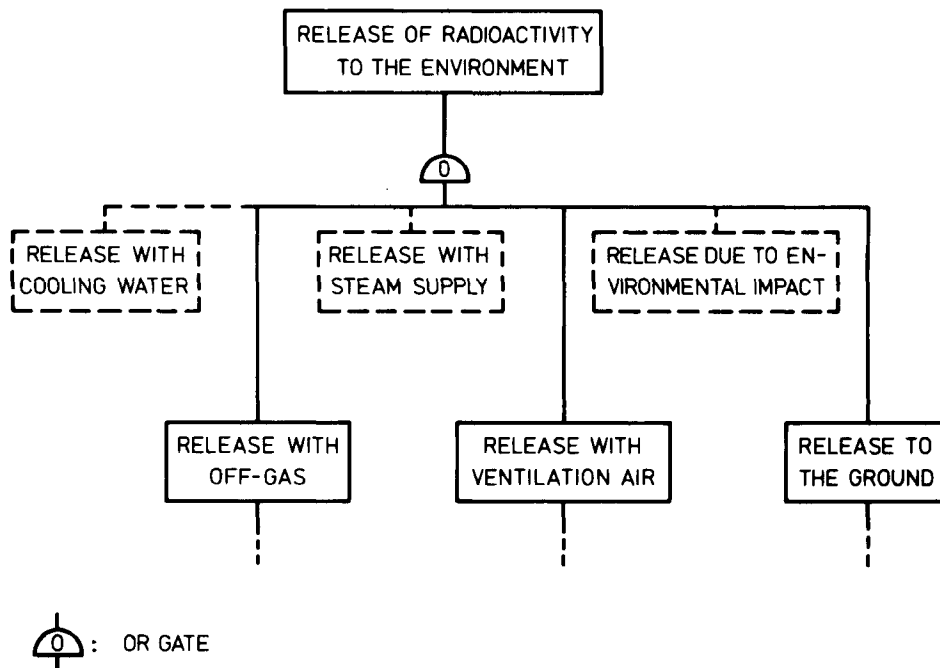
Fig. 2.   Solidification fault-tree structure.
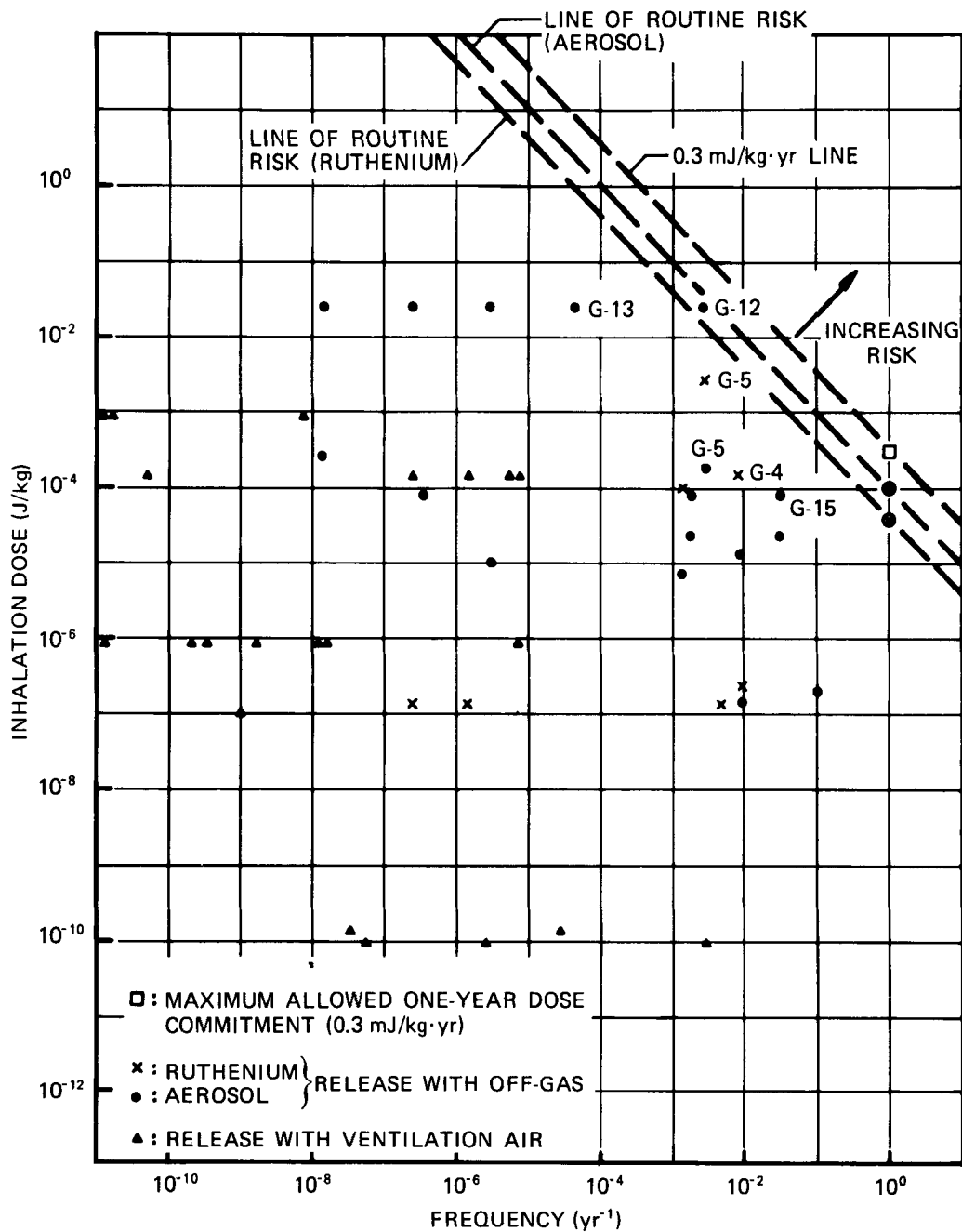
Fig. 3.   Inhalation dose versus frequency for waste solidification accidents.

the assumptions given in Table I, the routine discharge results in an annual dose of ~0.1 mJ/kg for aerosol and of ~0.04 mJ/kg for ruthenium release. Consequently, the routine risk is of the same order of magnitude or greater than the most important accident risks.

As recommended by federal regulations,[8] the maximum permissible whole-body exposure of an individual in the general population must not exceed 0.3 mJ/kg·yr. This value is also given in Fig. 3.

Finally, it is demonstrated by the analysis that fault-tree methodology involves a powerful tool for risk analysis of fuel cycle operations. Fault-tree

analysis is a deductive process. One assumes the occurrence of an event selected as the top undesired event constituting system failure. Then one works systematically backward to identify component faults that could cause the undesired event. Some advantages of this procedure are, in brief:

1. Relations between basic events can be perceived easily. This is relevant to the treatment of common mode failures.

2. Major potential weaknesses in the system are identified.

3. No assumption of initiating event is required.

This information is of particular interest for systems in the conceptual design state. Errors in design can be avoided, and major risks can be reduced by appropriate countermeasures.

REFERENCES

1. N. C. RASMUSSEN, *Reactor Safety Study*, WASH-1400, U.S. Atomic Energy Commission (1974).

2. H. J. WINGENDER, "Risk Analysis of Radioactive Waste Management Systems in Germany," *Nucl. Technol.*, **39**, 18 (1978).

3. M. J. BELL, "ORIGEN—The ORNL Isotope Generation and Depletion Code," ORNL-4628, Oak Ridge National Laboratory (1973).

4. W. COMPER, "Berechnung der Dosisfaktoren radiologisch wichtiger Nuklide," KFK 1615, Kernforschungszentrum Karlsruhe (1972).

5. K. J. VOGT and H. GEISS, "Kurzzeit- und Langzeitausbreitungsfaktoren zur Berechnung der Unweltbelastung durch Abluftfahnen," ZST-Bericht No. 198, Kernforschungsanlage Jülich (1974).

6. G. RICHTER and L. KAMARINOPOULOS, "Programm SUPERSTAR," Institut für Kerntechnik der TU Berlin (to be published).

7. T. H. SMITH et al., "A Risk-Based Fault Tree Analysis Method for Identification, Preliminary Evaluation, and Screening of Potential Accidental Release Sequences in Nuclear Fuel Cycle Operations," BNWL-1959, Battelle Pacific Northwest Laboratories (1976).

8. Verordnung über den Schutz vor Schäden durch ionisierende Strahlen (Strahlenschutzverordnung-StrlSchV), BGB 1, Z 1997 A, Bonn 20, No. 125 (Oct. 1976).

TRANSIENT ANALYSES OF A 1000-MW GAS-COOLED FAST REACTOR

DIRK WILHELM *Kernforschungszentrum Karlsruhe*
Institut für Neutronenphysik und Reaktortechnik
75 Karlsruhe, Weberstrasse 5, Federal Republic of Germany

To calculate the depressurization and flow-coastdown accidents in a 1000-MW gas-cooled fast reactor (GCFR) with a secondary steam cycle, the PHAETON2 computer code is used, the emphasis being placed on the solution of one-dimensional unstationary helium flows. The fluid dynamics equations are solved one by one by a combination of implicit and explicit methods, taking into account most of the terms of the original equations. In the case of the accidents considered, the shutdown system is always activated, and inherent actions only of the GCFR are allowed. The results show a necessity of backup pressures above 150 kPa for the depressurization accidents and a minimum circulator frequency of 5 Hz for the flow-coastdown accidents.

INTRODUCTION

During gas-cooled fast reactor (GCFR) development, questions have arisen about safety aspects that could considerably affect constructional items. In cooperation with the Kraftwerk Union Erlangen (Federal Republic of Germany), where studies for a GCFR of 1000 MW of electricity with secondary steam cycles are in progress,[1,2] computer codes are used parallel to the design work to study the effects of the overall plant construction on the required safety margins. In a GCFR, a major task is to prevent damage during loss of cooling performance in the core. In this paper, we examine this fluid dynamical problem because the geometrical configurations and characteristics of the primary helium cycle affect the history of the accident. No attention is paid to positive reactivity insertions. Thus, the computer code should primarily calculate the fluid flow in both the primary and secondary loops coupled with a point kinetic solution for neutron flux implying all major feedbacks. Neither auxiliary cooling systems nor special safety measures, such as blower speeds higher than the design speed, are regarded. It is thus the main purpose of the code to test the inherent features of the present construction. The results listed below, which show the compatibility of the PHAETON2 computer code, are very sensitive to the special design of the present reactor. Since no benchmark problem exists, the code results cannot be compared directly to any computation of a similar GCFR.

The purpose of the present investigation is not to prove the compatibility and effectiveness of any control system or secondary loop performance. The secondary loops only represent, so to speak, boundary conditions of the primary loops. Additional results of the 1000-MW reactor have been published.[3,4]

THE REACTOR

Figure 1 shows the main data of the 1000-MW GCFR presently considered. The primary helium loops are completely integrated in a prestressed concrete reactor vessel (PCRV); energy is transferred to secondary steam loops, most parts of which stand in a separated turbine building. The PCRV is located inside a secondary containment that withstands a backup pressure of more than 1 bar to cope with depressurization accidents. Figure 2 shows a model[4] of both primary and secondary loops, which can be drawn for the mathematical model described in the next section. Inside a central cavity of the PCRV, the core is suspended at a grid plate. The core as well as the axial and radial blankets consist of hexagonal subassemblies with cylindrical pins, which are vented.

Subassembly Characteristics
(first value: core subassembly, second value: blanket subassembly)

Number of subassemblies in the inner core region	85
Number of subassemblies in the outer core region	108
Number of subassemblies in the radial blanket region	180
Thickness of the hexagonal subassembly wall	4 mm
Spanner width of the subassembly wall	189 mm
Number of pins in a subassembly	271/169
Diameter of the pin	8.2 mm/13.1 mm
Pitch of the pins in hexagonal arrangement	11 mm/13.7 mm
Hydraulic diameter	7.79 mm/3.37 mm
Radius of the zero-shear-stress line of the equivalent annulus	5.78 mm/7.19 mm
Diameter of the pellet	7.14 mm/11.9 mm
Thickness of the steel cladding	0.53 mm/0.6 mm
Nusselt number of the fully developed laminar flow	9.54/2.7
Fanning friction factor of the laminar flow multiplied by the Reynolds number	27.63/15.76
Length of the smooth section of the cladding	444.3 mm/1481 mm
Length of the rough section of the cladding	1036.7 mm/0.0 mm
Length of the upper and lower axial blanket (smooth surface)	600 mm
Height of the rectangular two-dimensional roughness	0.1 mm
Width of the rectangular two-dimensional roughness	0.1 mm
Pitch of the rectangular two-dimensional roughness	0.7 mm

Reactivity Values

Reactivity constant of axial expansion	$K_A = -2.27 \times 10^{-6}$
Reactivity constant of radial expansion	$K_R = -7.47 \times 10^{-6}$
Reactivity constant of helium density variation	$K_V = -4.471 \times 10^{-3}$
Doppler reactivity	$\frac{1}{k}\frac{\partial t}{\partial T} = 0.082T^{-3/2} - 0.008T^{-1}$
Weighting factors for the Doppler feedback:	
Inner core region	0.4939
Outer core region	0.2250
Total blanket	0.2811

Design Point Characteristics

Maximum linear power in the core center	42.9 kW/m
Axial form factor	1.25
Radial form factor	1.09
Thermal power of the core and the blanket	2779 MW
Thermal power of the core	2644 MW
Power of all helium circulators	148 MW
Helium inventory	10 156 kg
Maximum helium pressure	120 bar
Total pressure drop of a loop with the core	6 bar
Pressure drop in the core	5 bar
Total helium flow through the core	1868 kg/s
Core inlet helium temperature	547 K
Mixed medium core outlet temperature	832 K
Total steam flow through the heat exchangers	1088 kg/s
Feedwater pressure	209 bar
Feedwater temperature	443 K
Hot-spot factor of the helium temperature difference	1.17
Hot-spot factor of the heat transfer fluid wall	1.39
Hot-spot factor of the heat generation in the pellet	1.17

Constant Properties

Specific heat capacity of helium	5.22 kJ/(kg K)
Ratio of specific heat of helium	1.667
Prandtl number of helium	0.667
Gas constant of helium	2.078 kJ/(kg K)
Density of the pellets	9113.4 kg/m³
Density of steel (cladding, subassembly wall)	8000 kg/m³
Thermal conductivity of the pellets	1.9×10^{-3} kW/(m K)
Thermal conductivity of steel	2.284×10^{-2} kW/(m K)
Specific heat capacity of the pellets	0.3349 kJ/(kg K)
Specific heat capacity of steel	0.5862 kJ/(kg K)

Fig. 1.   Main data of the 1000-MW GCFR.

1. REACTOR
2. RESUPERHEATER
3. STEAM GENERATOR
4. CIRCULATOR TURBINE CONTROL VALVE
5. CIRCULATOR TURBINE
6. HELIUM CIRCULATOR

7. NODE OF STEAM LOOP
8. NODE OF HELIUM LOOP
9. MAIN TURBINE CONTROL VALVE
10. MAIN STEAM TURBINE
11. FEEDWATER INLET

P1 THROUGH P12 PLENUM OF HELIUM LOOP
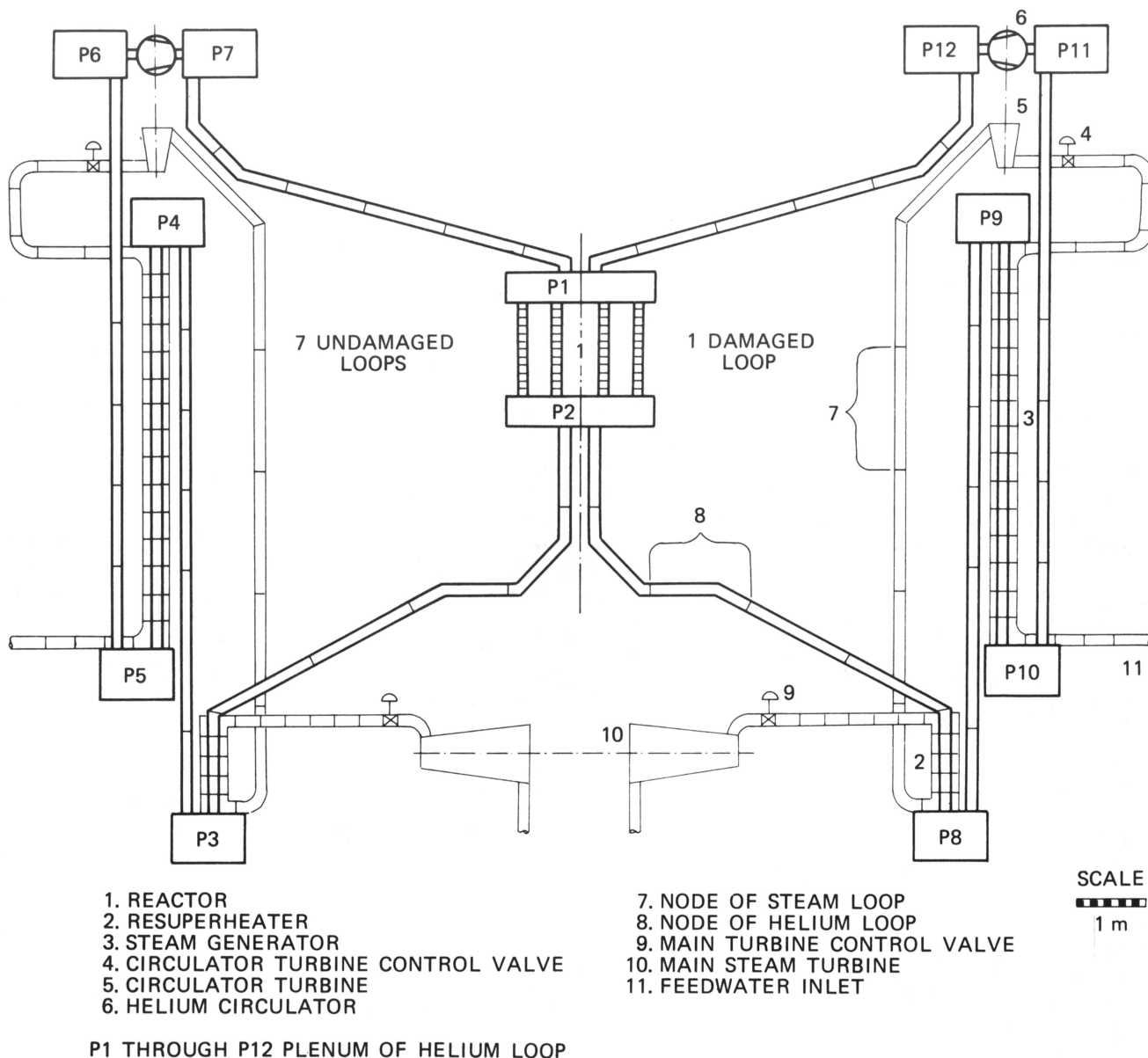
Fig. 2.   Model of the coolant loops of the 1000-MW GCFR.

Fuel pellets are surrounded by a steel cladding whose surface is roughened by transversal ribs[5] in the lower part of the pins. Helium passes downward through the core and enters a huge exit plenum. Helium-water heat exchangers with eight parallel loops are located in eight circumferential cavities. The helium flow is so directed that upward boiling occurs in the water of the secondary loops. The helium blowers are directly connected to one-stage steam turbines driven by the steam of the secondary loops. All machines stand inside the circumferential cavities, with the feedwater entering the PCRV and superheated steam leaving it for a main turbine connected to the electrical generator.

THE MODEL

Presuming that we shall solve the fluid dynamics equations in a one-dimensional form and that we shall separate the solution of the momentum and mass equations from that of the energy equation, we can build the model of Fig. 2 representing seven undamaged loops and one loop with a leakage for depressurization accidents. Parallel to these two primary model loops, the secondary loops shown in the figure must be established. Both primary loops end in the core inlet and outlet plenum connected by four channels, which constitute subassemblies in different core or blanket positions.

The cavities Pl through Pl2 represent points having constant variables of state for helium. They are connected by tubes that represent lines of constant mass flow. By this model, one can solve the mass and momentum equations. The tubes are divided into nodes of constant physical properties for helium in which the energy equation is solved mainly to calculate the heat exchange with the adjacent walls. Methods are described in the next section. Any different partitioning of cavities and nodes is possible to fit the needs of the loops being modeled.

The model also has to take into account the different characteristics of the helium blower and blower turbine and the energy transfer via the shaft connecting both machines. The model will allow us to distinguish between as many levels of power in the core as there are nodes (48 in Fig. 2), but feedback will be possible only by point kinetics. Controls from outside that, due to constructional optimization, are only possible with the secondary loops will be regarded as inputs for the computer code.

METHODS

This section gives a quick view of two of the main subroutines of the PHAETON2 computer code, written in FORTRAN IV and run on an IBM/370. One of the principal features of solving the fluid dynamics equations has already been mentioned in the previous section.

By the model described, we have separated the three conservation equations into two parts to be solved, one by one, admitting the drawback that shock waves cannot be considered. Compressibility effects will only be considered in the cavities that are treated as points. This method reduces calculation expenditure because cavities and nodes can be planned where they are really needed. Many nodes will be established where much energy is exchanged with the adjacent walls, cavities will be located in those regions where plenums exist, and links will be modeled for parts of large pressure drops. Normally, the number of cavities and connecting links is considerably lower than the number of nodes for the energy equations.

For a cavity, we have to solve the mass equation and a simple form of the energy equation, since the cavity has adiabatic walls. (Variables not defined here are defined in the Nomenclature on p. 39.)

$$\frac{\partial \rho}{\partial t} = -(1/V) \int_{\text{(plenum)}} d\dot{m} \quad , \qquad (1)$$

$$c_v \frac{\partial}{\partial t}(\rho T) = -(c_p/V) \int_{\text{(plenum)}} d(\dot{m}T) \quad , \qquad (2)$$

with the values for the density and temperature, ρ and T, being mixed mean values on the left side of

the equations, and with an integration over the boundaries of the plenum where an arbitrary number of mass flows, $\dot{m}$, links plenum with plenum. Along the links, we have to solve the momentum equation,

$$\frac{\partial \dot{m}}{\partial t} = \left[1 \Big/ \int_{\text{(link)}} dx \right] \left[- \int_{\text{(link)}} A\,dp + \dot{m}^2 \int_{\text{(link)}} \frac{d(\rho A)}{(\rho A)^2} \right.$$
$$\left. - g \int_{\text{(link)}} \rho A \sin\gamma\,dx - \int_{\text{(link)}} K_v A\,dx \right] \quad , \qquad (3)$$

with an integration over all those nodes having different helium properties of which a link consists. The force per helium volume, K_v, which acts on the adjacent walls, can be calculated with the help of steady-state friction factors[5-7] of high complexity.

Equations (1), (2), and (3) describe the hydraulic network of the model, taking into account all terms of the basic differential equations. Effects of natural convection, for example, will always be calculated, although they are negligible in case of superimposed forced convection. However, they allow a continuous change from one condition to the other.

We solve the system of equations for the hydraulic network using an implicit method,[8] y being a vector of state for $(\rho, T, \dot{m})$ and

$$\frac{d}{dt} y = f_a(y) \qquad (4)$$

being the basic ordinary differential equations. The vector function f_a is now taken at the time $t + dt$, where the vector has reached $y + dy$, transforming it into f_b,

$$\frac{d}{dt} y = f_b(y + dy) \qquad . \qquad (5)$$

Writing the right side in terms of the original vector function, $f_b(y + dy) = f_a + df_a$, we obtain

$$f_a\,dt = dy - df_a\,dt \quad . \qquad (6)$$

Since df_a is a function of the vector of state, we can write

$$f_a\,dt = \mathbf{B}\,dy \quad .$$

By inverting the matrix $\mathbf{B}$ with the elements

$$b_{ik} = -\frac{(\partial f_a)_i}{\partial y_k} dt$$

and

$$b_{ii} = 1 - \frac{(\partial f_a)_i}{\partial y_i} dt \quad ,$$

we can find a solution for y.

Since the vector functions of ρ and T can be substituted by that of $\dot{m}$, we solve the whole hydraulic network by

$$f_a(\dot{m})dt = \mathbf{B}d\dot{m} \quad . \tag{7}$$

Solving it for a number of n links, we have to invert a matrix of n^2 elements instead of $(3n)^2$ without reduction to one unknown variable. This saves more than 90% of calculation time.

In the secondary steam loops, the mass flow is calculated simply by a mass balance of the inventory of the boiler, which is supposed to be the only compressible part of the secondary loop. Thus, the inlet and outlet mass flows of the boiler will be constant all over the adjacent piping systems.

The solution of the hydraulic network imposes a constant mass flow on each of the links. We divide a link into nodes of constant geometry in which we assume constant helium properties as a function of a linear variation of pressure between both adjacent cavities and the temperature at the beginning of a time step. Assuming a constant wall temperature (T_w) over the length of the node (l), a step change of the wall temperature at the beginning of a time step $(t = 0)$, a linear variation (θ) over a time step of the inlet temperature into a node, a linear variation (P) over the time step of the superimposed pressure (p) and the helium temperature (T) as a function of axial length (x), the energy equation becomes

$$\frac{\partial T}{\partial t} + w\,\frac{\partial T}{\partial x} = \nu\left(T_w + \frac{1}{\nu\rho c_p}\frac{dp}{dt} - T\right) , \tag{8}$$

with $\nu = 1/(\rho A c_p R)$;

$$T_w + \frac{1}{\nu\rho c_p}\frac{dp}{dt} = \begin{cases} T_{wL} & \text{for } t \leqslant 0 \\[2mm] T_w + \dfrac{1}{\nu\rho c_p}P & \text{for } t > 0 \quad ; \end{cases}$$

$$T(x = 0) = \begin{cases} T_{iL} & \text{for } t \leqslant 0 \\[2mm] T_{iL} + \theta \cdot t & \text{for } t > 0 \quad . \end{cases}$$

Here, terms of inertia as well as of compressibility have been neglected because of the definition of a link. The thermal resistance, R, between the fluid and wall is calculated using steady-state correlations[6] for heat transfer coefficients that are functions of all parameters given in the literature (for example, roughened surfaces[5]) and are capable of coping with all kinds of heat transfer (for example, radiation in the core). Separation into a steady-state and transient part,

$$T(t,x) = T_{st}(x) + T_{tr}(t,x) , \tag{9}$$

yields two differential equations. The steady-state part is

$$w\,\frac{dT_{st}}{dx} = \nu\left(T_w + \frac{1}{\nu\rho c_p}\frac{dp}{dt} - T_{st}\right) , \tag{10}$$

with

$$T_{st} = \begin{cases} T_{iL} & \text{for } x = 0 \\[2mm] T_{oL} & \text{for } x = l \end{cases}$$

and

$$T_w + \frac{1}{\nu\rho c_p}\frac{dp}{dt} = T_{wL} \quad .$$

The transient part is

$$\frac{\partial T_{tr}}{\partial t} + w\,\frac{\partial T_{tr}}{\partial x} = \nu\left(T_w + \frac{1}{\nu\rho c_p}\frac{dp}{dt} - T_{tr}\right) , \tag{11}$$

with

$$T_{tr}(x = 0) = \theta \cdot t \quad \text{for } t > 0$$

and

$$T_w + \frac{1}{\nu\rho c_p}\frac{dp}{dt} = \begin{cases} 0 & \text{for } t \leqslant 0 \\[2mm] T_w + \dfrac{1}{\nu\rho c_p}P - T_{wL} & \text{for } t > 0 \quad . \end{cases}$$

The solution of Eq. (10) is obtained immediately:

$$T_{st}(x) = T_{wL} - (T_{wL} - T_{iL})\exp\left(-\frac{\nu}{w}x\right) . \tag{12}$$

To solve Eq. (11), we transform into Laplace-space and back again, obtaining

$$T_{tr}(t,x) = [1 - \exp(-\nu t)]\left(T_w + \frac{1}{\nu\rho c_p}P - T_{wL}\right)$$
$$\text{for } t \leqslant \frac{x}{w} \tag{13}$$

and

$$T_{tr}(t,x) = [1 - \exp(-\nu t)]\left(T_w + \frac{1}{\nu\rho c_p}P - T_{wL}\right)$$
$$+ \theta\left(t - \frac{x}{w}\right)\exp\left(-\frac{\nu}{w}x\right) - \left\{1 - \exp\left[-\nu\left(t - \frac{x}{w}\right)\right]\right\}$$
$$\times \exp\left(-\frac{\nu}{w}x\right)\left(T_w + \frac{1}{\nu\rho c_p}P - T_{wL}\right)$$
$$\text{for } t > \frac{x}{w} \quad . \tag{14}$$

As we see, the choice of one of these solutions depends on the value of the convection velocity, w. The steady-state and transient solutions will be combined by Eq. (9).

Thus, the outlet temperature of each node, which we find always downstream at $x = l$ and $t = \Delta t$, is only a function of the history of that part of the fluid that has been already inside the node at $t = 0$. If, for example, the velocity is very high, the basic temperature for the solution will be interpolated linearly between the inlet temperature at $t = \Delta t$, which is equivalent to the outlet temperature of the adjacent node and the inlet temperature at $t = 0$. If the velocity is very low, the basic temperature will be that

of a supposed helium particle inside the node that was located at a distance $w \cdot \Delta t$ from the outlet at $t = 0$. Even under extreme conditions, the numerical solution can always be stable. Using the energy balance over a node and time step, a mixed medium temperature of helium can be calculated that will be the reference temperature for the heat transfer and pressure drop correlations.

In the secondary steam loop, a similar procedure is used. As the enthalpy of water is the main unknown variable, an iteration over the water temperature is necessary. The reason is that the enthalpy and temperature are linked by complicated steam tables. Thus, a major simplification in Eqs. (10) and (11) is necessary that produces a linear variation of enthalpy over the distance of a node.

DEPRESSURIZATION ACCIDENTS

It is supposed that the seal of a big plug closing one of the peripheral PCRV cavities is failing. This leads to a mass flow out of plenum P11 in Fig. 2. Assuming a constant cross-section area of the leakage, the pressure in the primary loop will drop nearly exponentially, allowing a time constant of depressurization to be defined.

Immediately after detection of the leakage, the reactor will be scrammed and the main valves (see 4 and 9 in Fig. 2) of the secondary loop will be closed by a specified percentage. This leads to a reduction of the blower speed to avoid severe undercooling of the scrammed core while the density of helium is still high. As the pressures in the primary cycle reach that of the secondary containment, the blower speed must be increased to a maximum to produce as much mass flow in the core as possible to ensure shutdown heat removal. Two different shutdown power functions are used for the core and the blanket, since they contain different amounts of breeding and fission products.

Figure 3 shows results of a depressurization accident with a time constant of 30 s. The emphasis is placed on avoiding steep temperature ramps at the beginning of shutdown. The maximum nominal cladding temperature in the reactor center is plotted versus time with the relative core power during scram and the blower speed as the main parametric variables. Leakage occurs at time $t = 1$ s, and the scram and secondary loop valves will be activated at time $t = 2$ s.

It is not necessary to close the valves as fast as possible. Figure 3 shows a relative optimum among
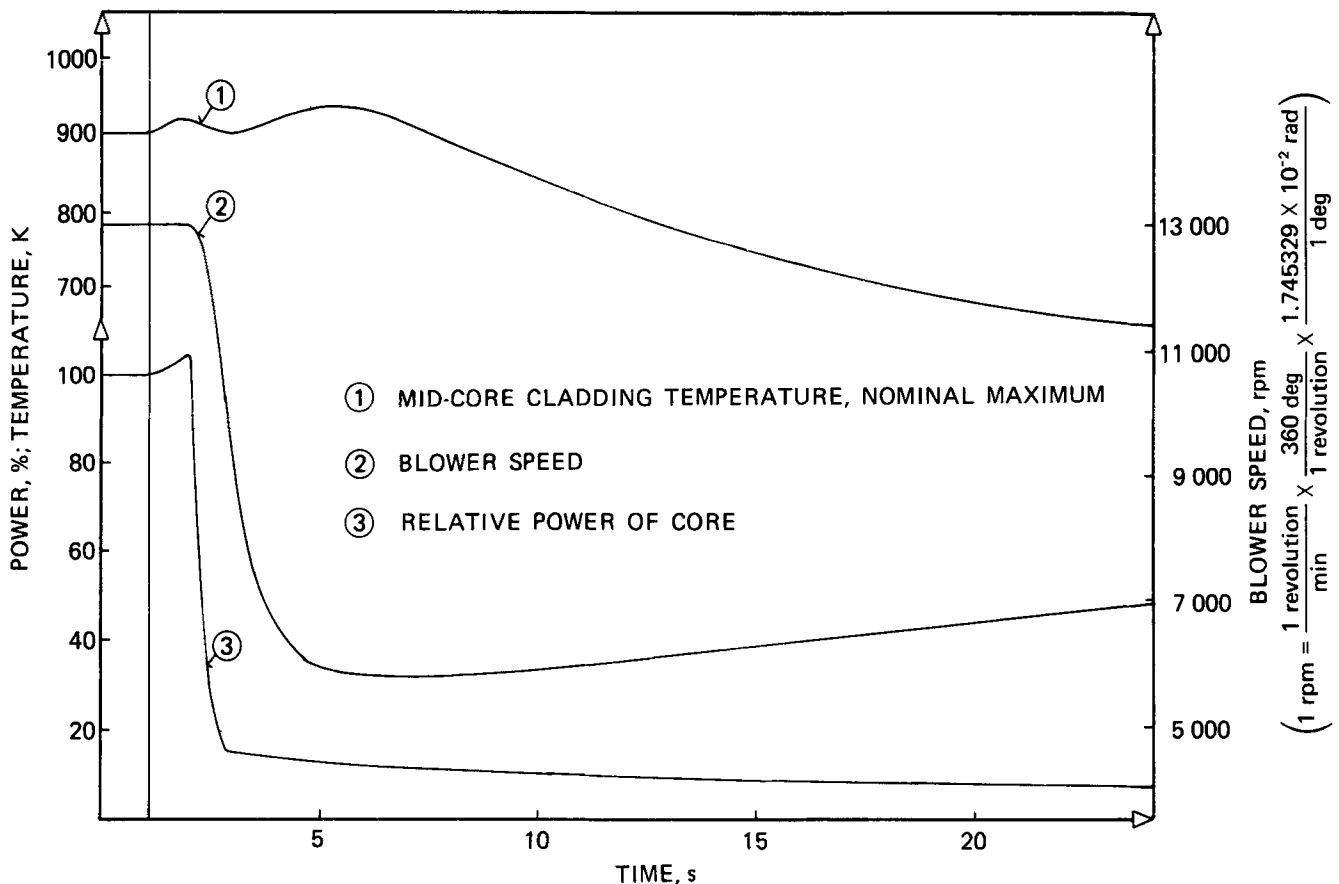

Fig. 3. Depressurization accident with scram (time constant is 30 s, 60 rpm = 1 Hz).

several test runs, assuming that the sectional area of the circulator turbine control valve is reduced linearly down to 3% between time $t = 2$ s and time $t = 3$ s. In the same interval, feedwater decreases linearly down to 9% and stays constant at this value for the rest of the time, and the main steam turbine is passed with a resulting exit pressure of the main turbine control valve of 400 kPa. The highest temperature gradient will be 25 K/s at the downward slope.

Figure 4 shows results of a depressurization accident with a time constant of 30 s and a backup pressure in the secondary containment of 300 kPa (3 bar). This is an inherent feature of the design if the helium is released into a secondary containment of an adjusted free volume that can withstand the requested internal pressure. The beginning of the scram is not optimized as in Figs. 2 and 4. The maximum cladding temperatures are plotted together with the mean input variables, pressure, and blower speed. As the pressure reaches that of the secondary containment, the blower speed has been increased to the design level. Temperatures rise to a maximum after 4 min. The pressure balance at the leakage will be reached after $2\frac{1}{2}$ min, and the diffusion of air into the primary loop cannot be calculated. After 2 min, the flow regime is at the lower end of the transition region near the laminar flow.

As the energy amount to be transferred from the pin to helium is rather low after shutdown, high cladding temperatures exist at points where the helium temperatures are high, i.e., in the lower part of the pin at the interface between the core and lower axial blanket. The core inlet temperature decreases very slowly, since the heat sink at the boiler performs at a constant feedwater temperature.

Figure 5 shows the results of a depressurization accident with a time constant of 30 s and a backup pressure of 150 kPa (1.5 bar). In Fig. 5a, the input variables, blower speed, pressure, and power are plotted. They show that the backup pressure of 150 kPa will be reached after 3 min. Consequently, in Fig. 5b, the temperatures of the cladding represented by the uppermost curve for the hot spot and the next below for nominal maxima rise continuously after 50 s and reach critical values after 6 min. The reactor outlet temperature follows the characteristic of the cladding temperature, while the cladding temperature in the radial blanket and the reactor inlet temperature remain nearly constant. A laminar flow regime in the core will be reached after $2\frac{1}{2}$ min. Since the laminar temperature profile will require considerably longer distances to develop than a turbulent one, the effects on the maximum cladding temperatures were investigated. Since the highest temperatures always occur at the reactor outlet, no reduction of the critical clad temperatures was observed. Considering the velocity profile, the hydrodynamic entry length is, even in a laminar regime, always shorter than the axial blanket at the upper end of the pin. This has no effect on the heat transfer in the core region where consequences are conceivable on the critical clad temperatures. The density and the resulting mass flow together with the rather low heat transfer coefficients in the core are not capable of keeping the cladding temperature below the limits of failure. The Nusselt number of a fully developed laminar flow was calculated to be 9.5,
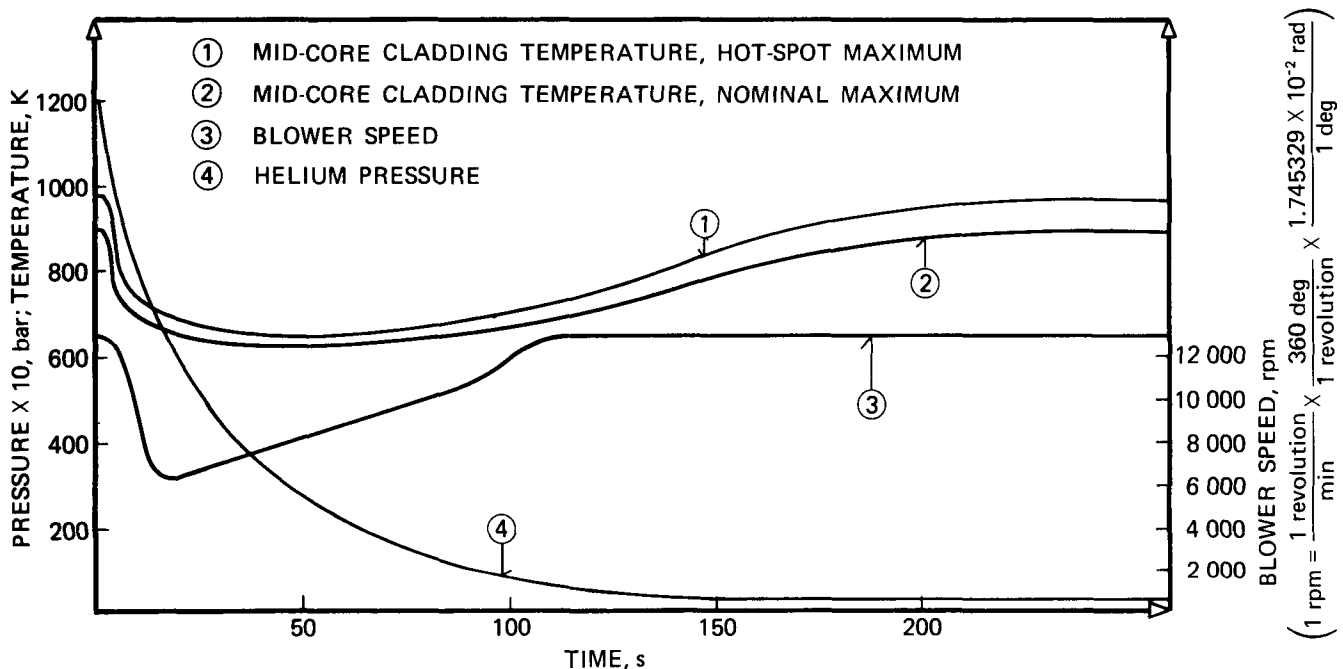

Fig. 4.   Depressurization accident with scram [time constant is 30 s, backup pressure is 300 kPa (3 bar), 60 rpm = 1 Hz].
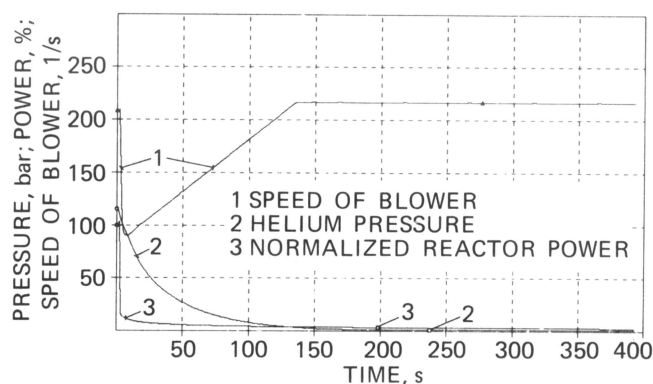
Fig. 5a. Depressurization accident with scram [time constant is 30 s; backup pressure is 150 kPa (1.5 bar)].
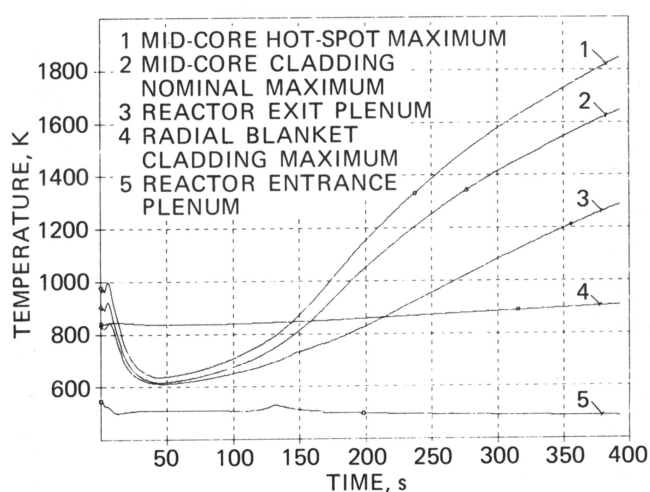

Fig. 5b. Depressurization accident with scram [time constant is 30 s; backup pressure is 150 kPa (1.5 bar)].

and interpolation routines were used for the transition region between turbulent and laminar flow. Although all major features for a successful efficient shutdown heat removal were studied, it should be stated that the blower speed could possibly be increased if the design would allow so and that auxiliary loops are not taken into account. But these are not inherent features of the present design. Depressurization constants of 30 s are very pessimistic. For most PCRV designs, one can admit a failure that could only produce a minimum time constant of 100 s or higher. With these parameters, the peak cladding temperatures would be considerably lower. With the present parameters, we can state a necessity of backup pressures well above atmospheric pressure.

FLOW-COASTDOWN ACCIDENTS

Accidents occurring at a normal design pressure level but with failing blowers can be caused by loss of

the driving power for the blowers. The rupture of blower blades and the loss of water for lubrication of the blower shaft will not be considered here, since effects on the safety are similar to that of total loss of power and the probability is considerably lower.

Figure 6 shows results of a flow-coastdown accident in which natural convection will be used to remove the shutdown heat. For this purpose, the center of the boiler, which is normally situated ~1 m below the center of the core in Fig. 2, has been raised 10 m above the core, which is possible by connecting separate PCRVs, containing the heat exchangers, to the main PCRV accommodating the reactor core. At time $t = 1$ s, all eight blowers lose power and the inertia of the shaft leads to a loss of blower speed with a time constant of a few seconds. The inertia of the circulator and turbine, which are connected to the same shaft, is $6.7 \cdot 10^{-3}$ kJ s^2, which is very small. To obtain the result in Fig. 6, this value has been raised by a factor of 5. The friction losses for the circulator at lower speed are probably underestimated. It is thus supposed that the circulator reaches a standstill at time = 115 s, which is forced by a linear decrease of speed starting at time = 100 s.

Although the blower approaches the stall limit as its speed reaches very low values, instabilities cannot be noticed. If the frequency of the shaft is smaller than 1 Hz, the circulator is supposed to behave simply like a throttle valve. This will generally occur while a pressure difference still builds up across the blower. Consequently, the mass flow reverts in the blower, leading to a reversal in the whole loop.

A maintenance of the flow direction could only be imagined if the pressure difference across the blower would revert before a standstill of the shaft, but this would need a very slow decrease in circulator speed. On the other hand, the calculation cannot take into account all the instabilities of the blower. So it is very probable that the mass flow reverts and a natural convection is initialized, which leads to an upward flow through the core attaining 3.4% of the design value. Consequently, the cladding temperatures rise to a maximum after the flow reversal. In case flow reversal cannot be avoided, the results are more favorable if the reversal proceeds very quickly. This is in fact obtained with an immediate stop of the circulators. All loops with less favorable configurations will have considerably higher maxima of the cladding temperatures, since the natural convection is strongly influenced by the geodetical heights of the heat source and sink. Calculations for a standing core have shown the possibility of maintaining the flow direction upward through the core when the circulator speed decreases very slowly. This can even be observed with the production of instabilities by the circulators running at the stall limit. The results in Figs. 6 and 7 anticipate a simultaneous interference in all eight loops. If only one loop circulator can be

1. HELIUM MASS FLOW THROUGH THE CORE
2. HELIUM MASS FLOW THROUGH THE CIRCULATOR
3. HOT-SPOT CLADDING MAXIMUM,
   CENTRAL SUBASSEMBLY
4. NOMINAL CLADDING MAXIMUM,
   CENTRAL SUBASSEMBLY
5. NOMINAL CLADDING MAXIMUM,
   RADIAL BLANKET
6. REACTOR OUTLET PLENUM
7. REACTOR INLET PLENUM
8. HELIUM PRESSURE
9. CIRCULATOR SPEED
10. MASS FLOW OF ONE SECONDARY LOOP
11. GENERATED POWER (CORE)
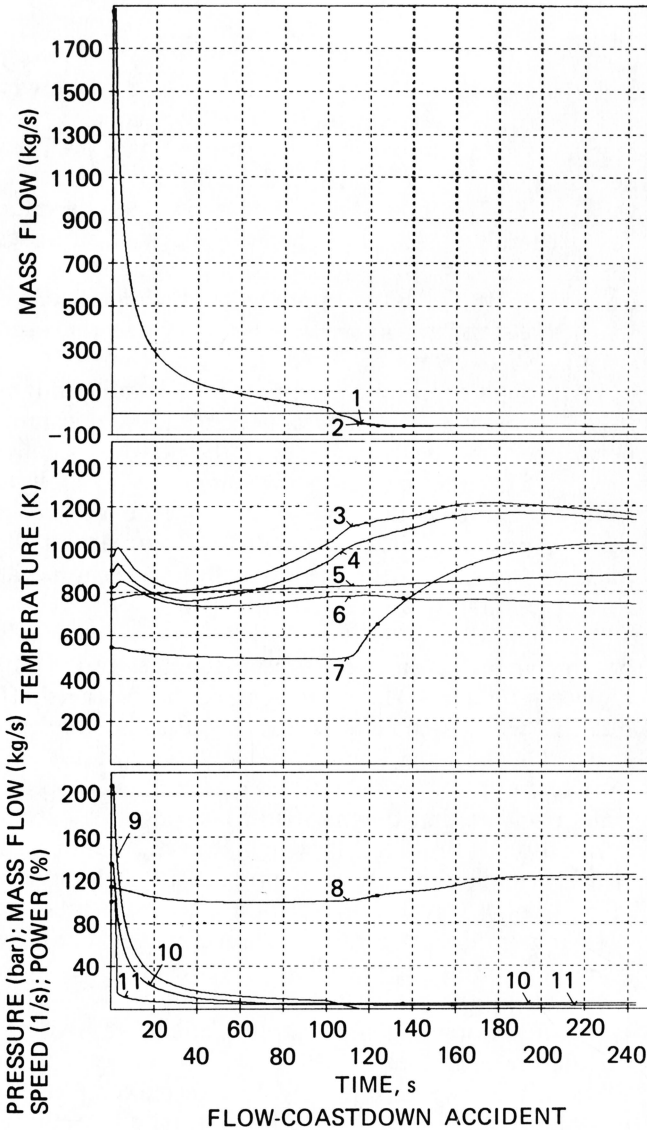
Fig. 6. Flow-coastdown accident with scram and natural convection (1 bar = 100 kPa).

Fig. 7a. Flow-coastdown accident with scram and minimum circulator speed of 3.33 Hz (200 rpm).

1. MID-CORE CLADDING TEMPERATURE,
   HOT-SPOT MAXIMUM
2. MID-CORE CLADDING TEMPERATURE,
   NOMINAL MAXIMUM
3. CORE OUTLET TEMPERATURE
4. AVERAGE CLADDING TEMPERATURE
   OF RADIAL BLANKET
5. CORE INLET TEMPERATURE
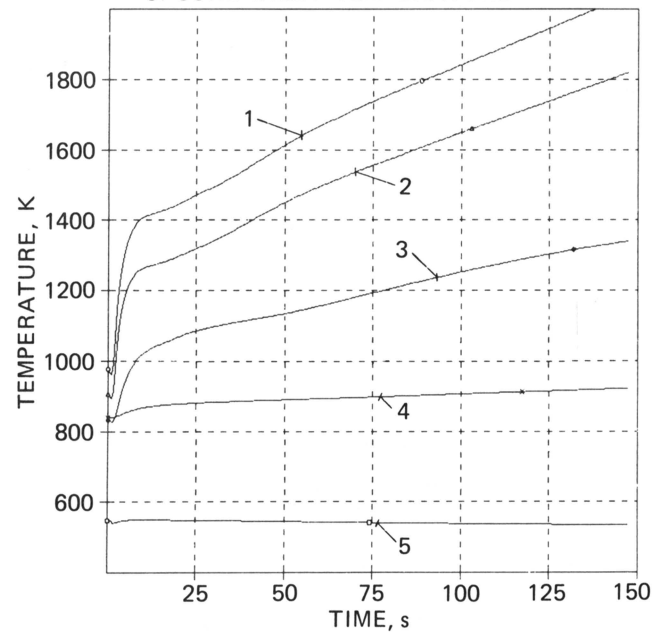
Fig. 7b. Flow-coastdown accident with scram and minimum circulator speed of 3.33 Hz (200 rpm).

kept running, the damaged loops are closed by automatic isolation valves and the shutdown heat can easily be removed.

Figure 7 shows results of a flow-coastdown accident with the normal geometrical configuration as in Fig. 2 and a loss of power for all blowers. Since the bearing of the blower shaft is lubricated by water with a tangential velocity, we can assume that the blower's frequency will not drop below 3.33 Hz (200 rpm). This leads to a nearly constant mass flow after 50 s, as shown in Fig. 7a. The blower will operate near the stall limit, so that uncertainties in its characteristics must be watched. Many test runs were

performed to examine mathematical instabilities while taking into account blower characteristics with a hysteresis beyond the stall limit. Since in the solution of the hydraulic network an instability once induced by unsteady characteristics can be fed back and leads to unrealistic results, the hysteresis has been neglected, and for each pressure difference imposed, the blower code will calculate one and only one mass flow. Figure 7b shows the resulting cladding temperatures, with the upper curve standing for the hot-spot values and the one below for the nominal values. Following this order, the core outlet temperature, the cladding temperature in the radial blanket, and the core inlet temperature are plotted.

The mass flow drops immediately after the accident, whereas the scram will be delayed by 1 s. The inertia of the circulator and turbine is $6.7 \cdot 10^{-3}$ kJ s². Consequently, the time constants of mass flow reduction are so small that the energy produced in the core cannot be removed normally. The temperatures rise very fast until the shutdown heat level reaches the level of the mass flow. After half a minute, a laminar flow regime will be reached, and the heat transfer performance leads to a further increase of cladding temperatures.

Consequently, the blower's frequency of 3.33 Hz (200 rpm) is not sufficient to prevent the cladding temperature from reaching critical values. Further calculations show that this can be avoided when the minimum frequency is increased to 5.0 Hz (300 rpm). Besides this, the great temperature increase during the first 10 s can be prevented by increasing the inertia of the circulator and turbine.

CONCLUSION

The PHAETON2 computer code has been proven to be practicable for calculating accidents of a 1000-MW GCFR with secondary steam cycles. For all accidents considered, the shutdown of the reactor and the specific time constants of the loops allow the use of one-dimensional fluid dynamics equations and point kinetics equations. In case of depressurization accidents, the backup pressure has proven to be the most important inherent feature, which, for the present pessimistic depressurization time constant of 30 s, must be greater than 150 kPa. As the minimum flow regime is near the interface of laminar to transition flow, the design of the subassemblies affects the resultant maximum cladding temperatures considerably.

In case of flow-coastdown accidents, the residual minimum blower frequency must be 5 Hz or more to remove the shutdown heat sufficiently. An additional inherent safety margin would be the increase of the circulator inertia. If all circulators would run down to zero, the natural convection of a special loop design could cope with the shutdown heat. In this case, the steam generator would have to be elevated 10 m above the core.

NOMENCLATURE

A = cross-section area, m²

$\mathbf{B}$ = matrix

b = matrix elements

c_v = specific heat capacity at constant volume, kJ/ (kg K)

c_p = specific heat capacity at constant pressure, kJ/ (kg K)

f = vector function

g = standard acceleration, m/s²

K_v = force per volume acting on a wall, kJ/m⁴

l = length of node, m

$\dot{m}$ = mass flow, kg/s

P = pressure variation with time, kJ/(s m³)

p = pressure, kJ/m³

R = thermal resistance, m·K/kW

t = time, s

T = absolute temperature, K (without subscript = helium)

V = volume, m³

w = velocity, m/s

x = axial distance, m

y = vector of state

γ = angle of inclination with respect to a horizontal plane

Δ = step interval

ν = $1/(\rho A c_p R)$, 1/s

ρ = density, kg/m³

θ = inlet temperature variation with time, K/s

Subscripts

i = in

L = when $t = 0$

o = out

st = steady state

tr = transient

w = wall

REFERENCES

1. "1000 MWe—Gasgekühlter Schneller Brüter Referenz- und Sicherheitsstudie," unpublished report, Kraftwerk Union Erlangen (1975).

2. C. A. GOETZMANN and M. DALLE DONNE, "Design and Safety Studies for a 1000 MW Gas Cooled Fast Reactor," *Proc. ANS Fast Reactor Safety Mtg.*, Beverly Hills, California, April 1974, CONF-740401-P2, U.S. Atomic Energy Commission (1974).

3. D. WILHELM, "Untersuchungen des Störfallverhaltens des GCFR von 1000 MWe mit dem digitalen Rechenprogramm PHAETON2," KFK 1276/3, Gesellschaft für Kernforschung, Karlsruhe (1976).

4. D. WILHELM, "The PHAETON2 Computer Code for Analyzing Accidents in a 1000 MWe Helium Cooled Fast Reactor," KFK 2561, Gesellschaft für Kernforschung, Karlsruhe (1977).

5. M. DALLE DONNE and E. MEERWALD, "Heat Transfer and Friction Correlations for Surfaces Roughened by Transversal Ribs," NEA Core Performance Specialist's Meeting, Studsvik (1973).

6. H. KAWAMURA, "Transient Hydraulics and Heat Transfer in Turbulent Flow," *Nucl. Technol.*, **30**, 246 (1976).

7. K. REHME, "Laminarströmung in Stabbündeln," *Chemie-Ingenieur-Technik 43*, 17 (1971).

8. T. A. PORSCHING, J. H. MURPHY, and J. A. REDFIELD, "Stable Numerical Integration of Conservation Equations for Hydraulic Networks," *Nucl. Sci. Eng.*, **43**, 218 (1971).

CONTAINMENT NEGATIVE PRESSURE EVALUATION

STEPHEN W. WEBB *Gilbert Associates, Inc.*
Applied Engineering Analysis Department, P.O. Box 1498
Reading, Pennsylvania 19603

The decrease in containment pressure following inadvertent actuation of the containment sprays has been evaluated. The depressurization occurs in two definite phases involving the short-term depressurization due to mass transport and the long-term depressurization due to heat transfer. Either phase may determine the maximum depressurization. Simple models may overestimate the maximum depressurization by 50% or more; therefore, transient models are needed to avoid unnecessary conservatism.

I. INTRODUCTION

The containment system for nuclear reactors must be designed to withstand appropriate positive and negative pressure differentials while maintaining functional integrity. The maximum positive pressure is caused by a pipe rupture inside the containment and receives detailed analysis involving the mass/energy releases and containment response characteristics. The maximum negative pressure is the result of inadvertent operation of containment heat removal systems, including the containment fan cooler units and containment sprays.

In general, the heat removal capability from inadvertent operation of sprays is much greater than inadvertent fan cooler operation. Various errors and/or malfunctions may initiate inadvertent operation of the containment sprays, including manual operation by the operator in the control room or a signal to operate the spray loop discharge valve during inservice testing. The causes of inadvertent spray actuation depend on the individual plant; care should be used in the plant design to minimize the possibility of inadvertent spray. Vacuum relief systems such as vacuum breakers are sometimes employed to limit the maximum negative pressure. The

pressure response from inadvertent spray operation discussed in this paper applies to all containment designs; however, the details involving vacuum relief analyses are not included.

Inadvertent operation of the containment sprays causes depressurization in the containment in two distinct phases—the short-term phase and the long term phase. In the short term, evaporative cooling causes a rapid depressurization within the first few seconds of spray operation. The latent energy required for evaporation of the spray droplets is supplied by the air causing a drop in containment pressure and temperature. The short-term phase continues until the containment atmosphere becomes saturated. Subsequently, the long-term phase involving heat transfer among the containment atmosphere, spray water, and containment structures determines the depressurization rate. The depressurization transient for a range of initial relative humidities is shown in Fig. 1 as calculated by the CONTEMPT-LT code.[1]

Simple calculations are often used to evaluate the containment negative pressure used for design purposes. These simple calculations, however, may overestimate the maximum depressurization by more than 50%; this situation could lead to unnecessary overdesign of the containment. The parameters involved in a transient analysis are discussed below. The short-term and long-term phases are discussed separately.

II. SHORT-TERM PHASE

During the short-term phase of the transient, the spray water enters the containment atmosphere and evaporates.[a] The energy required for evaporation of

---

[a]Assuming, of course, that the atmosphere is initially at <100% relative humidity. If the initial relative humidity is 100%, the short-term phenomena discussed do not take place.

$P_0 = 1.033$ kg/cm^2 (14.7 psia)
$T_0 = 49°C$ (120°F)
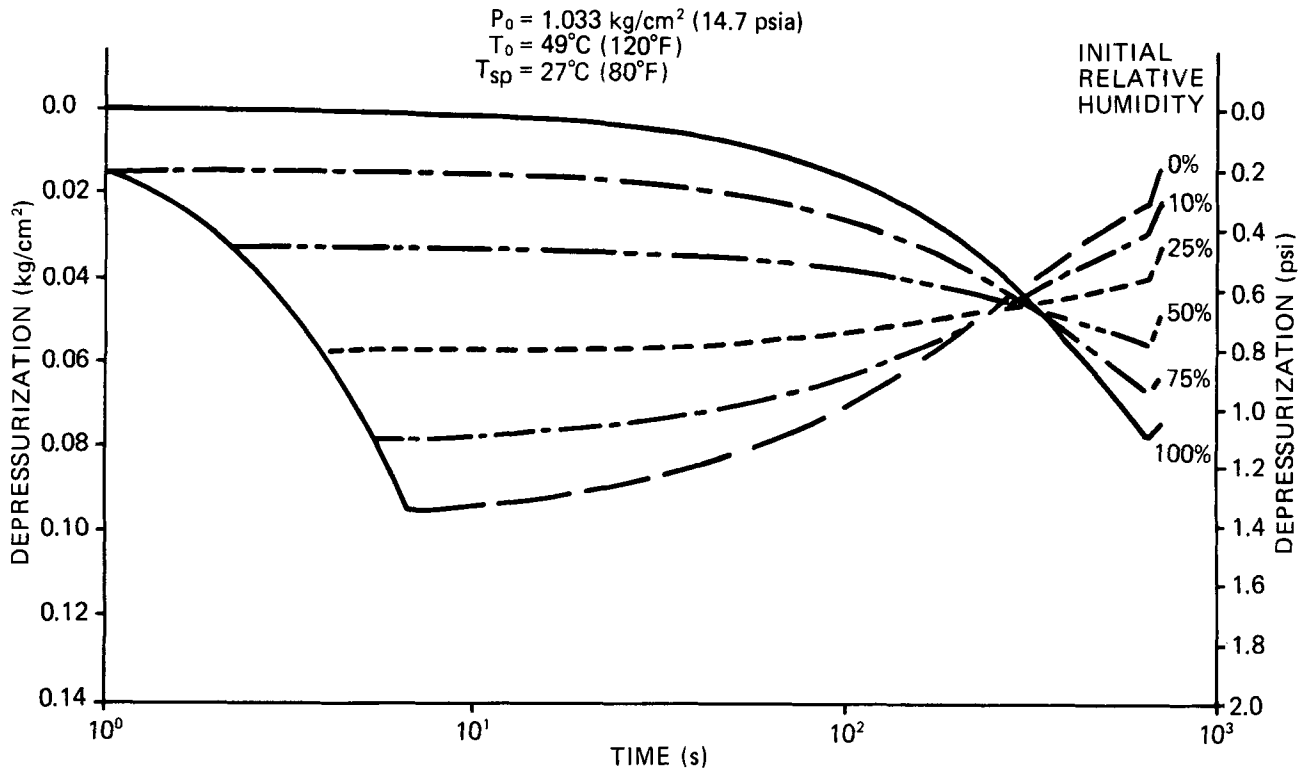$T_{sp} = 27°C$ (80°F)

Fig. 1.   Containment depressurization transients.

the drop must be supplied by the air, resulting in a decrease in the containment atmosphere temperature analogous to the measurement of the wet-bulb temperature. The rate of evaporation of the spray is controlled by the mass transport phenomena between the spray droplets and the atmosphere. The mass transfer rate from a drop may be calculated by the following formula[2]:

$$W_{dr} = k\pi D^2 \frac{X_{dr} - X_{atm}}{1 - X_{dr}} \ . \tag{1}$$

(See the Nomenclature on p. 45 for a definition of symbols.) The heat transfer associated with the evaporating drop is the sum of the sensible heat contribution from the temperature difference and the latent heat supplied by the mass transfer process.

The mass and heat transfer rates are dependent on many variables, such as the mass diffusivity, the drop size distribution and corresponding drop velocity distribution, the transient atmospheric vapor pressure and temperature, etc. As such, the transfer rates are transient and require a detailed analysis for evaluation. Therefore, it has been conservatively assumed that the spray entering the containment instantaneously vaporizes, resulting in the theoretical maximum heat and mass transfer rates.

The assumption of instantaneous spray evaporation has been incorporated into CONTEMPT-LT by introducing the spray mass/energy directly into the containment atmosphere as water vapor. Thus, no

liquid water is present until the atmosphere becomes saturated. For plants incorporating vacuum relief systems such as vacuum breakers, this assumption is overly conservative, since spray drop evaporation times on the order of 20 s are typical. Incorporation of spray mass transport considerations would reduce the depressurization rate and allow the vacuum relief devices time to operate. The maximum short-term depressurization value for plants without vacuum relief devices, however, will not be significantly changed by incorporation of a realistic evaporation model.

More water is evaporated from the sprays into the atmosphere for lower initial relative humidities. The resulting decrease in the air energy due to the latent heat supplied during the evaporation process causes a decrease in the atmospheric temperature and, hence, the pressure. Therefore, the depressurization of the containment is greater for lower initial relative humidities. This short-term depressurization can be estimated by iterating on the energy and volume constraints for saturated conditions. The general energy conservation equation is

$$M_a(U_{a0} - U_{af}) + M_g(U_{g0} - U_{gf})$$

$$+ \int_0^{t_f} \dot{M}_{sp}[U_g(t) - U_{gf}]dt$$

$$= \int_0^{t_f} \dot{M}_{sp}[U_g(t) - U_{sp}]dt \ . \tag{2}$$

By assuming a linear change in internal energy properties, a constant latent heat contribution, and a constant spray rate, the energy equation can be simplified as shown below along with the volume constraint:

$$\left[M_a C_{va} + \left(M_g + \frac{\dot{M}_{sp} t_f}{2} \right) C_{vg} \right] (T_0 - T_f)$$

$$= \dot{M}_{sp} t_f \left[U_g \left(\frac{T_0 + T_f}{2} \right) - U_{sp} \right] , \qquad (3)$$

$$v_g(T_f)(M_g + \dot{M}_{sp} t_f) = V . \qquad (4)$$

Iteration of the time and temperature for saturation of the containment will result in convergence on the resulting conditions for the short-term phase. Once the temperature is known, the depressurization can be calculated by applying the perfect gas law and the steam tables, or

$$P_d = P_0(T_0) - \left[P_a(T_0) \frac{T_f}{T_0} + P_g(T_f) \right] , \qquad (5)$$

where P_0 and P_a are evaluated at the initial atmospheric temperature, T_0, and P_g is evaluated at the final atmospheric temperature for the short-term transient, T_f.

The depressurization values predicted by CONTEMPT-LT are shown in Fig. 2, which presents the maximum short-term depressurization as a function of initial relative humidity. The depressurization is greater for lower initial relative humidities and/or higher initial containment temperatures. The results from the simple calculational model presented by Eqs. (2) through (5) are within 0.001 kg/cm² (0.01 psi) of the CONTEMPT-LT values.

The effect of varying the spray temperature has also been evaluated for the short term; the temperature was varied from 4 to 49°C (40 to 120°F) with 0% initial relative humidity. The spray temperature has a small effect on the short-term depressurization as the change of 45°C (80°F) in the spray temperature makes a difference of ~0.004 kg/cm² (0.05 psi). In addition, heat sink effects were studied; the analytical techniques are presented in more detail in Sec. III. As would be expected, the perturbation is small due to the time frame involved. For example, for a 0% initial relative humidity and a spray temperature of 27°C (80°F), inclusion of heat sinks makes less than a 0.001 kg/cm² (0.01 psi) difference in the depressurization value.

An apparent anomaly from the analysis is that for low initial relative humidities, the containment atmosphere may fall below the initial spray temperature. This situation can be explained by the fact that the spray temperature only determines the initial energy of the water and has a small effect on the latent heat supplied by the air for evaporation. In addition, the

temperature of the drop will decrease to the temperature of adiabatic saturation,[3] or the wet-bulb temperature. Since the evaporation process is controlled by vapor pressure differences from Eq. (1), water will continue to be evaporated from the drop to the atmosphere until the atmosphere becomes saturated. Therefore, the containment atmosphere may fall below the initial spray water temperature during this evaporation process.

III. LONG-TERM PHASE

After the atmosphere becomes saturated due to the mass transfer from the spray water drops, the containment response is controlled by heat transfer among the sprays, containment atmosphere, and heat sinks. A theoretical maximum depressurization can be derived by neglecting the heat sinks and assuming that the containment atmosphere ultimately reaches the initial spray temperature. Thus, the partial pressure of the air will simply change by a ratio of absolute temperatures, while the vapor pressure will be equal to the saturation value at the initial spray temperature. The theoretical maximum long-term depressurization is equal to

$$P_d = P_0(T_0) - \left[P_a(T_0) \frac{T_{sp}}{T_0} + P_g(T_{sp}) \right] , \qquad (6)$$

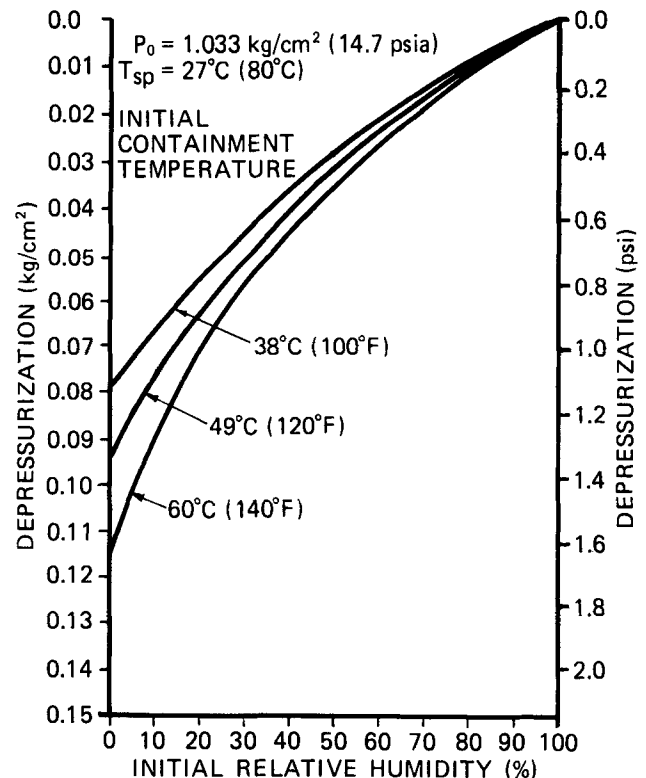which is similar to Eq. (5) presented in Sec. II.

Fig. 2.   Maximum short-term depressurization.

In the long-term phase, heat transfer between the spray drops and the atmosphere may or may not depressurize the containment more than achieved during the short-term phase. If the spray inlet temperature is greater than the short-term temperature of the containment atmosphere, the containment temperature will be increased by the sprays, resulting in an increase in the pressure. Conversely, if the spray inlet temperature is less than the short-term temperature, the containment temperature will be decreased by the sprays, resulting in further depressurization. Therefore, either phase may result in the maximum depressurization. The heat transfer rate between the spray drops and the containment atmosphere is a function of the drop size, velocity, and temperature. The spray drops will attain thermal equilibrium with the containment atmosphere within a few seconds.[4,5] Therefore, the conservative assumption has been made in CONTEMPT-LT that the spray water reaches the containment temperature instantaneously, maximizing the heat transfer rate and the resulting depressurization value.

Heat transfer between the containment structures and the containment atmosphere will result in a less severe long-term depressurization transient, since the structures act as heat sources in this case. The containment structures and atmosphere reach about the same temperature during normal operation within a reasonably short period of time. Therefore, when the containment temperature and pressure decrease as a result of the sprays, the temperature of the structures is higher than the atmosphere and heat is added to the containment atmosphere during the transient.

A turbulent natural convection heat transfer correlation for vertical plates and cylinders has been used in CONTEMPT-LT for the heat transfer coefficient between the heat sinks and the containment atmosphere. This correlation will result in a conservatively low estimate of the heat transferred from the containment structures to the containment atmosphere and can be approximated by the relationship[6]

$$h_c = 1.3 \, \Delta T^{1/3} \qquad (7a)$$

in SI units or

$$h_c = 0.19 \, \Delta T^{1/3} \qquad (7b)$$

in English units. The above heat transfer correlation has been combined with the containment structures designated as heat sinks for the containment integrity analysis from a pipe rupture.

Figure 3 presents the maximum long-term depressurization calculated by CONTEMPT-LT; this depressurization is greater for higher initial relative humidities and/or containment temperatures. Operator action 10 min after receipt of the appropriate negative pressure signal was assumed. A comparison to results obtained by Eq. (6) is presented in the next section.
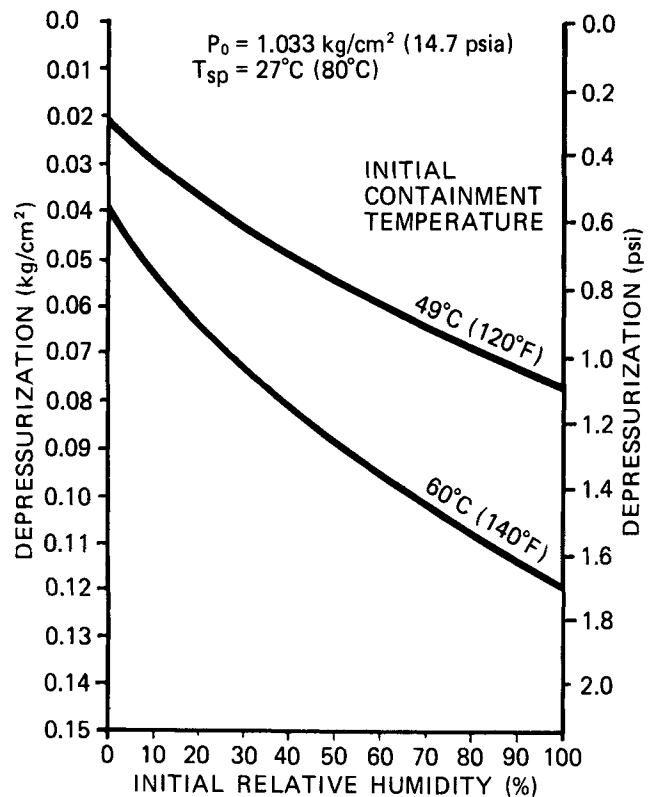
Fig. 3.   Maximum long-term depressurization.

IV. OVERALL EFFECTS

Figure 4 presents the maximum short-term and long-term depressurization for varying initial relative humidities. The short-term value dominates for lower relative humidities, while the longer term value controls for higher relative humidities. No single worst condition can be identified; the minimum and maximum relative humidities must be investigated to determine the maximum depressurization condition. The short-term depressurization can be calculated from the simple calculational model presented by Eqs. (2) through (5); however, as depicted in Fig. 4, the long-term pressurization may be considerably overestimated by the simple model of Eq. (6). The figure indicates a maximum depressurization of 0.146 kg/cm² (2.08 psi) using the simple model compared with 0.0773 kg/cm² (1.10 psi) for the CONTEMPT-LT transient model with heat sinks and operator action. Thus, the simple model overestimates the maximum depressurization by ~90%. The overall value, however, is overestimated by ~50% as the short-term depressurization becomes the limiting case.

V. CONCLUSION

The depressurization of the containment following inadvertent operation of containment sprays
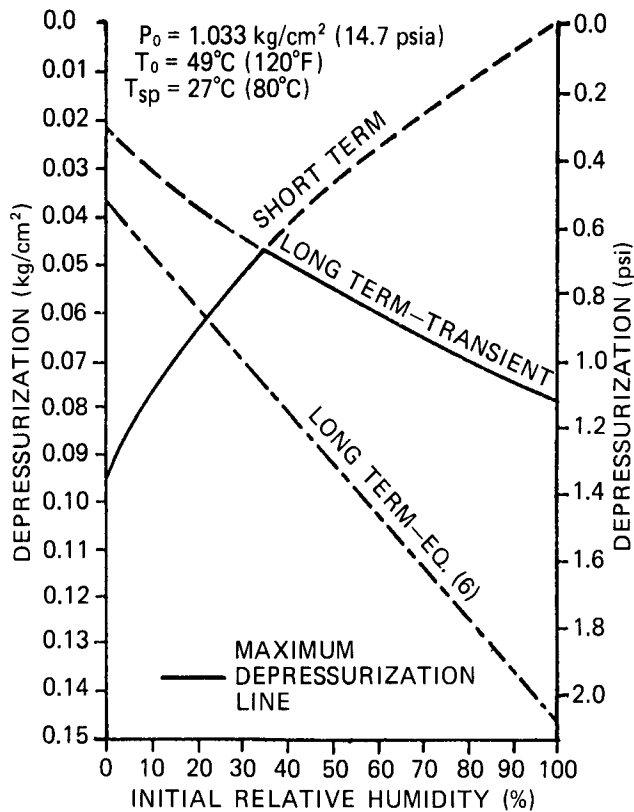
Fig. 4.   Maximum overall depressurization.

t = time

T = temperature

ΔT = temperature difference

U = specific internal energy

v = specific volume

V = containment volume

W = mass transfer rate

X = vapor pressure

Subscripts

a = air

atm = atmosphere

c = convection

d = depressurization

dr = drop

f = final

g = water vapor

0 = initial

sp = spray

v = refers to constant volume process

has two definite phases. The short-term phase due to evaporative cooling is dominated by the initial relative humidity and temperature; spray temperature and heat sinks are second-order effects. For the long term, heat transfer among the atmosphere, spray water, and containment structures and operator action are important and should be included as necessary. The short-term depressurization may be estimated by a simple calculational model; however, the long-term depressurization must rely on a transient analysis to avoid unnecessary conservatism. Analysis of the entire initial relative humidity range is necessary to determine the limiting case.

NOMENCLATURE

C = specific heat

D = drop diameter

k = mass transfer coefficient

h = heat transfer coefficient

M = mass

P = pressure

REFERENCES

1. L. L. WHEAT et al., "CONTEMPT-LT–A Computer Program for Predicting Containment Pressure-Temperature Response to a Loss-of-Coolant Accident," ANCR-1219, Aerojet Nuclear Company (June 1975).

2. R. B. BIRD, W. E. STEWARD, and E. N. LIGHTFOOT, *Transport Phenomena*, John Wiley and Sons, Inc., New York (1960).

3. W. E. RANZ and W. R. MARSHALL, Jr., "Evaporation from Drops," Parts I and II, *Chem. Eng. Prog.*, **48**, *141*, 173 (Mar.-Apr. 1952).

4. L. F. PARSLEY, "Design Considerations of Reactor Containment Spray Systems–Part VI. The Heating of Spray Drops in Air-Steam Atmospheres," ORNL-TM-2412, Part VI, Oak Ridge National Laboratory (Jan. 1970).

5. J. N. CHUNG and P. S. AYYASWAMY, "The Effect of Internal Circulation on the Heat Transfer of a Nuclear Reactor Containment Spray Droplet," *Nucl. Technol.*, **35**, 603 (1977).

6. W. H. McADAMS, *Heat Transmission*, 3rd ed., McGraw-Hill Book Company, Inc., New York (1954).

OPTIMUM FUEL LOADING AND OPERATION PLANNING FOR LIGHT WATER REACTOR POWER STATIONS. PART I: PRESSURIZED WATER REACTOR CASE STUDY

TSUTOMU HOSHINO *Institute of Atomic Energy, Kyoto University*
Gokanosho, Uji, Kyoto, Japan

A planning tool for strategic operation of nuclear power plants has been presented with a wider view on the overall utility system management. The tool was flexible enough to be capable of checking the feasibility of the proposed alternative plans as well as optimizing the plans in terms of the minimization of system operating costs over several refueling cycles.

The problem was defined in a small-scale utility system that consisted of a nuclear power plant and a replacement power station. The optimum decision was made on an in-core refueling pattern, its associated number of fuel assemblies, and the time length of coastdown operation. The optimization was subject to several physical and engineering constraints on reactor operation. Following the general decomposition approach, the method utilized iterative linear programming and a gradient projection algorithm of nonlinear programming.

A typical pressurized water reactor was studied. The economic gain was obtained mainly by filling margins originally involved in the reactivity and burnup limitations as well as by optimum coastdown operations. The flexibility of the method was especially enhanced in a case of recovery planning after unexpected plant outages with subsequent forced power reductions.

I. INTRODUCTION

A planning tool for operational strategy of nuclear power plants is needed that is versatile and flexible enough in actual circumstances. The planning task aims primarily at the search for several feasible alternatives, and, if these exist, the pursuit of the optimum solution comes next. The needs for the planning tool would be such that the tool must help the planner study, through simulation, several preselected alternative strategies, and that the feasibility as well as the optimization of the alternatives are automatically tested and performed by the planning tool.

For instance, as pointed out by Bonk et al.,[1] unexpected plant outage and consequent expenditure can easily cancel out the economic gain obtained by in-core fuel management. Actually, in-core fuel management is not restricted to "in-core" at all, but is subject to perturbations in the system environment around the nuclear power plant. Even in the age of base-loaded operation, there would be considerable economic incentive in the simultaneous planning of the cycle scheduling and in-core refueling scheme, before going too far into the details of reactor physics.

Early works on optimization of in-core refueling schemes mainly dealt with the near-equilibrium situation under fixed power and cycle length, with the dynamic programming technique.[2,3] Linear programming (LP) was found to provide a more powerful and flexible means for finding the optimal strategy for region-wise shuffling in nonequilibrium refuelings.[4-7] Integer LP was applied for the optimization of assembly-wise allocation of fuel assemblies.[8] Various formulations and methods other than these techniques have been presented for the in-core fuel management problem. Since the readers may find a proper review elsewhere,[9] the following brief comments are limited to the aspect of interaction between the refueling scheme and cycle-power scheduling.

Short-range economics of the cycle planning with a possibility of power stretchout was studied.[10] Several in-core management studies with the interaction to the cycle power demand and cycle period requirement were presented at an earlier topical

meeting.[11] The overall optimization of the fuel management, cycle scheduling, and power allocation among several nuclear plants was studied.[12,13]

A summary of the utility system planning was presented at a symposium[14] in 1974. Among the contributions to the symposium, a system integration model called ORSIM is one presenting the midrange planning of nuclear plant operation in the power network with many fossil and hydro power stations.[15,16] However, the interest of the work centered mainly on the aspect of the power system economization and the reliability assessment, while the optimum strategies around nuclear power stations are left unexplored.

One of these problems is the economic trade-off between the nuclear saving by stretchout operation and the expenditure for the replacement power, which may interest the operation planners. Stretchout is defined here as a plant operation such that the reactor continues to run after it loses the excess reactivity to be appropriated for the fuel depletion. It is possible for contemporary light water reactors (LWRs) to stretch out the operation in several ways, where the negative moderator reactivity-feedback is utilized for compensating the fuel depletion. Generally, as the coastdown interval increases, the nuclear fuel cost and system operating cost decrease on account of the increased nuclear fuel burnup. However, too much coastdown requires too much replacement power cost, which cancels out the nuclear fuel saving and results in the higher system operating cost. Economic trade-off between these two has been discussed in Refs. 17 and 18, where it must be noted that the optimum trade-off cannot be determined within a particular cycle, because potential interstage couplings exist among refueling cycles.

Another problem, more up-to-date, is how to adapt the once-established refueling scheme to month-to-month, year-to-year variations in system environment. A probable situation may be such that the fuel purchase has been made with slightly higher enrichments for the operation in a higher availability, while unexpected delays or outages will force the plant to operate in a lower availability. The only measure left to us is the optimization of refueling and power operational schemes.

To provide a flexible planning tool for these problems, the present paper[a] aims at the feasibility checking of operational strategies and the economic optimization in a well-defined, small-scale power system, as shown in Fig. 1, which consists of a nuclear power plant, a replacement power station to be integrated when the nuclear plant derates or shuts
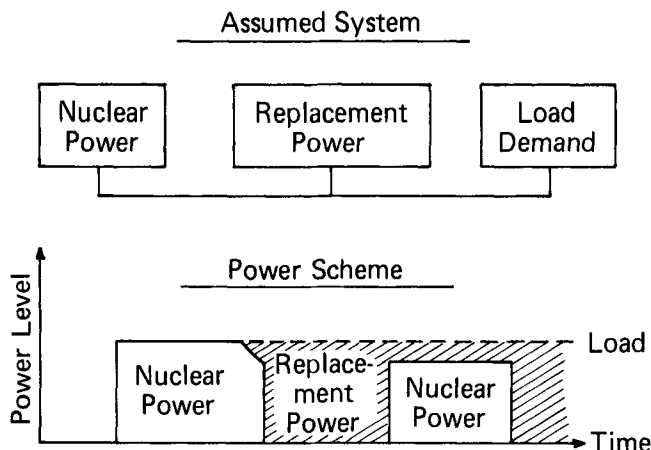
Fig. 1. Assumed system and power scheme.

down, and a load representing the system power demand.

In the present paper, the method follows the general guideline of earlier studies,[12,19] but with a more systematic way of optimization, that is, the decomposition of the problem into two phases: (a) in-core fuel management optimization under the fixed cycle and power scheduling, and (b) the search for better scheduling with the use of the dual variable or shadow cost information of the active constraints derived in phase a.

The objective function to be minimized is the system operating cost, including both nuclear and replacement fuel costs. The in-core part of the problem adopts the iterative LP formulation, modified from one proposed by Sauar,[5] with the additional constraints of safety and engineering considerations. The LP formulation makes it possible to check the feasibility of the problem, which must be ensured before the optimization task. The search for better cycle schedulings is guided by the gradient projection algorithm,[20,21] and the whole procedure is iterated until satisfactory convergence.

Note that the emphasis lies on the proposition and formulation of the problem defined in a simplified power system and the application of the mathematical programming techniques to this type of problem. Several simplifications and assumptions are involved in the fuel cost and reactor physics model. Assembly-wise expansion of the optimized solutions is also left to the users. A more elaborate formulation of the fuel cycle on making up the system operating cost can be incorporated with the present model without great modifications, although it is not intended in this paper.

A numerical example for a typical pressurized water reactor (PWR) is presented. The demonstrated figures, however, should be interpreted within the framework of input data and a simplified system model.

---

[a]This is an extension of an earlier presentation[7] that dealt with boiling water reactor (BWR) planning problems. BWR cases will be reported in Part II of this paper.

II. PROBLEM FORMULATION

II.A. Decision Variables

II.A.1. Lot Size

The in-core model is formulated in terms of "lot" and "lot size."[5] Lot, or batch, refers to a group of fuel assemblies that has a uniform nuclear property, and that is loaded, located in the same region, and discharged simultaneously. Lot is characterized in terms of lot pattern, i.e., region-location pattern defined by $LOC(i,j)$ = the region in which lot i is located in cycle j, where $LOC(i,j) = 0$ denotes out-of-core (see Fig. 2). Lot patterns can be either specified or generated automatically as all possible combinations of region-location history. Lot size N_i is the number of fuel assemblies belonging to lot i. Enrichment of particular lot is a fixed parameter, although several types of lots with different enrichments can be treated.

II.A.2. Cycle Periods and Cycle Power Level

The optimum decision is made at the beginning of the planning horizon, which is called the decision point. The planning horizon consists of J refueling cycles, although the lot patterns can extend beyond the planning horizon.

One refueling cycle consists of a fixed period of refueling shutdown, T_{sj}, a period of constant power operation, T_{fj}, with normalized power level, P_{fj}, and a subsequent period of coastdown operation, T_{dj}. Index j stands for the j'th cycle, where $j = 1, 2, \ldots, J$. The power level at the end of cycle (EOC) is given by

$$P_j^{EOC} = P_{fj} \exp(-r_d T_{dj}) \ , \tag{1}$$

where r_d denotes time rate of the power coastdown. The power level scheme is illustrated in Fig. 3. The decision variables in the optimization are taken as lot size $N = \text{col.}(N_i)$, where $i = 1, 2, \ldots, I$; power level $P_f = \text{col.}(P_{fj})$; cycle periods $T_f = \text{col.}(T_{fj})$; and $T_d = \text{col.}(T_{dj})$, where $j = 1, 2, \ldots, J$.

II.B. Objective Cost Function

The cost to be minimized is the levelized system operating cost discounted to the time origin, i.e.,

$$Z = \left[\sum_{i=1}^{I} C_i N_i + \sum_{j=1}^{J} A_j (D_j - P_r L_j) T_j \right] \Bigg/ \sum_{j=1}^{J} G_j D_j T_j \ , \tag{2}$$

where

C_i = discounted cost of a nuclear fuel assembly associated with lot i

N_i = lot size of lot i
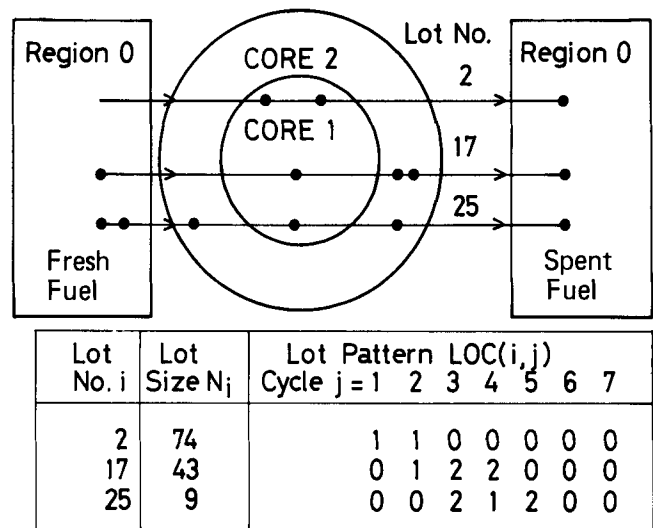
Fig. 2.   Illustrated lot pattern and lot size.

Lot No. i	Lot Size N_i	Lot Pattern LOC(i,j) Cycle j = 1	2	3	4	5	6	7
2	74	1	1	0	0	0	0	0
17	43	0	1	2	2	0	0	0
25	9	0	0	2	1	2	0	0

A_j = discounted cost of the fuel generating unit replacement power in cycle j

D_j = total demand power in cycle j

P_r = rating power of the nuclear plant

L_j = capacity factor of the nuclear plant

T_j = time length of cycle j

G_j = discounted value of unit electric power in cycle j.

The discounted costs are made up as follows:

$$C_i = RC_{0i}(1 + r_{nucl}/1 + r_{int})^{\tau_i} \tag{3}$$

$$A_j = A_0(1 + r_{repl}/1 + r_{int})^{t_j} \tag{4}$$

$$G_j = (1 + r_{elect}/1 + r_{int})^{t_j} \tag{5}$$

$$t_j = \sum_{j'=0}^{j-1} T_{j'} \ , \tag{6}$$

where

C_{0i} = cost of a fresh nuclear fuel assembly associated with lot i if purchased at the time origin

τ_i = time length between the time origin and the beginning of cycle (BOC) of the initial loading of lot i

A_0 = cost of the fuel for replacement power if purchased at the time origin

$r_{nucl}, r_{repl}, r_{elect}$ = escalation rates of the nuclear fuel, replacement fuel, and value of the electric power, respectively

r_{int} = interest rate

T_0 = time length between the time origin and BOC of the first cycle

R = discount factor for the fuels that remain in the core at the end of the planning horizon, where $0 \leqq R < 1$. $R = 1$ for the fuels discharged in the planning horizon.

Nuclear or replacement fuels are assumed to be purchased at each BOC. The value of discharged nuclear fuel should properly be included in the initial cost, C_{0i}. This is possible because once lot i and its lot pattern are specified, the discharge date, the discharged burnup, and the spent fuel salvage value can be determined. The initial cost, C_{0i}, works as an interface to the fuel cycle stream. Operating cost is made up of the expenditures for fuels and is independent of the factors that are not affected by the decision variables. The evaluation of the inventory that remains at the end of the planning horizon is adequately made with the discount factor R.

II.C. Constraints in Fuel Management

II.C.1. Constraint for Fuel Assembly Number

The number of fuel assemblies must be fixed based on the consideration of the thermal energy output. The number of fuel assemblies is kept constant in each region throughout the plant life:

$$C1: \sum_{i=1}^{I} \text{LOCT}(i,j,l)N_i = M_l \ , \quad \text{for all } j \text{ and } l \ , \qquad (7)$$

where

M_l = number of fuel assemblies in region l

$\text{LOCT}(i,j,l) = 1$, when $\text{LOC}(i,j) = l$

$= 0$, when $\text{LOC}(i,j) \neq l$.

II.C.2. Constraint for Minimum Core-Averaged k_∞ at EOC

To keep the core critical, the core-averaged multiplication factor at each EOC should not be less than the minimum permissible value:

$$C2: \sum_{i=1}^{I} K_\infty(i,j,\text{EOC}) \, \text{LOCM}(i,j)S_{ij}N_i/M_t$$

$$\geqq K_{\text{av}}(j,\text{min}) \ , \quad \text{for all } j \ , \qquad (8)$$

where

$K_\infty(i,j,\text{EOC}) = k_\infty$ of the fuel assembly of lot i at EOC of cycle j, which is defined in Sec. II.E

$\text{LOCM}(i,j) = 1$, when $\text{LOC}(i,j) \neq 0$

$= 0$, when $\text{LOC}(i,j) = 0$

S_{ij} = normalized power sharing by lot i in cycle j, which is defined in Sec. II.E

M_t = total number of fuel assemblies loaded in core

$K_{\text{av}}(j,\text{min})$ = minimum k_∞ of fuel assemblies averaged in core at EOC of cycle j to be compensated for by the neutron leakage, absorptions by xenon, samarium, residual boron, and burnable poisons. Stretchout operation with a lower core-averaged temperature reduces $K_{\text{av}}(j,\text{min})$ by $\Delta k_c(T_d)$, which is defined in Eq. (28).

II.C.3. Constraint on Burnup of Fuel

The burnup of the discharged fuel assembly is limited within the permissible maximum value U^{max}, based on those technical considerations of the irradiation-induced swelling and fission gas pressure buildup. The fuel purchase, guarantee, and reprocessing contracts would impose the constraints not only of this maximum burnup of single fuel assembly, but also of the maximum burnup averaged over discharged fuel assemblies at each cycle end, V^{max}:

$$C3: \sum_{j=1}^{J} \text{LOCM}(i,j)S_{ij}S_pL_jT_j \leq U^{\text{max}}, \quad \text{for all } i \ , \qquad (9)$$

$$C4: \sum_{i \in I_j} \text{LOCM}(i,j)S_{ij}S_pL_jT_jN_i/N_{dj} \leq V^{\text{max}} \ ,$$

$$\text{for all } j \ , \qquad (10)$$

where

I_j = set of indices of the lot discharged in cycle j

N_{dj} = total number of fuel assemblies discharged at EOC of cycle j

S_p = core-averaged specific power.

The latter constraint, C4, is treated explicitly in the LP calculation, while constraint C3 works implicitly on N_i, so that,

$C3': N_i = 0$ for those i's of which lot patterns violate constraint C3.

In case L_j and T_j are treated as fixed parameters, constraint C3 determines a subset of eligible lot indices, $I_e = (i; \text{C3 is satisfied})$, out of all possible lot indices $I_a = (i; i = 1, 2, \ldots, I)$. The summation $\sum_{i=1}^{I}$ appearing in this paper can be replaced by $\sum_{i \in I_e}$.

II.C.4. Constraint on the Available Partially Irradiated Fuel

In the case of the simulation of the recovery transient after unexpected plant outages, the initial cycle could start with the partially irradiated fuel. However, a limited number of these fuel assemblies are available. The constraint associated with this situation is written as follows:

$$C5: \sum_{i \in I_p} N_i \leqq A_{vp} \ , \qquad \text{for all } p \ , \qquad (11)$$

where

I_p = set of lot indices pertinent to the p'th type of partially irradiated fuel

A_{vp} = number of available fuel assemblies belonging to the p'th type fuel.

II.C.5. Constraint of Positivity

Lot size N_i should be positive:

$$C6: N_i \geqq 0 \ , \qquad \text{for } i \in I_a \ , \qquad (12)$$

and integral in nature. However, they are allowed to vary continuously, and the adjustment to integer numbers is left to the users.

II.C.6. Other Inactive Constraints and Assumptions

There are several constraints that are not active nor necessary in PWR operation planning. Constraint for the maximum core-averaged k_∞ of fuel assemblies at BOC is one prohibiting those situations when the core becomes too reactive due to the wrong choice of fuel enrichment or less burnup of fuels caused by a lower plant availability. The constraint is expressed by a similar form to C2:

$$C2': \sum_{i=1}^{I} K_\infty(i,j,\text{BOC}) \text{LOCM}(i,j) S_{ij} N_i / M_t$$

$$\leqq K_{av}(j,\text{max}) \ , \qquad \text{for all } j \ , \qquad (8')$$

where

$K_\infty(i,j,\text{BOC})$ = k_∞ of lot i at BOC of cycle j, which is defined in Sec. II.E.

$K_{av}(j,\text{max})$ = maximum k_∞ of fuel assemblies averaged in core at BOC of cycle j, to be compensated by the maximum concentrations of boron and a burnable poison if any.

This constraint will not become active except in very abnormal situations, such as an ordinary refueling scheme in a low availability, which is described in Sec. IV.D.

Constraints for minimum regional k_∞ of fuel assemblies at EOC and for a maximum number of the reactive (fresh) fuel assemblies in each cycle are mainly pertinent to the BWR core. The former is concerned with the power distribution shaping. The latter is related to the suppression of excessive local k_∞ and power peaking, which, in a PWR core, would adequately be maneuvered by the chemical shim control and burnable poison management, if necessary.

The optimized refueling schemes are determined in terms of the type and number of fuel assemblies in each region in each cycle. Their expansion into assembly-wise allocation must be made elsewhere to check the feasibility of the optimized schemes with respect to the thermo-hydraulic margin and one-rod-stuck reactivity margin. The constraint for the maximum regional fresh loading may be helpful in making this assembly-wise expansion task feasible.

II.D. Constraints in Plant Operation

II.D.1. Constraint on Power Level

The power level normalized by rating power P_r should not exceed the maximum, P_j^{max}, and should not be lower than the minimum, P^{min}:

$$C7: P_{fj} \leqq P_j^{\text{max}} \ , \qquad \text{for all } j \ , \qquad (13)$$

$$C8: P_j^{\text{EOC}} \geqq P^{\text{min}} \ , \qquad \text{for all } j \ . \qquad (14)$$

Note that constraint C8 also limits the maximum length of T_{dj}.

II.D.2. Constraint on Cycle Length

The cycle length cannot be longer than the permissible period, T_j^{max}, between the inspections regulated by the authority:

$$C9: T_j \leqq T_j^{\text{max}} \ , \qquad \text{for all } j \ . \qquad (15)$$

A set of variables (P_f, T_f, T_d) or space represented by them characterizes the plant operation scheduling and is called TP variables or TP space.

II.E. Core Model

The normalized power sharing S_{ij} in constraints C2, C2', C3, and C4 is dependent, through the reactor physics model, on the fuel loading scheme characterized by lot pattern and lot size N_i. The power sharing of each fuel assembly, S_{ij}, is empirically correlated on k_∞ of each fuel assembly by the following relation[22]:

$$\tilde{S}_{ij} = \exp\left[A_m \frac{K_\infty(i,j,\text{BOC})}{K_{av}(j,\text{BOC})} + B_m\right] \ , \qquad m = \text{LOC}(i,j) \ , \qquad (16)$$

$$S_{ij} = F_j \tilde{S}_{ij} \ , \qquad (17)$$

$$F_j = M_t \bigg/ \sum_{i=1}^{I} \tilde{S}_{ij} N_i \text{LOCM}(i,j) \quad , \tag{18}$$

where

$$K_{av}(j,\text{BOC}) = \sum_{i=1}^{I} N_i K_\infty(i,j,\text{BOC})\text{LOCM}(i,j)/M_t \quad . \tag{19}$$

The exponential function is introduced to keep the positivity of the value as well as to obtain better fittings on the correlated data. Constants A_l and B_l are empirical parameters pertinent to region l.

Infinite multiplication factor K_∞ of the fuel assembly is expressed in terms of the fuel enrichment ϵ and the burnup B accumulated since the fresh fuel loading:

$$\left. \begin{aligned} k_\infty &= \alpha + \beta B + \gamma B^2 \\ \alpha &= \alpha_1 + \alpha_2\epsilon + \alpha_3\epsilon^2 \\ \beta &= \beta_1 + \beta_2\epsilon + \beta_3\epsilon^2 \\ \gamma &= \gamma_1 + \gamma_2\epsilon + \gamma_3\epsilon^2 \end{aligned} \right\} \quad . \tag{20}$$

Burnup of lot i at EOC of cycle j is expressed by

$$B = B_{ij} = \sum_{j'=1}^{j} \text{LOCM}(i,j')S_{ij'}S_p L_{j'}T_{j'} \quad . \tag{21}$$

Multiplication factor $K_\infty(i,j,\text{EOC})$ in Eq. (8) is calculated by the substitution of Eq. (21) into Eq. (20). Factor $K_\infty(i,j,\text{BOC})$ is derived from the substitution of burnup at BOC of cycle j. The multiplication factor k_∞ of fuel assemblies is defined in the reference state, i.e., in the rating temperature with no boron, no burnable poison, no xenon and samarium poisons, and no neutron leakage. These reactivity effects should be included in $K_{av}(j,\text{min})$ in constraint C2 and in $K_{av}(j,\text{max})$ in constraint C2'.

II.F. Stretchout Operation

Stretchout operation is to continue the operation after the reactor loses the excess reactivity to be appropriated for the depletion of fuel. The LWRs are generally capable of stretching out in several ways. The simplest is the coastdown operation, where the reactor is left alone and the power level gradually decays, while the reactivity depletion is compensated for by the excess reactivity newly introduced by the derated power through the negative power coefficient of the core. For PWRs, there are other options for coastdown operation, depending on the opening of the governing valve to the high-pressure turbine with or without the control by the T-average reference controller.[17] Another possibility is the feedwater-preheater cutout, where the preheater is deliberately

cut out and the core inlet coolant enthalpy decreases, thus bringing a similar effect on the reactivity balance.

Let us assume here a situation where only the coastdown with exponentially decaying power for T_{dj} days is intentionally planned, after the constant power generation in level P_{fj} has lasted for T_{fj} days, as shown in Fig. 3. The power level, P, during the coastdown is determined in such a way that the reactivity loss due to the fuel depletion, Δk_f, is always compensated for by the reactivity gain due to the power decrease, Δk_c, that is,

$$\Delta k_c(t) = \Delta k_f(t) \quad , \tag{22}$$

where t is the time measured from the beginning of the coastdown and power level P is normalized such that $P = 1.0$ at the rating power.

Noting that the fuel depletion rate is proportional to the power level P and that the additional reactivity introduced is proportional to the power decrease, we can write the equations

$$\frac{d\Delta k_f}{dt} = \left\langle \frac{\partial k_\infty}{\partial B}\frac{\partial B}{\partial t} \right\rangle = \left\langle \frac{\partial k_\infty}{\partial B}S \right\rangle P \tag{23}$$

and

$$\frac{d\Delta k_c}{dt} = \delta_p P_r \frac{dP}{dt} \quad , \tag{24}$$

where S is the assembly specific power, assumed to be independent of the power level, δ_p is the power coefficient of reactivity, and where $\langle \ \rangle$ means averaging procedure over the fuel assemblies in core.

Combining Eqs. (22), (23), and (24), we obtain the power level expression as follows:

$$P = \exp(-r_d t) \quad , \tag{25}$$

where

$$r_d = -\left\langle \frac{\partial k_\infty}{\partial B}S \right\rangle \bigg/ \delta_p P_r \quad . \tag{26}$$

Note that the EOC power level of Eq. (1) is based on the above expression.

The bracketed value in Eq. (23) can be further approximated by using Eq. (20), i.e., burnup B_{ij} at EOC, as follows:

$$\left\langle \frac{\partial k_\infty}{\partial B}S \right\rangle = \sum_{i=1}^{I} \left(\frac{\partial k_\infty}{\partial B}\right)_{ij} S_{ij}S_p \text{LOCM}(i,j)N_i/M_t$$

$$\cong \sum (\beta + 2\gamma B_{ij})S_{ij}S_p \text{LOCM}(i,j)N_i/M_t \quad . \tag{27}$$

Integrating Eq. (23) together with Eq. (25) during the coastdown, we obtain the additional reactivity introduced by the power coastdown, i.e.,
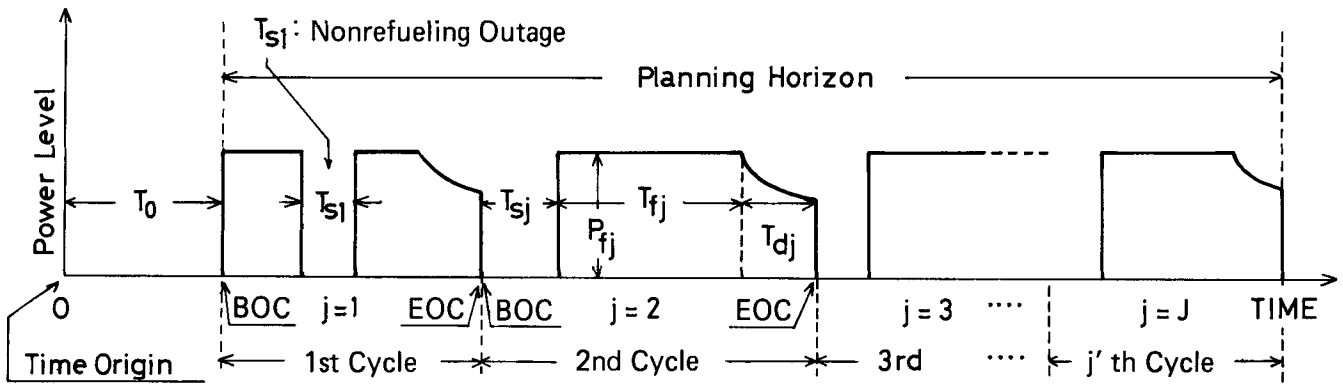
Fig. 3.   Assumed power level and time interval scheme. Here,

P_{fj} = constant power level

T_{fj} = constant power level period

T_{dj} = coastdown period

T_{sj} = refueling outage period.

Outage in cycle 1 is planned for inspection purpose.
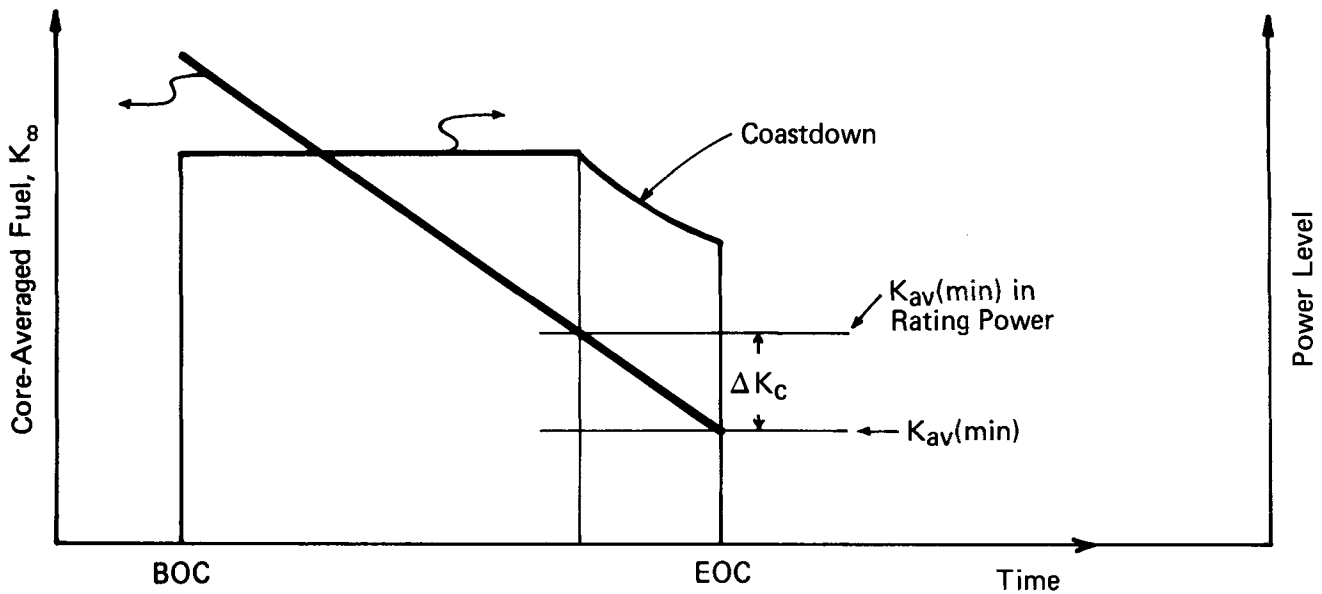
Fig. 4.   Power level and fuel k_∞ depletion.

$$\Delta k_f(T_d) = \Delta k_c(T_d) = \frac{S_p}{M_t r_d} [1 - \exp(-r_d T_{dj})]$$

$$\times \sum_{i=1}^{I} S_{ij}(\beta + 2\gamma B_{ij})\text{LOCM}(i,j)N_i \ . \qquad (28)$$

Since the k_∞ constraints in this study are imposed on the fuel k_∞ averaged over core, adequate treatment of the coastdown effect requires that the reactivity compensation, Δk_c, should be taken into account in the constraint vector, b, of Eq. (31) or (33), where the minimum k_∞ bound is interpreted as follows (see Fig. 4):

$$K_{av}(\text{min}) = [K_{av}(\text{min}) \text{ in rating power}] - \Delta k_c \ .$$
$$\qquad (29)$$

However, the term Δk_c is linear in terms of N_i as shown in Eq. (28), which will be taken into account in the constraint matrix A of Eq. (31) or (33), instead of being included in the constraint vector b.

II.G. Interrelation Among Variables

The cost function, Eq. (2), and constraints C3, C4, and C9 are expressed in terms of cycle length, T_j, and cycle capacity factor, L_j, which can be calculated from the TP variables as follows:

$$T_j = T_{sj} + T_{fj} + T_{dj}$$
$$L_j = P_{fj} \left\{ T_{fj} + [1 - \exp(-r_d T_{dj})/r_d] \right\} /T_j \Bigg\} \quad . \quad (30)$$

II.H. Problem Statement

Now the problem can clearly be stated as

P1: Overall Problem. Determine the decision variables, N, P_f, T_f, and T_d, so as to minimize the cost function, Eq. (2), subject to constraints C1 through C9.

III. METHOD OF SOLUTION

III.A. Nonlinearities

The cost function, Eq. (2), and constraints C1 through C9 are nonlinear in terms of the decision variables, N, P_f, T_f, and T_d. Nonlinearities exist in the cost function itself, in the dependence of k_∞ on the exposure E, and in the dependence of E on S_{ij}, P_f, T_f, and T_d. The power sharing, S_{ij}, is also determined by the fuel loading scheme, and the discharged assembly number, N_{dj}, of constraint C4 is a part of the fuel scheme itself, all of which constitutes the nonlinear feature of the problem.

III.B. Method of Solution

III.B.1. Decomposition of the Problem

One way, probably the only way, of making the problem tractable is the application of the decomposition principle with the careful aid of the iterative technique. By the extended application of Rosen's partitioning algorithm in nonlinear programming,[21] the problem is decomposed into an in-core refueling subproblem and an overall optimization of subproblem in the plant operation planning. A conceptual scheme of the method is depicted in Fig. 5.

III.B.2. Procedure

TP variables P_f, T_f, and T_d are fixed, at a moment, as TP parameters, and the in-core fuel management problem is solved with respect to the lot size N. The subproblem, called the fuel subproblem, is stated as follows:

P2: Fuel Subproblem. Given the TP parameters P_f, T_f, and T_d, determine the lot size, N, so as to minimize the nuclear fuel cost $Z_n = C \cdot N$, subject to constraints C1 through C6 represented by a matrix form,

$$A \cdot N = b \quad . \quad (31)$$

III.B.3. Fuel Subproblem

The problem is still nonlinear due to the dependence of the power sharing on the lot size. This part

TP Variables

FUEL SUBPROBLEM

Given TP Variables
Optimize In-Core
Fuel Scheme

OVERALL PROBLEM

Given Fuel Scheme
Optimize System
Operating Cost
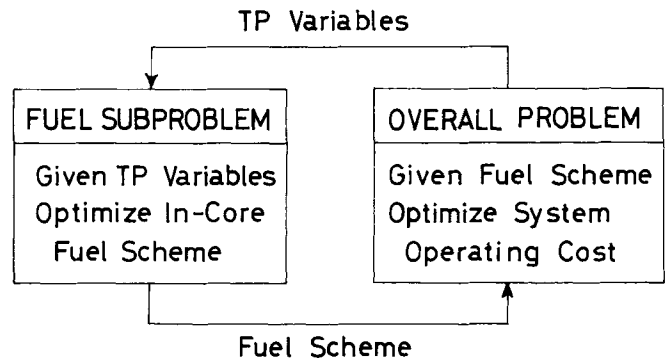
Fuel Scheme

Fig. 5. Conceptual scheme in solution: decomposition.

of the nonlinearities will be overcome by an iterative technique, such that the fuel subproblem is solved by assuming proper values for decision-variable-dependent parameters; then, solution N updates the assumed values. The procedure is called PS iteration, which can be summarized as follows:

1. Make guesses at $K_{av}(j, \text{BOC})$ in Eq. (16), F_j in Eq. (17), and N_{dj} in Eq. (10). Let them be denoted by

$$k_1 = \text{col.}[K_{av}(j, \text{BOC})]$$
$$F_1 = \text{col.}(F_j) \Bigg\} \quad , \quad (32)$$
$$N_{d1} = \text{col.}(N_{dj})$$

and let $g = 1$.

2. Solve the fuel subproblem for the g'th iteration:

P3: Minimize $Z_{ng} = C \cdot N$,

subject to $A(k_g, F_g, N_{dg}) \cdot N_g = b$.   (33)

3. If $|Z_{ng} - Z_{ng-1}|/Z_{ng} < e$, where e is an error criterion, then the iteration is supposed to converge.

4. Calculate new values for k_g^*, F_g^*, and N_{dg}^* from the solution N_g.

5. Determine the guesses for the next iteration by conventional relaxation formulas:

$$k_{g+1} = r_k k_g^* + (1 - r_k)k_g$$
$$F_{g+1} = r_f F_g^* + (1 - r_f)F_g \Bigg\} \quad , \quad (34)$$
$$N_{dg+1} = N_{dg}^*$$

and repeat from step 2 with $g \Leftarrow g + 1$.

Cost vector C and constraint matrix A in Eq. (33) are no longer dependent on the decision variable N, so that the minimization problem of step 2 can be solved by the use of LP. Infeasibility is automatically detected by the well-known two-stage simplex algorithm for LP (Ref. 20). Therefore, the PS iteration either converges with a sequence of feasible solutions or ends with infeasibility in an LP routine.

III.B.4. Overall Problem

The PS iteration with fixed TP parameters terminates with the minimum operating cost if the fuel subproblem is feasible; otherwise, fuel subproblem P2 is infeasible for the given set of TP parameters. Consequently, the overall problem, P1, is reduced to a minimization problem, P4, below.

P4: Minimize $Z(P_f, T_f, T_d)$, subject to constraints C7, C8, and C9 and to such a constraint that the sought variables must always be kept within the domain of feasibility of the fuel subproblem P2:

$$C10: \quad H(P_f, T_f, T_d) \leqq 0 \ . \tag{35}$$

The minimization problem, P4, can be solved by the gradient projection algorithm with the aid of the cost gradient information.

III.B.5. Cost Gradient Vector

The gradient vector,

$$-\nabla Z = -(\partial Z/\partial P_f, \partial Z/\partial T_f, \partial Z/\partial T_d) \ ,$$

indicates the steepest descent of cost function Z. The partial derivatives of Z in the j'th cycle subspace of TP space (P_f, T_f, T_d) are expressed as follows:

$$\frac{\partial Z}{\partial X_j} = \left[\frac{\partial (Z_n + Z_r)}{\partial X_j} P_t - \frac{\partial P_t}{\partial X_j} (Z_n + Z_r) \right] \bigg/ P_t^2 \ , \tag{36}$$

where the cost function Eq. (2) is rewritten by

$$Z = (Z_n + Z_r)/P_t \tag{2'}$$

where

Z_n = discounted nuclear fuel cost = $\sum_i C_i N_i$

Z_r = discounted replacement fuel cost

$$= \sum_j A_j (D_j - P_r L_j) T_j$$

P_t = discounted total electric power = $\sum_j G_j D_j T_j$.

Variable X_j represents any one of TP variables P_{fj}, T_{fj}, or T_{dj}.

The derivatives of the nuclear fuel cost are further approximated by the use of the dual solution, π, as well as the primal solution, N_0, of the fuel subproblem P3:

$$\frac{\partial Z_n}{\partial X_j} \cong \pi \left(\frac{\partial b}{\partial X_j} - \frac{\partial A^*}{\partial X_j} N_0 \right) \tag{37}$$

$$= \pi \frac{\partial b}{\partial X_j} - \pi \frac{\partial A^*}{\partial L_j} N_0 \frac{\partial L_j}{\partial X_j} - \pi \frac{\partial A^*}{\partial T_j} N_0 \frac{\partial T_j}{\partial X_j} \ , \tag{38}$$

where A^* is the matrix A of Eq. (31) or (33), excluding the coastdown effect $\Delta k_c(T_d)$ by Eq. (28).

III.B.6. Cost Minimization Procedure: TP Search

In the minimization guided by the cost gradient vector, special care must be taken to keep the point of search within the constraint domain prescribed by constraints C7, C8, and C9. In case the point comes on the boundary of the domain and the gradient vector $-\nabla Z$ directs outward, the projection of the vector of the boundary surface will indicate the best direction of decreasing Z. This type of search is well known as the gradient projection method,[21] with a stopping rule based on the fundamental theorem by Kuhn-Tucker (see Ref. 20).

Actually, as described below, the search procedure can be discussed only on the surface of $P_{fj} = P_j^{max}$ in each cycle j. It must be noted, however, that the constraint domain can be further trimmed by constraint C10. The procedure must be flexible enough to treat the infeasible fuel subproblem. Principles of the minimization procedure, TP search, are summarized as follows. (Also, refer to Fig. 6, which illustrates several probable situations that may occur in TP search.)

1. The current point of search in TP space is kept on the TP line determined by activated constraints C7 and C9, i.e.,

$$\text{TP line:} \quad P_{fj} = P_j^{max} \ , \qquad \text{for all } j \ , \tag{13'}$$

$$T_{fj} + T_{dj} = T_j^{max} - T_{sj} \ , \quad \text{for all } j \ . \tag{15'}$$

This is based on a fact that increasing the total power P_t is the most efficient means for decreasing the cost Z.

If the current point of search lies in the interior of the domain of constraints C7, C8, and C9, it is brought on the TP line along the direction of the steepest descent, $-\nabla Z$, in the next step of the search. (See steps $1 \rightarrow 2$, $1' \rightarrow 2'$, $1'' \rightarrow 2''$, and $7'' \rightarrow 8''$ in Fig. 6.)

2. On the TP line, the search continues in the direction of the orthogonal projection of the $-\nabla Z$ vector on the line, as far as the cost is improved. (See steps $2 \rightarrow 3$, $2' \rightarrow 3'$, $4' \rightarrow 5'$, and $8'' \rightarrow 9''$ in Fig. 6.)

3. If the cost is not improved, the step of search is reduced by half to ensure the local optimality of the point. (See steps $3 \rightarrow 4$ and $3 \rightarrow 5$ in Fig. 6.)

4. In case the current of search violates constraint C10, that is, the case of infeasible fuel subproblem, the step size is reduced by half to find the approximate boundary of feasible region. (See steps $1'' \rightarrow 2''$, $2'' \rightarrow 3''$, $4'' \rightarrow 5''$, and $5'' \rightarrow 6''$ in Fig. 6.) Thereupon, the search is guided to go round the infeasible region. (See steps $3'' \rightarrow 4''$ and $6'' \rightarrow 7''$ in Fig. 6.)

5. The stopping rule is based on the Kuhn-Tucker condition.[20] The search terminates when either one of the following cases occurs:
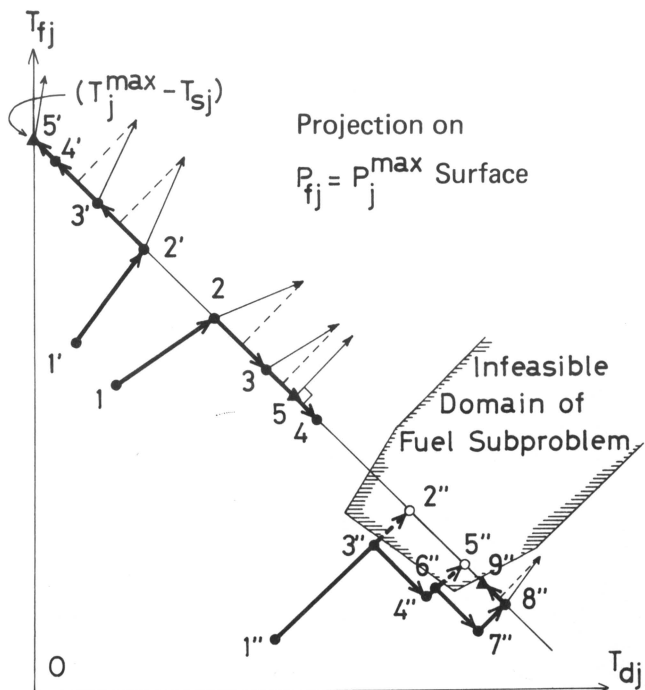
Fig. 6. Typical TP search procedures on (T_{fj}, T_{dj}) plane. Route of search is projected on $P_{fj} = P_j^{pmax}$ surface in cycle j subspace of TP space. Here, T_j^{max} is the maximum cycle length in cycle j and T_{sj} is the shutdown period in cycle j.

a. The cost gradient vector is perpendicular to the TP line. (See point 5 in Fig. 6.)

b. The search on TP line reaches the corner point, i.e.,

$$T_{dj} = 0 \ , \quad \text{or} \quad T_{dj} = (1/r_d)\ln(P_j^{max}/P^{min}) \ , \tag{39}$$

and the next move violates the constraint domain. (See points 5' and 9' in Fig. 6.)

III.C. Asymptotic Solution to Equilibrium Refueling

It is always a problem to evaluate the fuels that remain inside the core at the end of the planning horizon. One way of treating this problem is to assume the equilibrium refueling near the end of the horizon and to force the optimum solution being asymptotic to the equilibrium refueling. Let us define "equilibrium fuel lots" as those that are initial loaded within the planning horizon but are discharged

beyond the horizon. An example is given in Tables I and II for these equilibrium lots spanning beyond the planning horizon.

Given lot size N_2 and constraint matrix A_2 associated with the equilibrium fuel lots, we can rewrite the constraint equation of Eq. (31) as follows:

$$[A_1 \mid A_2]\begin{bmatrix} N_1 \\ \hline N_2 \end{bmatrix} = [b] \ . \tag{40}$$

The asymptotic component, N_1, is obtained by solving LP:

$$\text{Min.} \ Z = C_1 \cdot N_1 \ , \tag{41}$$

$$\text{subject to } A_1 \cdot N_1 = b - A_2 \cdot N_2 \ , \tag{42}$$

where C_1 is the cost vector associated with N_1. Note that the cost of these equilibrium lots, N_2, is taken care of by factor R in Eq. (3).

IV. NUMERICAL STUDY

IV.A. Reference Case and Optimized Cases

The procedure was programmed in a code, "FAPMAN" (Ref. 23). A typical PWR of 826 MW(electric) was studied. The case taken as a reference (Case I) is an out-in refueling scheme of one-third core batch size with a conventional scatter loading in the inner region. The initial core is loaded with the fuels of 2.0-, 2.7-, and 3.35-wt% enrichments. Then the core is brought to equilibrium with the feed fuel of 2.8-wt% enrichment. Other parameters used in the calculation are listed in Table III. Lot patterns and lot sizes associated with one-third core out-in scatter loading were specified by input data to the program.

The optimization was carried out (Case II) with respect to lot size, N, while the lot patterns are fixed in the same out-in refueling scheme as in Case I.

In Case III, not only the lot size but also the lot patterns were optimized within the framework of general out-in refueling scheme, where the fresh fuel assemblies are loaded only in the outermost core region, then shuffled inward, and finally discharged from the innermost core region. The cycle periods and power level, i.e., TP variables for Cases II and III, are the same as that of Case I, the capacity factor being 70%.

Optimization was then extended to the TP variables in Case IV, where the optimum coastdown operation is attempted. For these cases, the equilibrium out-in refueling scheme of the reference case is assumed beyond the planning horizon. The lot patterns in planning horizon must be asymptotic to this equilibrium cycle scheme. The inventory remaining in the core at the end of planning horizon is discounted by half, i.e., $R = 0.5$ in Eq. (3) when included in the fuel cost.

TABLE I

Reference Out-In Refueling Scheme

Cycle 1 2 3 4 5 6 7 8 9 10	Lot Size		Enrichment (wt%)
Lot Pattern	Case I[a]	Case II[a]	
1 0 0 0 0 0 0	52	52	2.0
1 1 0 0 0 0 0	1	24	2.0
1 1 0 0 0 0 0	50	27	2.7
1 1 1 0 0 0 0	1	1	2.7
1 1 0 1 0 0 0	1	1	2.7
2 1 1 0 0 0 0	52	52	3.35
0 2 1 1 0 0 0	51	51	2.8
0 2 1 1 1 0 0	1	1	2.8
0 0 2 1 1 0 0	51	51	2.8
0 0 2 1 1 1 0	1	1	2.8
0 0 0 2 1 1 0	51	51	2.8
0 0 0 2 1 1 1	1	1	2.8
0 0 0 0 2 1 1	51	51	2.8
(Beyond Horizon)			
0 0 0 0 2 1 1 1 0 0	1	1	2.8
0 0 0 0 0 2 1 1 0 0	51	51	2.8
0 0 0 0 0 2 1 1 1 0	1	1	2.8
0 0 0 0 0 0 2 1 1 0	51	51	2.8
0 0 0 0 0 0 2 1 1 1	1	1	2.8

[a]Noncoastdown operation with a 70% capacity factor.

Cases V, VI, VII, and VIII are similar to the cases I, II, III, and IV, respectively, but do not assume these equilibrium cycles beyond the planning horizon, where the residual in-core inventory is discharged and evaluated as zero,[b] i.e., $R = 0$. For all cases, the reloading of the once discharged fuel lots is permitted for the fuels of enrichment of 2.0 and 2.7 wt%.

IV.B. Cost Performances and Discussions

Cost performances are compared in Table IV for these cases. Detailed refueling schemes are listed in Tables I, II, and V. Time-dependent variations of core-averaged fuel k_∞ are depicted in Fig. 7 for Cases I and III. During the TP search in Case IV, a steep negative cost gradient toward increasing P_f keeps the search on $P_f = 1.0$ surface, i.e., in full-power operation.

It is noted that the optimization gain is obtained mainly by filling up the margins available that exist in burnup limit and reactivity residual in the reference

---

[b]The assumption of the zero-inventory value, $R = 0$, may not be natural, while another problem exists in the asymptotic assumption to the equilibrium: The assumed equilibrium refueling policy may not be optimum.

TABLE II

Optimum Out-In Refueling Scheme

(Asymptotic cases to equilibrium cycles beyond planning horizon)

Cycle 1 2 3 4 5 6 7 8 9 10	Lot Size[a]		Enrichment (wt%)
Lot Pattern	Case III[b]	Case IV[c]	
1 0 0 0 0 0 0	27	26	2.0
1 1 0 0 0 0 0	33	35	2.0
1 0 1 0 0 0 0	16	17	2.0
1 1 0 0 0 0 0	17	15	2.7
1 1 0 1 0 0 0	11	12	2.7
2 1 1 0 0 0 0	44	43	3.35
2 2 1 1 0 0 0	8	9	3.35
0 2 1 1 0 0 0	28	26	2.8
0 2 1 1 1 0 0	9	10	2.8
0 2 2 1 1 0 0	7	8	2.8
0 0 2 1 1 0 0	22	34	2.8
0 0 2 1 1 1 0	20	6	2.8
0 0 2 2 1 1 0	0	4	2.8
0 0 2 2 1 0 0	3	0	2.8
0 0 0 2 1 0 0	6	0	2.8
0 0 0 2 1 1 0	18	42	2.8
0 0 0 2 1 1 1	20	1	2.8
0 0 0 2 2 0 0	5	0	2.8
0 0 0 2 2 1 1	0	5	2.8
0 0 0 0 2 1 0	14	0	2.8
0 0 0 0 2 1 1	32	46	2.8
(Equilibrium Pattern)			
0 0 0 0 2 1 1 1 0 0	1	1	2.8
0 0 0 0 0 2 1 1 0 0	51	51	2.8
0 0 0 0 0 2 1 1 1 0	1	1	2.8
0 0 0 0 0 0 2 1 1 0	51	51	2.8
0 0 0 0 0 0 2 1 1 1	1	1	2.8

[a]Minor inconsistencies by ±1 may exist on the total number of fuel assemblies in a region; these can be attributable to the rounding-off to the integer values.
[b]Noncoastdown operation with 70% capacity factor.
[c]With optimum coastdown operation.

design parameters. As summarized in Table IV, the nuclear fuel cost of Case II is improved by 1.110% from the reference case because of the optimized lot size. The cost is further improved by 6.769% from the reference case due to the optimization of the lot pattern itself within the out-in refueling context.

The optimization gain in nuclear fuel cost depends on the enrichment of fuels in such a manner that the higher enrichment brings about the more optimization gain. Naturally, the optimization gain becomes zero if the enrichment of fuels is so adjusted that the reactivity margin at EOC is exactly zero.

TABLE III

Assumed Parameters in Numerical Study

Nuclear plant parameters
Thermal rating power	2432 MW
Electric rating power, P_r	826 MW
Number of fuel assemblies, M_l	
in inner region $l = 1$	105
in outer region $l = 2$	52
Core-averaged specific power	33.78 MW/tU
Minimum core-averaged k_∞, $K_{av}(j,\min)$	
in cycle $j = 1$	1.108
in cycles $j \geq 2$	1.098
Maximum core-averaged k_∞, $K_{av}(j,\max)$	
in cycle $j = 1$	1.31
in cycles $j \geq 2$	1.23
Rate of power coastdown, r_d	0.01486 1/day

Nuclear fuel parameters
Maximum fuel assembly burnup, U^{max}	36 500 MWd/tU
Maximum discharged burnup, V^{max}	33 000 MWd/tU

Fuel cycle and economic data
Feed assay	0.711 wt%
Tail assay	0.2 wt%
U_3O_8 cost	10 $/lb
Coversion cost	2 $/kg U_{feed}
Enrichment cost	40 $/kg U_{prod}·SWU
Fabrication cost	200 $/kg U_{prod}
Value of discharged fuel	None
Annual escalation rate of	
nuclear fuel cost, r_{nucl}	0.08
replacement fuel cost, r_{repl}	0.08
electric power value, r_{elect}	0.08
Annual interest rate	0.08

System parameters
Total system power demand, D	826 MW
Replacement fuel cost, A_0	23.3 mill/kWh
Fuel cycle length, T_j^{max}	
in cycle $j = 1$	592 days
in cycles $j \geq 2$	365 days
Shutdown period, T_{sj}	
in cycle $j = 1$	177.6 days
in cycles $j \geq 2$	109.5 days
Constant power period, T_{fj}	
in cycle $j = 1$	414.4 days
in cycles $j \geq 2$	255.5 days
Capacity factor	70%

TABLE IV

Specifications and Performance Figures of Numerical Examples

	Asymptotic Refueling to Equilibrium Pattern						Nonasymptotic Refueling			
	Reference	Optimized Cases			Recovery Cases		Reference	Optimized Cases		
	Case I	II	III	IV	XV	XVI	Case V	VI	VII	VIII
Lot size	Fixed	Optimized	Optimized	Optimized	Optimized	Optimized	Fixed	Optimized	Optimized	Optimized
Lot pattern	Fixed	Fixed	Optimized	Optimized	Optimized	Optimized	Fixed	Fixed	Optimized	Optimized
Coastdown	None	None	None	Optimized	None	Optimized	None	None	None	Optimized
System operating cost (mill/kWh)	8.701	8.682	8.586	8.580	10.39	10.38	8.918	8.900	8.766	8.758
System operating cost saving from reference case (%)	---	0.2170	1.324	1.393	---	---	---	0.2117	1.706	1.794
Nuclear fuel cost (mill/kWh)	2.430	2.403	2.266	2.252	1.399	1.383	2.741	2.714	2.523	2.505
Nuclear fuel cost saving from reference case (%)	---	1.110	6.769	7.333	---	---	---	0.9842	7.930	8.584
Nuclear capacity factor (%)	70.00	70.00	70.00	69.98	59.01	59.00	70.00	70.00	70.00	69.98
Discharged burnup[a] (MWd/tU)	24 643	24 643	26 203	26 425	26 265	26 469	22 021	22 021	23 646	23 795

[a] Averaged for all lots with unit discount factor.

However, the optimized nuclear fuel cost becomes smaller as the enrichment gets larger. That is because, though the fuel cost becomes higher in keeping with the enrichment under the fixed refueling pattern, the optimized fuel cost becomes lower due to a smaller batch size optimally adjusted, which consequently lessens the discharged reactivity potential. Some examples validating the statement are illustrated in Table VI.

During the TP search in Case IV, the cost improvement is also attributable to the nuclear fuel saving, as indicated by the reduction from 6.769 to 7.333%. However, the system operating cost saving by coastdown operation is not great due to the rapid

TABLE V

Optimum Out-In Refueling Scheme
(Nonasymptotic Cases)

Cycle	Lot Size[a]		Enrichment (wt%)
1 2 3 4 5 6 7			
Lot Pattern	Case VII[b]	Case VIII[c]	
1 0 0 0 0 0 0	27	26	2.0
1 1 0 0 0 0 0	33	35	2.0
1 0 1 0 0 0 0	16	17	2.0
1 1 0 0 0 0 0	17	15	2.7
1 1 0 1 0 0 0	11	12	2.7
2 1 1 0 0 0 0	44	43	3.35
2 2 1 1 0 0 0	8	9	3.35
0 2 1 1 0 0 0	28	26	2.8
0 2 1 1 1 0 0	9	10	2.8
0 2 2 1 1 0 0	7	8	2.8
0 0 2 1 1 0 0	31	30	2.8
0 0 2 1 1 1 0	10	11	2.8
0 0 2 2 1 1 0	3	4	2.8
0 0 0 2 1 1 0	34	32	2.8
0 0 0 2 1 1 1	10	11	2.8
0 0 0 2 2 1 1	5	5	2.8
0 0 0 0 2 1 1	43	42	2.8
0 0 0 0 2 2 1	5	5	2.8
0 0 0 0 0 2 1	43	42	2.8
0 0 0 0 0 2 2	4	5	2.8
0 0 0 0 0 0 2	48	47	2.8

[a]Minor inconsistencies by ±1 may exist on the total number of fuel assemblies in a region. These can be attributable to the rounding-off to the integer values.
[b]Noncoastdown operation with a 70% capacity factor.
[c]With optimum coastdown operation.

power decay in the stretchout operation in PWRs, which necessitates greater replacement power cost.

The way of filling up the margins observed in the process is such that the slack variables[c] associated with constraint C2 are driven out at all cycles. Constraint C4 relating to the burnup limit is always free in these numerical calculations, though the discharged burnup increases as the optimization proceeds, as shown in Table IV, which definitely contributes to the optimization gain as well. Constraint C10 limiting the cycle time length is strongly active. Given the maximum cycle length and the fixed refueling outage, the problem boils down to how to

---

[c]A slack variable is a variable, y, that converts inequality constraint $G(x) \leqq g$ or $G(x) \geqq g$ to equality constraint $G(x) + y = g$. It indicates the slackness or margin involved in the original constraint. The original constraint becomes active when $y = 0$.

share the operation into that with constant power level and coastdown. Also, this constraint essentially determines the maximum plant availability.

The optimum solution differs depending on the method of evaluating the fuel inventory remaining in the core at the end of the planning horizon. Generally speaking, the solutions forced to asymptote to the equilibrium cycle near the end of the horizon have less freedom to contribute to the optimization gain when they are compared to the nonasymptotic cases. For instance, optimized solutions for Cases III and IV shown in Table II do not attempt any fresh fuel loading in cycles 6 and 7, which lessens the effective fuel inventory subject to the optimization, while the optimization gain discussed is being compared to the reference case, which takes into account the whole fuel inventory loaded in the planning horizon.

On the contrary, in Cases VII and VIII in Table V, the remaining in-core inventory, including those fresh fuels loaded near the end, is supposed to be thrown away but is still subject to the optimization. It is noted that the economic savings for these cases are naturally greater than for the asymptotic cases. Ratio between savings can be approximately given by 5/6, the ratio between effective fuel inventories subject to the optimization.

As far as the initial and second cycle fuel loadings are concerned, the optimum nonasymptotic refueling schemes shown in Table V are almost the same as those of the asymptotic cases shown in Table II. The difference gets large in the cycles after the second, where the end effect starts to appear. That creates the impression, though it may not be generalized beyond the example illustrated here, that the propagation depth of the end effect may be nearly equal to the maximum refueling pattern length plus one cycle. It must also be noted for the cases in Table V that a set of lot patterns appear repeatedly after the first cycle with an accompanying rhythm in the lot size, which can be interpreted as the optimum equilibrium pattern. On the other hand, in the asymptotic cases in Table II, some repeated lot patterns are recognized with more vague rhythms in lot sizes.

Difference is also noticed in the optimum coastdown solutions shown in Table VII. Coastdown in cycles 5 and 6 of the nonasymptotic Case VIII is effective, by stretching out the fuel burnup, in reducing the wasteful fresh fuel loading near the end of the plant life, while in the asymptotic Case IV, the coastdown is avoided in these cycles, being forced to the assumed equilibrium scheme.

IV.C. Cost Sensitivity and Probable Errors

The PS iteration ends when the objective cost difference between consecutive iterations falls within the range prescribed by error criterion e. The oscillation in cost was observed during PS iteration, that is,
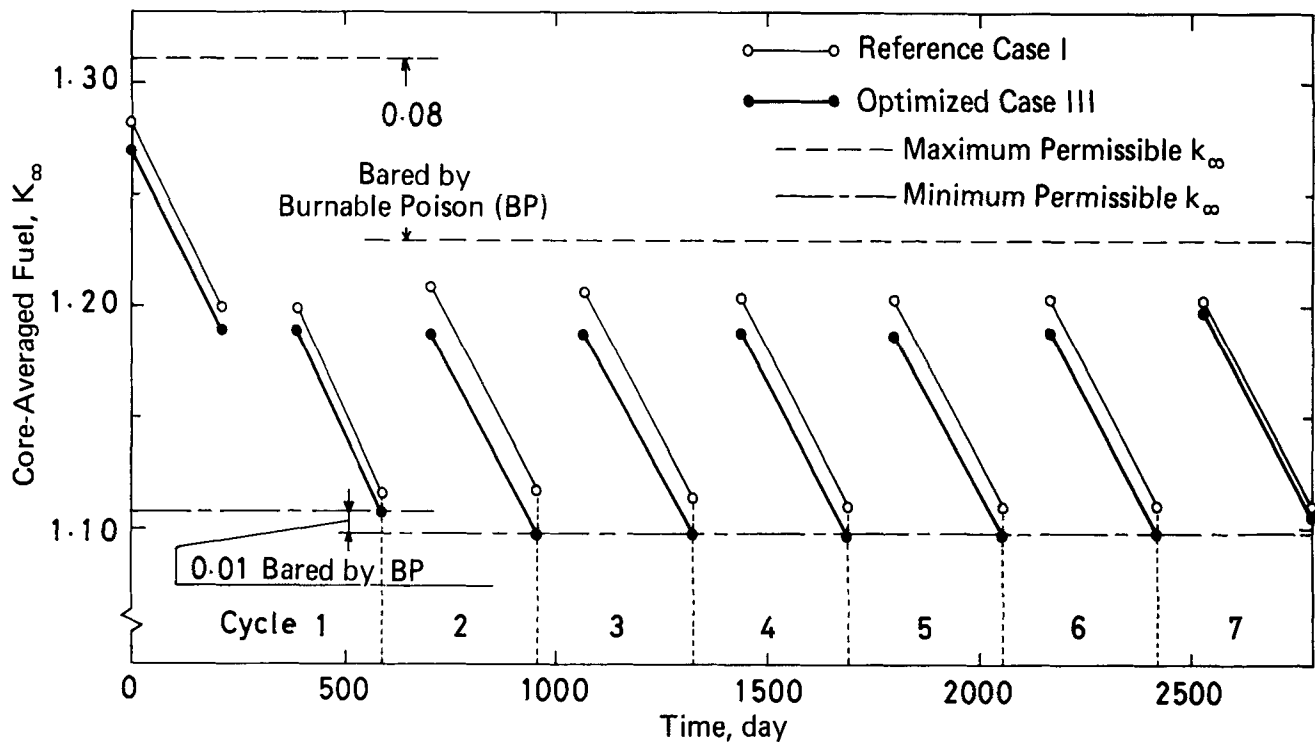
Fig. 7.   Core-averaged fuel k_∞ in reference Case I and optimized Case III.

TABLE VI

Nuclear Fuel Cost Saving Versus Feed Fuel Enrichment

Feed Fuel Enrichment[a] (wt%)	Nuclear Fuel Cost (mill/kWh)				Cost Saving from Each Reference Case (%)
	Reference Refueling[b]		Optimized Refueling[b]		
		Case Number		Case Number	
2.7	2.3560	IX	2.3058	X	2.132
2.9	2.4431	XI	2.2509	XII	7.869
3.1	2.5309	XIII	2.2086	XIV	12.735

[a]Feed fuels are loaded after cycle 1. Fuel enrichments for initial load are assumed as 2.0, 2.7, and 3.0 wt%.
[b]Noncoastdown operation with a 70% capacity factor.

it was inherent in iterative LP applications. However, the relaxation procedure was found to be successful in suppressing the oscillation. The study on the effect of several initial guesses revealed that the convergence is attained within a relative error of 10^{-5}, with relaxation factors r_f and $r_k = 0.75$ and error criterion $e = 5 \times 10^{-7}$. The difference between the nuclear fuel cost based on the continuous lot size and that based on an integer adjusted lot size was found to be small, contributing to the objective cost by a relative error of 10^{-4}. Though the present algorithm of TP search does not guarantee against the uniqueness of the optimum solution, almost all routes starting from

several points on the TP line converged to the same local optimum point. The local minimization during TP search appeared to converge within a relative accuracy of $\sim 10^{-4}$. These cost sensitivities are insignificant compared with the cost improvements and variations among the demonstrated numerical cases.

IV.D. Recovery Planning After Forced Outages

The importance of finding a feasible, if not optimum, cycle planning is enhanced, especially in the recovery transient after unexpected plant outages or forced power reductions. Suppose that something

TABLE VII

Optimum Coastdown Periods (days)

Cycles	1	2	3	4	5	6	7
Case IV[a]	1.88	3.85	3.44	2.98	5.00	0	0
Case VIII[b]	1.93	3.78	3.51	3.36	3.18	2.95	5.00

[a]Asymptotic case to equilibrium refuelings.
[b]Nonasymptotic case.

wrong occurred with fuel assemblies on the 150th day, which caused a reactor shutdown. Inspection will take 200 days, during which four suspected fuel assemblies will be removed and replaced by fresh assemblies with the same nuclear performance. The plant will restart on the 350th day. The power level will be kept at 40 and 70% of the rating power in the succeeding two cycles, respectively. The refueling date will not be altered in these two cycles. The other conditions are the same as specified in Table III. What is the best decision on the 150th day about the subsequent cycle strategy?

An optimization was attempted with noncoastdown condition (Case XV). A TP search (Case XVI) starting from the noncoastdown Case XV arrived at an optimum point. En route to the optimum point, a domain was observed where the fuel subproblem becomes infeasible. Optimized schemes are shown in Table VIII. Note that the fresh fuel loading is avoided in cycle 2, where the reactivity is abundant due to a low plant availability. The derived core-averaged fuel k_∞ variation at the optimum point (Case XVI) is shown in Fig. 8.

Another attempt of optimizing the lot size was made with the same lot pattern as in Case I, but it failed to initiate the TP search due to the infeasibility of fuel subproblem at the starting point, where constraint C2' associated with excessive reactivity was violated. Conventional way of refueling appears to be so limited that it cannot utilize the latent potentials for adapting the scheme to emergent situations.

V. CONCLUSIONS

Fuel cycle management was optimized with a wider scope on the utility power system. The study was made for the system consisting of a nuclear power plant and a replacement power station integrated into the system when the nuclear plant derates or shuts down. Optimization of nonequilibrium refueling together with cycle power scheduling was automatically carried out. A numerical simulation demonstrated that an economic saving amounts to 7.3% in nuclear fuel cost and 1.4% in system operat-

TABLE VIII

Recovery Refueling Scheme

(Asymptotic cases to equilibrium cycles beyond planning horizon)

Cycle 1 2 3 4 5 6 7 8 9 10 — Lot Pattern	Case XV	Case XVI	Enrichment (wt%)
1 1 0 0 0 0 0	22	20	2.0[a]
1 1 1 0 0 0 0	11	12	2.0[a]
1 1 0 1 0 0 0	18	19	2.0[a]
1 1 1 0 0 0 0	39	38	2.7[b]
1 1 1 0 1 0 0	6	6	2.7[b]
1 1 1 0 2 0 0	5	6	2.7[b]
2 2 1 1 0 0 0	40	39	3.35[c]
2 2 2 1 1 0 0	12	13	3.35[c]
1 1 1 0 0 0 0	4	4	2.0[d]
0 0 2 1 1 0 0	20	22	2.8[d]
0 0 2 1 1 1 0	15	12	2.8[d]
0 0 2 2 1 0 0	5	5	2.8[d]
0 0 0 2 1 0 0	4	0	2.8[d]
0 0 0 2 1 1 0	37	40	2.8[d]
0 0 0 2 1 1 1	6	7	2.8[d]
0 0 0 0 2 1 1	46	45	2.8[d]
(Equilibrium Pattern)			
0 0 0 0 2 1 1 1 0 0	1	1	2.8[d]
0 0 0 0 0 2 1 1 0 0	51	51	2.8[d]
0 0 0 0 0 2 1 1 1 0	1	1	2.8[d]
0 0 0 0 0 0 2 1 1 0	51	51	2.8[d]
0 0 0 0 0 0 2 1 1 1	1	1	2.8[d]

[a]Partially burnt to 5319 MWd/tU.
[b]Partially burnt to 5894 MWd/tU.
[c]Partially burnt to 3983 MWd/tU.
[d]Fresh fuel.

ing cost for a referenced example. Purchased fuels prepared for operations in a higher availability will be economically loaded with a considerable saving in a lower availability condition.

The flexibility can cope with the planning requirement for recovery from the forced plant outages. The recovery scheme is automatically generated or is checked for the feasibility if the present program is used; otherwise, one has to resort to conventional trial-and-error works, which are very likely to miss even the feasible solutions.

The present study assumed that the nuclear fuel burning inside the core had been purchased with the low price before the recent cost soaring, while the replacement power is generated with the present price of oil. Consequently, there was a big cost gap between nuclear and replacement powers that demerited the nuclear cost savings by the optimum
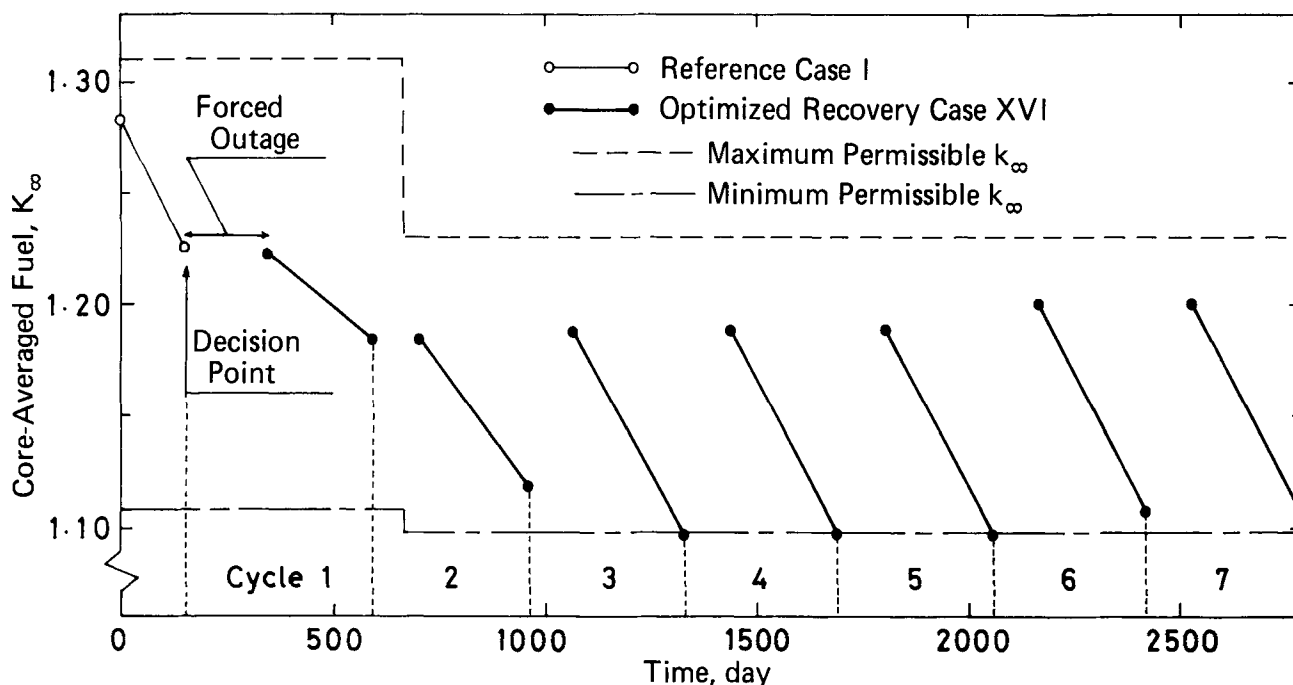
Fig. 8.   Core-averaged fuel k_∞ in recovery planning Case XVI.

refueling and coastdown operation, relative to the cost saving efforts to increase the plant availability. Moreover, the constraint imposed by the regulatory authority on the maximum cycle length between planned refueling and/or inspection outages played the essential role in limiting the availability, which may otherwise be extended by designing the core with longer life.

However, the story would be quite different, depending on the assumed environment of safety-related regulation and economic factors. Economic incentive for this type of study will be more enhanced in varying complicated environments, such as for the case where nuclear units have to load-follow in off-peak periods, probably with more rigid bases on the plant integrity. It is worth noting that the proposed method can automatically provide the incremental fuel cost [following the same method for cost gradient vector, Eq. (36)], which is needed in load-follow ages, for interfacing the nuclear unit planner to the system economic-load-dispatcher such as ORSIM (Ref. 15).

ACKNOWLEDGMENTS

REFERENCES

1. G. J. BONK, R. L. CROWTHER, and O. A. THOMPSON, "Interaction Between Nuclear Plant Loading Changes and Nuclear Fuel Costs," Proc. American Power Conf., 33, 253 (1971).

2. I. WALL and H. FENECH, "The Application of Dynamic Programming to Fuel Management Optimization," Nucl. Sci. Eng., 22, 285 (1965).

3. R. L. STOVER and A. SESONSKE, "Optimization of BWR Fuel Management Using an Accelerated Exhaustive Search Algorithm," J. Nucl. Energy, 23, 673 (1969).

4. A. SUZUKI and R. KIYOSE, "Application of Linear Programming to Refueling Optimization for Light Water Moderated Power Reactors," Nucl. Sci. Eng., 46, 112 (1971).

5. T. O. SAUAR, "Application of Linear Programming to In-Core Fuel Management Optimization in Light Water Reactors," Nucl. Sci. Eng., 46, 274 (1971).

6. H. MOTODA, J. HERCZEG, and A. SESONSKE, "Optimization of Refueling Schedule for Light Water Reactors," Nucl. Technol., 25, 477 (1975).

7. T. HOSHINO, M. TAKAHASHI .and Y. FUJII, "Optimization of In-Core Fuel Management, Cycle Period and Power Scheduling of Nuclear Power Plants by Large Scale Nonlinear Programming," Proc. Conf. Computational Methods in Nuclear Engineering, April 15-17, Charleston, South Carolina, CONF-750413, Vol. 1, p. III-115, U.S. Energy Research and Development Administration (1975).

8. T. KUBOKAWA and R. KIYOSE, "Optimization of In-Core Fuel Management by Integer Linear Programming," *Proc. Conf. Computational Methods in Nuclear Engineering*, April 15-17, Charleston, South Carolina, CONF-750413, Vol. 1, p. III-135, U.S. Energy Research and Development Administration (1975).

9. J. O. MINGLE, "In-Core Fuel Management via Perturbation Theory," *Nucl. Technol.*, 27, 248 (1975).

10. P. CIVITA, P. FORNACIARI, and T. MAZZANTI, "Optimal Operational Strategy in Nuclear Fuel Management," *Nucl. Technol.*, 14, 116 (1972).

11. *Proc. Mathematical Models and Computational Techniques for Analysis of Nuclear Systems*, April 9-11, 1973, Ann Arbor, Michigan, CONF-730414, U.S. Atomic Energy Commission (1973).

12. H. Y. WATT, M. BENEDICT, and E. A. MASON, "Methods for Calculating Incremental Fuel Costs for Nuclear Energy," *Proc. Mathematical Models and Computational Techniques for Analysis of Nuclear Systems*, April 9-11, 1973, Ann Arbor, Michigan, CONF-730414, p. V-58, U.S. Atomic Energy Commission (1973).

13. J. T. RHODES, "Operational Planning of Multi-Nuclear Unit Systems," in a Collection of Papers Presented at the Nuclear Utilities Planning Methods Symp., January 16-18, 1974, Chattanooga, Tennessee, ORNL-TM-4443, Oak Ridge National Laboratory (1974).

14. A Collection of Papers Presented at the Nuclear Utilities Planning Methods Symp., January 16-18, 1974, Chattanooga, Tennessee, ORNL-TM-4443, Oak Ridge National Laboratory (1974).

15. J. C. TURNAGE and B. E. PRINCE, "A Computer Code (ORSIM) for the Simulation and Optimization of Utility System Operation with Nuclear Plants," in a Collection of Papers Presented at the Nuclear Utilities Planning Methods Symp., January 16-18, 1974, Chattanooga, Tennessee, ORNL-TM-4443, Oak Ridge National Laboratory (1974).

16. D. L. FARRAR, "Application of a Simulation Model (ORSIM) to Electric Generation Planning," in a Collection of Papers Presented at the Nuclear Utilities Planning Methods Symp., January 16-18, 1974, Chattanooga, Tennessee, ORNL-TM-4443, Oak Ridge National Laboratory (1974).

17. W. STEVENS, W. FLOURNOY, and D. PILMER, "Reduced Enrichment Requirements Through Optimal Cycle Coastdown, San Onofre Unit 1," *Trans. Am. Nucl. Soc.*, 24, 214 (1976).

18. D. E. KUSNER, M. A. MANN, and P. J. TURINSKY, "Planned Cycle Stretchout in PWRs," *Trans. Am. Nucl. Soc.*, 27, 467 (1977).

19. R. B. ROTHROCK, "Interstage Coupling Effects in LWR Fuel Management," in a Collection of Papers Presented at the Nuclear Utilities Planning Methods Symp., January 16-18, 1974, Chattanooga, Tennessee, ORNL-TM-4443, Oak Ridge National Laboratory (1974).

20. L. S. LASDON, *Optimization Theory for Large Systems*, The Macmillan Company, New York (1970).

21. J. B. ROSEN, "The Gradient Projection Method for Nonlinear Programming. Part I—Linear Constraints," *SIAM J. Appl. Math.*, 8, 181 (1960).

22. Y. NAGINO, M. YOKOTE, and S. KUWABARA, Private Communication (1977).

23. T. HOSHINO, "FAPMAN-5, A Computer Code for Optimum Operation of LWR Power Stations," Report No. 174, Technical Reports of the Institute of Atomic Energy, Kyoto University (1977).

ELECTROCHEMICAL EXTRACTION OF HYDROGEN FROM MOLTEN LiF-LiCl-LiBr AND ITS APPLICATION TO LIQUID-LITHIUM FUSION REACTOR BLANKET PROCESSING

W. F. CALAWAY *Argonne National Laboratory*
Chemical Engineering Division, 9700 South Cass Avenue
Argonne, Illinois 60439

The electrochemical evolution of hydrogen from a molten solution of LiF-LiCl-LiBr containing small quantities of LiH and saturated with metallic lithium has been demonstrated. The evolved hydrogen is recovered from the melt by sweeping the hydrogen electrode with a circulating stream of argon and subsequently trapping the hydrogen from the argon with a hot titanium getter bed. It is found that by continually gettering the argon, 100 ± 2% of the hydride present in the molten salt, at a concentration of 1 wppm, is recoverable.

Results of metallographic examinations of stainless-steel components in contact with the salt solution during the experiments indicate some evidence of surface attack (10 to 15 μm) and intergranular penetration (30 to 50 μm), but extrapolated corrosion rates are generally small (~0.2 mm/yr). These results incorporated into a reevaluation of the molten-salt extraction process, as it applied to tritium recovery from a liquid-lithium fusion reactor blanket, indicate a more favorable processing capability than was previously expected.

INTRODUCTION

First-generation fusion power reactors are expected to operate by means of the deuterium-tritium (DT) reaction[1,2]; hence, they will almost certainly have to breed their own tritium. Presently, liquid lithium is considered to be one of the more likely breeding materials.[3] This particular medium has the advantage that it can serve both as the tritium breeding blanket and the primary coolant for the reactor.

The concentration of tritium that can be tolerated in a liquid-lithium fusion reactor blanket has been discussed extensively. Both economic and safety considerations dictate rather low maximum allowable tritium concentrations for the blanket, and it is generally agreed that safety considerations set the more stringent constraint.[4] In particular, if liquid lithium is to be used as both the breeding material and reactor coolant, the steady-state concentration of tritium must be maintained at a low enough level to prevent significant permeation of tritium through the blanket structure and primary heat exchanger. It is believed that this requirement will constrain the allowable tritium concentration in the blanket to <1 wppm (Ref. 5). Thus, an efficient method for extracting and recovering very low concentrations of tritium from liquid lithium is essential to the development of liquid-lithium blanket concepts for fusion reactors.

The extraction of 1 wppm of tritium from liquid lithium is a difficult task. Lithium has great affinity for hydrogen isotopes, as indicated by the low hydrogen partial pressures found over lithium-lithium hydride mixtures[6] and by the high solubility of lithium hydride in lithium.[7] Hence, conventional purification procedures such as cold trapping and distillation seem impractical. Other, more elaborate, techniques for liquid-lithium blanket processing have recently been reviewed.[8] Proposed methods that presently appear feasible include

1. exothermic solid getters[9]

2. permeable windows[10]

3. liquid alloy getters[11]

4. molten-salt extraction.[6,12,13]

The latter method is particularly appealing because the recovery of tritium from a molten salt is much simpler than recovery from liquid lithium. In addition, this process may also be useful in removing other nonmetallic impurities (e.g., hydrogen, deuterium, carbon, nitrogen, and oxygen) that would also tend to accumulate in a liquid-lithium blanket.

Studies[12] previously conducted at Argonne National Laboratory (ANL) showed that tritium (present as LiT) is preferentially extracted from liquid lithium by selected molten salts when the two liquids are contacted. Based on this study, a molten-salt extraction process was conceived in which tritium could be removed from a liquid-lithium fusion reactor blanket by

1. contacting a portion of the lithium from the blanket with a molten salt

2. separating the salt and metal phases

3. returning the purified lithium to the blanket

4. processing the salt to recover the tritium.

The thrust of more recent work on the development of this process has been to experimentally verify the salt processing step. To this end, a study was initiated to evaluate possible methods for removing deuterium and protium from molten salts.[6,13]

The extents of extraction of protium, deuterium, and tritium from a molten salt are expected to be similar since all three hydrogen isotopes have nearly identical chemical properties. Thus, the two non-radioactive hydrogen isotopes can serve as substitutes for tritium in the salt processing experiments with confidence that tritium extraction will closely follow the results obtained with protium and deuterium.

Reasonably well established techniques for purifying fused alkali-halide salts seemed at the outset to be applicable to the tritium salt processing problem. Nonmetallic elements have been removed from molten salts using both chemical sparging[14,15] and electrochemical techniques.[16] These methods can be adapted to recovering tritium in a blanket processing scheme provided that

1. the metallic lithium that is dissolved in the salt does not adversely affect the recovery

2. the tritium that is extracted is recoverable in a form suitable for reinsertion into the fusion-reactor fuel cycle.

Previous experiments at ANL on lithium/hydrogen galvanic cells[17] demonstrated that hydrogen could be electrochemically generated from LiCl-KCl eutectic containing a high concentration of lithium hydride. More recent studies[6,13] conducted at ANL examined recovery of hydrogen isotopes from molten salts at the low concentrations relevant to lithium processing. In these studies, protium and deuterium were sparged

from LiCl-KCl and LiF-LiCl-LiBr by the reaction of HCl gas with LiH and LiD. The results indicated that the concentration of hydrogen isotopes in certain molten salts can be reduced to <5 wppm by chemical sparging.

Experiments to recover protium and deuterium at low concentrations from molten salts by electrochemical evolution were also pursued.[13] Results from experiments with a graphite anode demonstrated the possibility of recovering hydrogen isotopes by this technique. However, complications that were attributed to the reaction of lithium with the graphite electrode could not be resolved. For this reason, experiments to examine the electrochemical recovery of hydrogen from a molten salt using a nonreactive hydrogen electrode were initiated. The results of the latter experiments are the subject of this paper.

EXPERIMENTAL

The experiments were designed to simulate as closely as possible the salt processing step of a molten-salt extraction system. The experimental apparatus is depicted in Fig. 1. A stainless-steel gas handling system is connected to a vacuum-tight furnace well containing a pot of molten salt and having a cover gas of ultra-high-purity argon at 105 kPa (800 Torr). The argon is circulated through the apparatus in a closed loop by a stainless-steel bellows pump (Metal Bellows Company model MB-21) at a flow rate of $\sim$10 cm^3/s. The gas is dispersed through the salt by a hollow porous bubbler and then flows past a controlled leak valve that couples the gas stream with a mass spectrometer system. In processing the salt solutions, the hydride ion is converted to gaseous hydrogen, which enters the argon stream. Thus, the rate and extent of hydrogen extraction from the salt can be followed by continuously analyzing the gas stream with the mass spectrometer. A titanium bed heated to 500°C can be switched into the gas stream (via a four-way valve) and used as a getter to collect the gaseous hydrogen and purify the argon. Metallic lithium and lithium hydride are added to the salt through a set of ball valves that act as an air lock for the well. Sufficient lithium is added to the salt to simulate the anticipated condition of the salt when it returns from the lithium contacting operation in an actual molten-salt processing system.

The mass spectrometer is a Varian VGA-100 quadrupole gas analyzer installed in a metal vacuum manifold attached to a 2.5 X 10^{-2} m^3/s ion pump. The ultimate vacuum attainable in the manifold is $\sim$1 X 10^{-8} Pa ($\sim$10^{-10} Torr). During experiments, the controlled leak valve (Granville-Phillips series 203) connecting the argon stream to the vacuum system is set so that a steady-state pressure of 1 X 10^{-5} Pa ($\sim$10^{-7} Torr) is maintained in the manifold. At this pressure, the flow rate into the vacuum
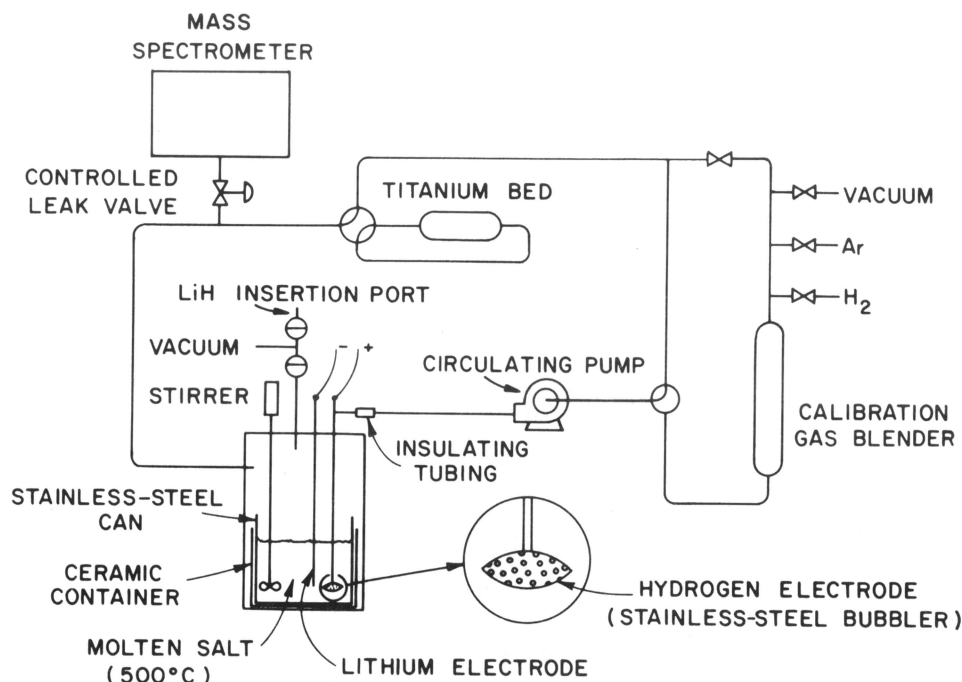
Fig. 1.   Schematic diagram of the experimental apparatus used in the molten-salt processing experiments.

system is such that the total contents of the manifold are replaced several times a second, thus ensuring that the actual gas-stream composition and the composition measured by the mass spectrometer are identical even during short-term fluctuations. Operated in this configuration, the mass spectrometer is capable of detecting (signal/noise = 1) $\sim 0.1\%$ H_2 in the argon. This concentration corresponds to ~ 0.1 wppm of hydrogen recovered from the salt. Calibration of the mass spectrometer is accomplished by recording the mass spectrometer signal while circulating known quantities of hydrogen in the argon stream. The calibration was generally performed once each day and was always done after the controlled leak valve was readjusted.

All components in contact with either molten salt or liquid lithium are made of stainless steel. The argon bubbler is a standard stainless-steel "beaker filter" (Pall Corporation). It consists of two concave sintered Type 316L stainless-steel disks (5-μm mean pore size) welded to form an ellipsoid with a welded tube extending from one face. The bubbler is also used as the anode of the cell (hydrogen electrode); with this arrangement, the hydrogen generated by electrolysis should be swept out of the salt by the circulating argon before the lithium that saturates the salt can back-react with the hydrogen. The lithium electrode is a Type 304 stainless-steel tube, sealed at the bottom and immersed in the salt. It is continuously in contact with a small adhering pool of molten lithium near the salt surface. Experiments

were carried out at 500°C. The temperature of the melt is measured to an accuracy of ±2°C with a Chromel-Alumel thermocouple placed inside the lithium electrode. To ensure an equilibrium solution and a uniform temperature, the salt was mixed with a magnetically coupled stirrer having a Type 304 stainless-steel paddle. The electrodes, stirrer, and other well penetrations were electrically insulated by Teflon sleeves.

The molten salt used in the experiments was LiF-LiCl-LiBr (22-31-47 mol%). It was prepared from the individual (reagent-grade) salts by

1. drying them at 250°C under vacuum overnight

2. melting them under a helium atmosphere

3. removing particulate matter from the salt solution by a settling and skimming process

4. electrochemically purifying the melt using an aluminum cathode and a carbon anode.[16]

The melting point of the purified salt was found to be 445°C, in agreement with its reported value.[18] The lithium metal was obtained from the Foote Mineral Company and had a reported purity of 99.98%. The lithium hydride was prepared by direct reaction of lithium metal with hydrogen (research grade). All materials were stored in a helium glove box designed to maintain concentrations of water, oxygen, and nitrogen below 1 wppm. The salt was loaded into the furnace well inside the glove box,

and the sealed well was then removed and connected to the experimental apparatus. The lithium and lithium hydride were weighed in the glove box and placed in tubes with one closed end and a ball valve to seal the other end. These sealed tubes were individually connected to the ball valve assembly on the well. After evacuation to remove air from the space between the valves and helium from the sealed tube, the lithium and lithium hydride were dropped into the molten salt by opening both ball valves. Generally between 0.2 and 0.5 g of lithium was added to the salt in this manner to saturate the salt with lithium. For each experiment, a lithium hydride crystal weighing between 8 and 21 mg was added to 1.25 kg of LiF-LiCl-LiBr, via the ball valves, to produce a solution with a hydride ion concentration of between 1 and 2 wppm.

Hydrogen extraction was accomplished by electrolyzing the melt at an electromotive force (emf) below the decomposition potential of the salt. The potential applied to the electrodes was furnished by a 0- to 10-V adjustable power supply (Lambda model LP-530-FM). The electrode current was monitored by continuously recording the voltage drop across a 0.1-Ω resistor in series with the cell. The potential drop across the resistor was always small enough (<50 mV) that the potential across the electrodes was taken to be constant and identical to the potential across the terminals of the power supply. Experiments were conducted under constant voltage conditions with emfs ranging from 0.4 to 1.2 V. In some runs, the emf was applied to the cell before the lithium hydride addition and in other runs after the hydride addition. Both the mass spectrometer analysis of the gas stream and the current of the electrochemical cell were used to follow the progress of the hydrogen extraction as a function of time.

Two separate types of experiments were performed to study the electrochemical recovery of hydrogen from molten salts. One series of experiments was conducted under conditions in which the extracted hydrogen was allowed to accumulate in the argon stream circulating through the salt. After the extraction appeared to be complete (i.e., after a stable mass spectrometer signal was obtained), the titanium bed was valved in to remove the hydrogen. These experiments permitted continuous monitoring of the hydrogen extraction and recovery by mass spectrometric analysis of the gas stream and provided confirmation that molecular hydrogen was indeed being liberated. The remaining experiments were conducted with the titanium bed on stream throughout the runs. The hydrogen gas generated in these experiments was gettered on a continuous basis and thus never accumulated in the argon stream. (This was confirmed by the inability to detect hydrogen in the argon with the mass spectrometer.) The latter

type of experiment is particularly useful in deducing parameters for the electrochemical evolution, since there is virtually no molecular hydrogen in the circulating gas stream to back-react with the lithium in the salt.

Upon completion of the electrochemical extraction experiments, the hydrogen and lithium electrodes and the stirrer paddle were examined for evidence of corrosion by the molten LiF-LiCl-LiBr and metallic lithium. The electrodes and paddle were removed from the salt and soaked in water to dissolve excess salt and lithium. They were then sectioned, mounted, and polished for microscopic and electron microprobe analysis. Samples were first examined and photographed with a Reichart metallurgical optical microscope. For examination at higher magnification and for elemental analysis, an Applied Research Laboratories EMX-SM electron microprobe was used.

RESULTS AND DISCUSSION

Electrochemical Studies

Results for a typical electrochemical experiment to recover hydrogen from LiF-LiCl-LiBr using a stainless-steel anode are given in Fig. 2. The upper trace in Fig. 2 is the current through the salt, and the lower trace is the corresponding H_2 concentration in the argon stream as determined mass spectrometrically. In this experiment, the LiH was added before a potential was applied across the electrodes. After the LiH was dissolved in the salt and the solution was well mixed, an emf of 1V was applied. As can be observed from the current and mass spectrometer traces in Fig. 2, hydrogen is rapidly evolved from the salt as soon as the voltage is applied. When the gas flow is directed over the hot titanium bed, the H_2 is gettered from the argon stream, and the current and mass signals decrease.

The parameter of principal interest in this study is the recovery efficiency, which is defined as the weight of hydrogen recovered from the salt divided by the weight of hydrogen added to the salt (expressed as a percentage). This parameter is determined from the weight of lithium hydride added to the system and the magnitude of the calibrated mass spectrometer signal. The recovery efficiency calculated in this manner for the experiment in Fig. 2 was 90%. Experiments similar to the one described above were carried out at several different applied potentials to determine how the recovery efficiency varies with the electrode emf. Results for this series of experiments are presented in Fig. 3. When the applied potential is at or below 0.6 V, no change in either the current through the salt or the H_2 concentration in the argon is detected as LiH is added to the salt. Hydrogen recovery from the salt begins at an
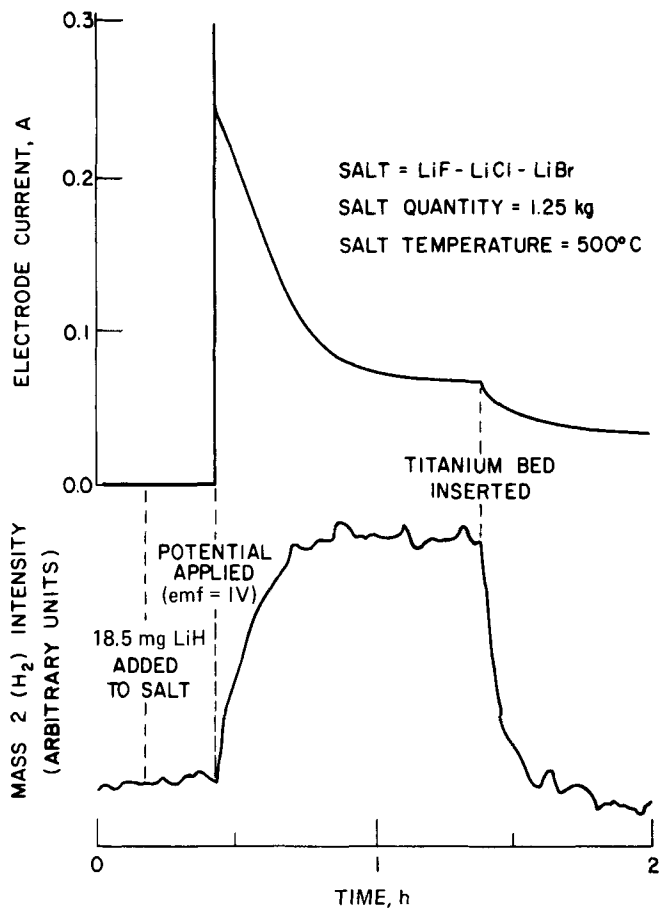
Fig. 2.   Results of a typical experiment to recover hydrogen electrochemically from molten LiF-LiCl-LiBr.

Fig. 3.   Variation of the hydrogen recovery efficiency of the electrochemical process as a function of the applied emf.

Fig. 4.   Comparison of the electrode current for extraction experiments in which a getter bed was used (a) and bypassed (b).

emf of ~0.7 V; the recovery efficiency increases to a maximum near 0.9 V and then appears to decline.

When the titanium bed was in line throughout the experiment, little or no hydrogen was detected in the argon stream by the mass spectrometer. Shown in Fig. 4 is the cell current for two similar experiments, one with the bed in (top trace) and one with the bed out (bottom trace). In both these experiments, an emf of 1 V was applied across the electrodes before the LiH was added to the salt. Note that with the titanium bed in, the current asymptotically approaches the previous base line value, whereas without the titanium bed, the current approaches a value slightly higher than the original.

The results from electrochemical experiments without the titanium bed in line indicate that hydrogen can be readily extracted from LiF-LiCl-LiBr at a concentration as low as 1 wppm. As typified in Fig. 2, time-resolved mass spectrometer analysis of the circulating gas stream reveals that the electrochemical process rapidly generates molecular hydrogen, which immediately enters the argon sweep gas. In addition, the calculated recovery efficiencies indicate that during the electrochemical process, an appreciable (~1.5-kPa) hydrogen partial pressure is
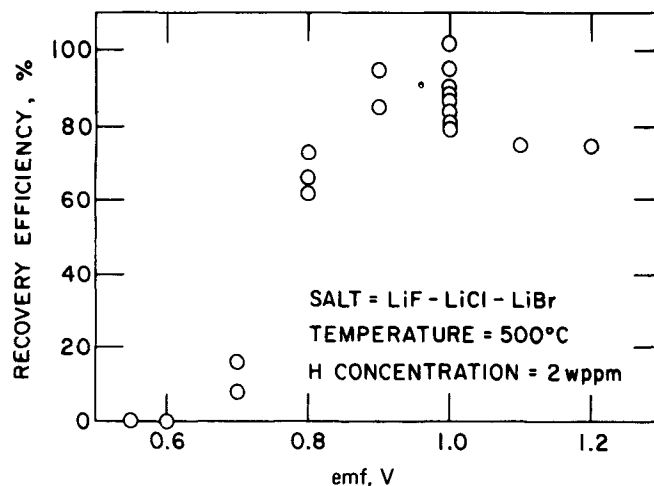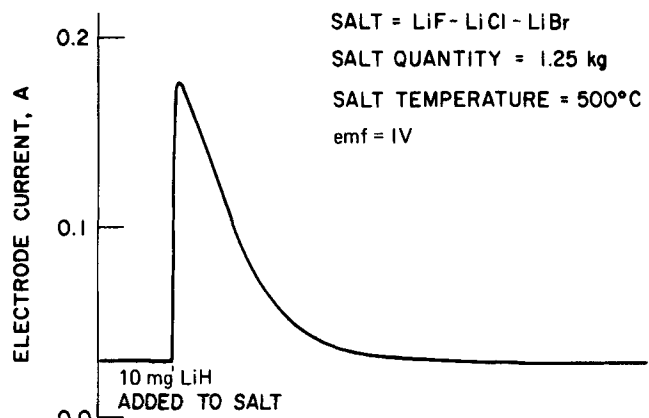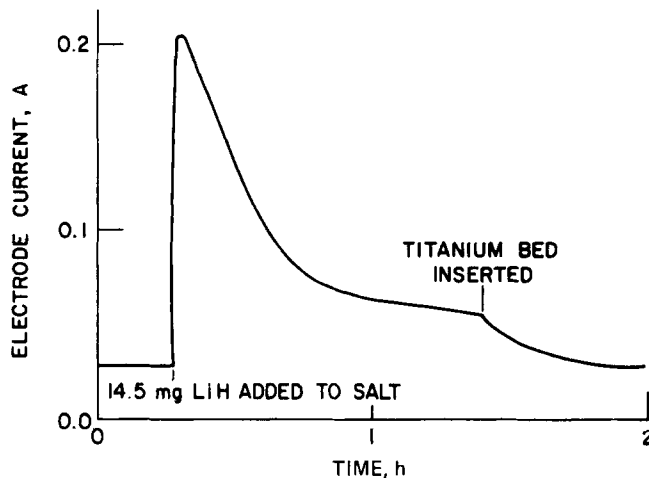
maintained above a lithium-saturated molten salt. Similar proof of the effectiveness of electrochemical processing is deduced from the cell current. When a potential is applied to the lithium hydride/lithium salt solution, an immediate increase in the cell current occurs, as is observed in Fig. 2. The spike in the current is due to establishment of the polarization layer around the electrodes. The current remaining after the spike can be considered as consisting of two components:

1. a current associated with electrolyzing the LiH (denoted hydride current)

2. a current associated with the conductivity of the lithium-saturated salt (denoted background current).

As hydrogen gas forms, the hydride ion is depleted from the salt and the current decays, asymptotically approaching a value slightly higher than the background current. The presence of this small current above the background level indicates that a small steady-state hydride concentration remains in the salt, owing to the equilibrium established between the rate of electrochemical evolution of hydrogen and the rate of back-reaction of gaseous hydrogen with the metallic lithium dissolved in the salt.

The competition between the electrochemical extraction and the lithium-hydrogen back-reaction was expected. The fact that the equilibrium is shifted to the extent that >80% of the hydrogen can be maintained in the gas phase says much for the effectiveness of the argon-sparged electrode in carrying hydrogen out of the lithium-saturated salt. Recovery of the residual hydride in the salt can be accomplished by reducing the concentration of hydrogen in the argon, which is done in these experiments by introducing the titanium getter. By lowering the activity of the hydrogen gas, back-reaction with lithium in the salt is virtually eliminated, thus allowing complete recovery. When the argon stream is directed through the titanium bed, the mass 2 signal returns to its background level as hydrogen is gettered from the argon. At the same time, the cell current returns to its background value as the remaining hydride is extracted from the salt.

As depicted in Fig. 3, the recovery efficiency improves when the emf is increased from 0.6 to 0.9 V. By increasing the applied potential, the rate of hydrogen generation increases and the hydride-hydrogen equilibrium is shifted toward the gas phase. It appears that the equilibrium cannot be shifted any further toward gaseous hydrogen by increasing the applied potential beyond 0.9 V. The rate of hydrogen evolution probably reaches a maximum at this point owing to mass transfer effects. A possible explanation for the slight decline in the hydrogen recovery efficiency at potentials above

1.0 V is the evolution of hydrogen in other chemical forms, e.g., CH_4, HBr, or H_2O. (The electrochemical evolution of methane from a molten salt containing Li_2C_2 and LiH has been observed.[19])

Two additional experimental parameters were examined. In several experiments, the salt was not stirred during the extraction. No change was observed in either the recovery rate or the recovery efficiency, compared with values obtained with stirred salt. Another experiment was performed in which the argon was not circulated. The current increased with the addition of the LiH but declined from its peak value only slightly before it leveled off. (The current dropped only ~35% from its peak value.) Once the argon circulation was started again, the extraction proceeded in the usual fashion. This experiment verified that the flow of gas over and through the anode is responsible for the high recovery rate and recovery efficiency. The fact that the current declined only slightly from its initial value in this experiment indicates that most of the hydrogen remains in the melt. It is believed that the argon flow sweeps hydrogen from the anode and that the absence of this sweeping mechanism allows bubbles of hydrogen to accumulate on the surface until back-reaction of hydrogen with dissolved lithium becomes significant.

A quantitive measure of the effectiveness of the sparged electrode was deduced by calculating the amount of current required for extraction in experiments with the titanium bed in line. For each of these experiments, the current time envelope was integrated to obtain the current efficiency (i.e., moles of hydrogen extracted/moles of electrons supplied above background current). An efficiency of >95% was consistently observed, indicating that <5% of the hydrogen is back-reacting with the metallic lithium before it is liberated from the melt. The high current efficiency allows an accurate estimate of the hydrogen recovery efficiency to be made from the cell current. If it is assumed that the rate of hydrogen-lithium back-reaction is directly proportional to the rate at which hydrogen is being electrochemically evolved, then the hydride ion concentration as a function of time, $C(t)$, can be calculated from

$$C(t) = C(0) - E \int_0^t i dt , \qquad (1)$$

where

E = current efficiency

i = current

t = time.

For several experiments, Eq. (1) was integrated for different values of time, and the calculated hydride concentration was plotted against the current yielding an average slope of ~4 wppm H^-/A. From this it is

possible to estimate the hydride ion concentration in the salt from the current it produces. For experiments performed without the titanium bed, this method can be an alternative for calculating recovery efficiencies. As an example, examine Fig. 2 where the amount of LiH originally added to the salt was 18.5 mg or 1.85 wppm H^-. The magnitude of the current above its background level is 35 mA, and the hydride ion concentration remaining in the salt is 4 wppm $H^-/A \cdot$ 0.035A = 0.14 wppm H^-. The ratio of the hydride ion concentration remaining in the salt to the amount added is 0.14 wppm $H^-/1.85$ wppm $H^- = 0.08$, and thus the recovery efficiency is 92%. This compares favorably with the recovery efficiency of 90% calculated from the mass spectrometer results.

The current can also be used to estimate the uncertainty in the recovery efficiency for experiments with the titanium bed in line. In all experiments of this type and also in experiments in which the titanium bed was switched in after a steady state was reached, the current returned to its background level as the extraction progressed (see Fig. 4). This return to background indicates that 100% recovery of hydrogen from the salt is achieved when the getter bed is used. In each experiment, it was possible to detect current changes of less than ±5 mA. By the use of information derived from Eq. (1), it is estimated that an uncertainty of 5 mA in the current measurement yields a minimum detectable limit of 0.02 wppm H^- in the salt. Thus, it is determined from analysis of the electrode current that extraction of hydrogen from the salt at the 1-wppm level can be accomplished with a recovery efficiency of 100 ± 2% for experiments in which a getter bed is used to prevent hydrogen accumulation in the argon stream.

Process Development and Salt Selection

The work described in this paper has two immediate goals. The first is to experimentally demonstrate the salt processing step of the molten-salt extraction scheme under conditions applicable to purifying a liquid-lithium fusion reactor blanket. The second (assuming successful completion of the first goal) is to examine and select the most promising salt processing technique and an appropriate molten salt for further development in a larger scale molten-salt extraction system. The first objective has been achieved for electrochemical processing as reported here and for processing by chemical sparging as reported previously.[6,13] In regard to the second goal, electrochemical extraction using LiF-LiCl-LiBr appears at present to be the best choice for near-term development, as discussed below.

Electrochemical evolution and chemical sparging are equally efficient as techniques for processing the salt. Both methods allow rapid and complete recovery of hydrogen at very low levels. Nevertheless,

electrochemical extraction is believed to be the better method for the following reasons:

1. Electrochemical evolution is simpler and cleaner in that no reactive chemicals such as HCl are required.

2. Chemical sparging results in reaction of the lithium that saturates the salt during the processing with a consequent loss of substantial amounts of lithium from the blanket.

3. Electrochemical processing lends itself more readily to continuous collection of tritium and thus has a safety advantage over a process in which tritium is allowed to build up in the gas stream (as required by gas sparging).

The salt selection was made primarily on melting point considerations. For lithium molten salt mixtures to be adequately contained in stainless steel, it is imperative that the system be maintained at or below 500°C (Ref. 20). Allowing for a reasonable leeway in the operating temperature, a molten salt with a melting point ≤450°C is required. A number of binary and ternary alkali-halide mixtures meet this criterion. In light of previous work[13] with LiCl-KCl, an all-lithium-ion salt mixture seems the best choice. Within these constraints, the ternary mixtures LiF-LiCl-LiX (where X = bromine or iodine) are the only possibilities, and the bromide appears to be the better selection on the base of stability of the salt and the problems associated with introduction of halides into the lithium blanket. (The presence of halogens in the lithium blanket is of prime concern, since they can adversely affect the tritium breeding rate and can undergo undesirable transmutation reactions.) In this regard, the consequences of the presence of chloride in a liquid-lithium fusion reactor blanket were found in an earlier analysis[12] to be negligibly small. The effect of fluoride is expected to be even smaller.[21] Bromide has a larger cross section, and its presence in the blanket could be significant. Neutronics calculations to determine the impact of bromine on tritium breeding and formation of long-lived radioactive isotopes have recently been carried out.[21] It is estimated that at a concentration of 100-appm bromide in lithium the neutron flux available for tritium breeding is reduced by only ~0.5% as a result of Br(n,total) reactions. (Although the solubility of LiBr in lithium has not been measured, the measured values of the solubility of NaCl and NaBr in sodium,[22] KCl and KBr in potassium,[23] and LiCl in lithium[24] suggest that the saturation solubility of LiBr in lithium will be <100 appm at 500°C.)

Examination of transmutation reactions involving bromine revealed the formation of ^{79}Se via the reaction

$$^{79}Br\,(n,p)\,^{79}Se \xrightarrow[\ 7 \times 10^4\,yr\ ]{\beta^-} \ ^{79}Br\ (no\ gamma)\ .$$
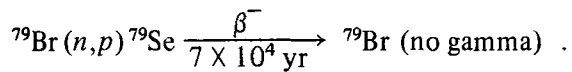
This is the only long-lived radioactive isotope produced by the presence of the bromide in the lithium. It is worth noting that no gamma radiation is associated with the decay of ^{79}Se and that the intensity of β^- emission from ^{79}Se is much less than the intensity of emission from the tritium β^- decay. For example, assuming a bromine concentration of 100 appm in the lithium blanket, the induced radioactivity in the blanket after one year of operation will be $<4 \times 10^4$ Bq/kg(Li), while activity associated with a tritium concentration of 1 wppm in the blanket is $\sim 2 \times 10^{11}$ Bq/kg(Li). Thus, it appears from a neutronics point of view that fluoride, chloride, and bromide at <100-appm levels are acceptable as impurities in liquid-lithium fusion reactor blankets.

Post-Experimental Corrosion Examination

The electrodes and the stirrer paddle depicted in Fig. 1 were examined for corrosion effects after exposure to the lithium-saturated LiF-LiCl-LiBr for ~ 2000 h at $\sim 500°C$. For approximately half of that time, an emf had been applied across the electrodes and the stirrer was in motion. In addition, for ~ 6 h during these studies, the solution temperature was at $600°C$ due to plugging difficulties. Metallographic analysis revealed grain boundary penetration to a maximum depth of ~ 50 μm. Photomicrographs of the stirrer paddle showing the extent of the attack are presented in Fig. 5. A microprobe scan across one of the grain boundaries of the stirrer is given in Fig. 6. All components examined had a surface depletion of iron, nickel, and chromium to a depth of ~ 15 μm. In addition, the stirrer had chromium enrichment at the grain boundaries.

The metallographic evidence suggests that the corrosion of the stainless steel in these experiments follows a mechanism more closely associated with liquid-lithium corrosion than with molten-salt corrosion. This tentative conclusion is based on the following observations:

1. The experimentally measured corrosion rate of ~ 200 μm/yr is nearer that expected for lithium corrosion[20,25] than that for molten salt corrosion.[26,27]

2. Nickel is preferentially depleted from grain boundaries, as would be expected for lithium penetration.[25]

3. Chromium appears to accumulate at the grain boundaries, again suggesting lithium penetration rather than salt penetration, since molten salts would more than likely cause chromium depletion.[27]
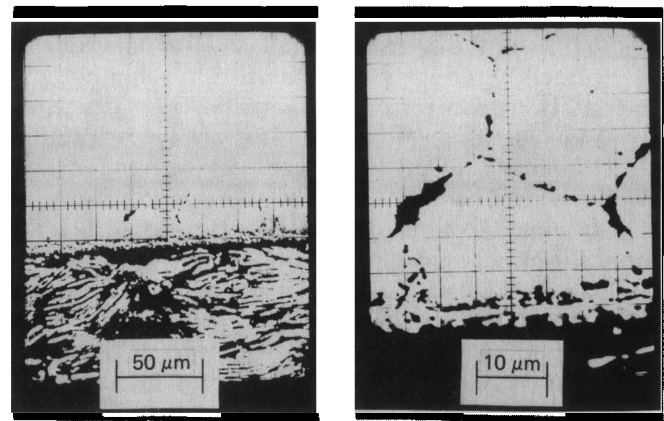
Fig. 5.   Magnified section of a Type 304 stainless-steel stirrer after immersion in lithium-saturated LiF-LiCl-LiBr for ~ 2000 h at $500°C$.
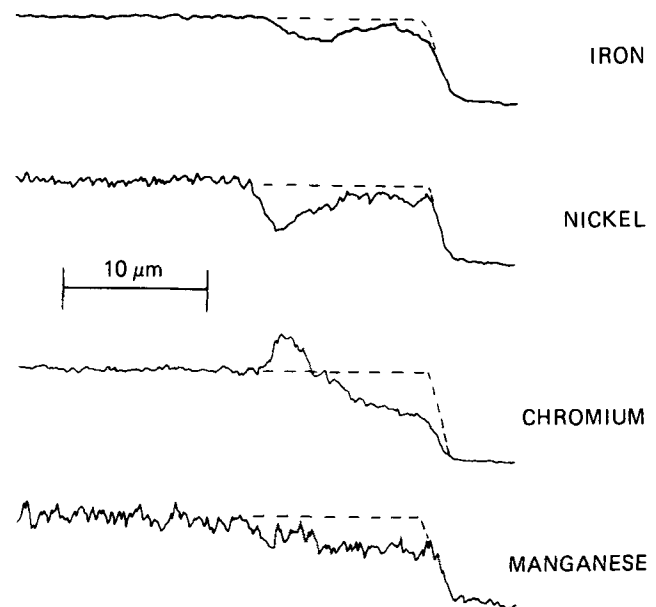
Fig. 6.   Typical electron microprobe scans showing the composition of the Type 304 stainless-steel stirrer after immersion in lithium-saturated LiF-LiCl-LiBr for ~ 2000 h at $\sim 500°C$. The dotted lines are electron microprobe scans of Type 304 stainless steel not exposed to the lithium salt solution.

(However, the observed chromium depletion at the surface of the stainless steel may be an indication that dissolution of chromium by the salt is also occurring.)

It is not clear from these experiments whether the corrosion of stainless steel in the salt-lithium solution was greater than it would have been in liquid lithium alone. The rate of grain boundary penetration is higher than the rate expected for purified (gettered) lithium.[26] However, the exposure of the metal to the molten solution for several hours at $600°C$ may have

been more responsible for the depth of the observed attack than the exposure for a much longer time at 500°C.

EVALUATION OF THE MOLTEN-SALT EXTRACTION SCHEME

In applying the experimental results to an analysis of the applicability of the molten-salt extraction scheme for fusion reactor blanket processing, it is assumed that the chemical behavior of tritium will be similar to that of the other hydrogen isotopes. Previous experiments with protium and deuterium revealed no significant isotope effect.[13] Therefore, salt processing experiments that are reported here for 1 wppm of hydrogen should correspond to tritium experiments at a concentration of $\sim$3 wppm of tritium. To calculate the tritium concentration in a lithium circuit that would be necessary to produce a 3-wppm solution of tritium in the salt after contact of the two phases, the distribution coefficient between the two phases must be known. Although this parameter has not been measured for LiF-LiCl-LiBr/Li, volumetric distribution coefficients for similar salt/lithium systems are in the range from 4.0 (for LiF-LiCl/Li eutectic) to 1.2 (for LiBr-RbBr/Li eutectic).[12] Thus, a reasonable estimate of the LiF-LiCl-LiBr/Li volumetric distribution coefficient would be $\sim$2. Using this value and accounting for the ratio of the lithium-to-salt densities ($\sim$4), the tritium concentration in lithium on a wppm basis will be approximately twice the concentration in the salt (assuming that equal volumes of salt and lithium are contacted). Therefore, the salt processing experiments performed in this study correspond to tritium extractions from lithium starting at about the 6-wppm level.

One possible difficulty in using the data from this study to predict the operation of a full-scale tritium extraction process is interference due to contaminants in the lithium. There is no doubt that a liquid-lithium fusion reactor blanket will accumulate quantities of carbon, nitrogen, and oxygen. Like hydrogen, these impurities will be partitioned between the liquid lithium and molten salt by the contacting step. In fact, molten-salt extraction may prove to be a reasonable means of removing these impurities from liquid lithium. This possibility is presently under consideration at ANL, where results of a preliminary study have indicated that interference of hydrogen extraction by other impurities is unlikely.

In the molten-salt extraction process, as applied to liquid-lithium fusion reactor blankets, it is assumed

1. that the lithium circuit will consist of a circulating lithium loop containing the reactor

blanket and the primary heat exchanger, and a small side stream for tritium recovery

2. that the tritium will be bred in the lithium blanket at a constant rate

3. that the rate of tritium recovery from the lithium will be directly proportional to the tritium concentration in the lithium.

Once the reactor has begun to operate, the tritium inventory in the lithium will begin to grow, and the tritium recovery rate will increase until it approaches the breeding rate. Equilibrium is established when the tritium inventory reaches the steady-state value. For a molten-salt extraction system in which equal volumes of salt and lithium are contacted, the relationship between the fraction of a lithium blanket that must be processed per unit time, X, and the steady-state tritium inventory, I_{ss}, is given by[12]

$$X = \frac{R_b}{I_{ss}} \cdot \frac{\epsilon D_v \eta + 1}{\epsilon D_v \eta} \ , \qquad (2)$$

where

R_b = tritium breeding rate

ϵ = efficiency of tritium recovery from the salt

D_v = volumetric distribution coefficient of tritium between the lithium and the salt

η = efficiency factor that accounts for non-equilibrium tritium distribution during contacting.

Using this equation and experimental values of D_v for several salts, Maroni et al.[12] concluded that a molten-salt extraction scheme was a feasible process and, as an example of its applicability, analyzed the tritium processing requirements for the Reference Theta-Pinch Reactor. In the analysis by Maroni et al., it was estimated that the tritium recovery efficiency from the salt would be $\sim$20%, with a current density of 1 A/m². For the experiments described herein, a recovery efficiency near 100% has been achieved. The average current density can be estimated from experiments that used a getter bed (such as in Fig. 4a) by dividing the integral of the current time curve by the area of the anode ($\sim$4 X 10^{-3} m²) and the time required for extraction. Note that both the initial hydride concentration and the recovery efficiency affect the current density. Thus, obtaining a recovery efficiency near 100% at an initial hydride concentration of 1 wppm in the salt requires almost 1 h of electrolysis at an average density of $\sim$8 A/m², while recovery of 90% of the hydrogen requires only 30 min, yielding a current density of $\sim$16 A/m². The current density of 1 wppm of tritium in lithium is estimated to be $\sim$1 A/m² at ϵ = 90%.

It is apparent from the experimentally determined recovery efficiencies that the molten-salt extraction process is even more favorable than originally proposed. In light of this finding, the analysis of the processing requirements presented in Ref. 12 has been reexamined using an efficiency of 90%. Results of this reexamination, given in Table I, show that the improved recovery efficiency leads to a reduction, by a factor of 2 to 4, in the fraction of lithium processed per unit time. This reduction, in turn, decreases the number of contacting units and the electrical power required for the processing and represents a significant decrease in the space and cost demands for the tritium recovery system.

An important trade-off exists between the contacting step and the salt processing step. The trade-off occurs between the recovery efficiency, which determines the number of contacting units, and the average current density, which dictates the volume of the electrolysis tank. With all other parameters fixed, the efficiency of the salt processing, ϵ, determines the number of contacting units required to maintain a given tritium steady-state inventory. On the other hand, the average current density decreases as the recovery efficiency increases, since the average current density is proportional to the tritium concentration. Therefore, the total electrode area and the size of the electrolysis tank must be large to extract the tritium at the lower current density and still recover tritium at a rate equal to the breeding rate. The salt processing step can be operated at high recovery efficiency and low current density or the recovery efficiency can be reduced to increase the average current density. It is believed that maximizing the recovery efficiency will be the preferred mode of operation, since the contacting units will be more complex devices than the salt processing tanks and the contacting operation will require substantially more electrical power.

The analysis in Table I gives a rough estimate of the processing requirements for a liquid-lithium fusion reactor blanket. It is difficult to estimate the actual requirements accurately, since neither the allowable tritium inventory, I_{ss}, nor the efficiency of the contacting operation, η, is known. Plans are already under way to determine the latter parameter with a multipurpose, 0.19-m^3 (50-gal) forced-circulating lithium processing test loop, currently being constructed at ANL. This loop will test the effectiveness of various methods of tritium and impurity control in lithium, including molten-salt extraction.[13] Attached to the loop will be a vessel designed to operate both as a mixer-settler for lithium salt contacting and as an electrochemical salt processing tank.

TABLE I

Analysis of the Molten-Salt Extraction Scheme for a Liquid-Lithium Blanket System

Tritium breeding rate (R_b)	= 60 g/h
Average lithium temperature	= 500°C
Extraction system temperature	= 500°C
Steady-state blanket inventories	
Lithium	= 8.0 × 10^8 g
Tritium (I_{ss})	$\begin{cases} = 0.425 \text{ kg for 13 nPa} \\ = 4.25 \text{ kg for 1300 nPa} \end{cases}$
Tritium recovery efficiency (ϵ)	= 90%
Capacity per extractor unit	= 23 m^3/h
Electrical power per extractor unit	= 3.73 kW

Tritium Partial Pressure (nPa)	Effective Distribution Coefficient ($D_l \cdot \eta$)	Fraction[a] Processed per Hour (X)	Number[b] of Extractor Units	Required Electrical Power (kW)
13	4.0	0.180	26	97
	2.0	0.220	32	119
	1.0	0.298	43	160
	0.5	0.455	66	246
1300	4.0	0.018	3	11
	2.0	0.022	4	15
	1.0	0.030	5	19
	0.5	0.046	7	26

[a]Fraction of the total lithium inventory that passes through the contactor network per hour.
[b]Number of units required in parallel for single-stage operation.

A detailed analysis of the molten-salt processing scheme must await more exact information on the allowable tritium inventory for a liquid-lithium fusion reactor blanket. This information will not be available until data from either large-scale test facilities or an actual fusion reactor are obtained. An important feature of the presently conceived molten-salt extraction process is that it appears to be applicable throughout the entire range of tritium concentrations that would be desired. No limiting behavior in the electrochemical processing technique was found down to the detectable limit of the experimental apparatus (corresponding to 0.06 wppm of tritium in lithium). As can be seen in Table I, the processing requirements are quite small at 5 to 0.5 wppm of tritium in lithium. They increase linearly as the tritium concentration decreases so that the processing requirements at 0.05 wppm are a factor of 10 higher than those given in Table I for 0.5 wppm. Furthermore, the molten-salt. extraction process lends itself to a modular design in which relatively small units are connected in parallel to the liquid-lithium blanket. This design allows additional flexibility for accommodating changes in the allowable tritium inventory of the blanket. If future safety regulations, economic constraints, or design difficulties require a reduction in the tritium inventory, additional processing units could be easily attached to meet the new requirements.

CONCLUSION

From this study it is concluded that hydrogen isotopes can be readily extracted from lithium halide molten salts saturated with lithium by electrolysis using an argon-sparged electrode. The hydrogen isotopes removed from the salt are recovered from the argon by a hot titanium getter bed. The electrochemical extraction technique that has been examined lends itself to incorporation into a molten-salt extraction process for tritium recovery from liquid-lithium fusion reactor blankets. The rate and efficiency of the electrochemical evolution are quite favorable and indicate that tritium extraction from liquid lithium by a molten-salt extraction process will be rate limited by the efficiency of the lithium salt contacting step rather than that of the salt processing step. Assuming that the distributions of tritium between lithium and different lithium halide salts are all similar, the molten salt that appears to be best suited for processing liquid-lithium fusion reactor blankets is LiF-LiCl-LiBr (22-31-47 mol%). A molten-salt extraction process that is based on this salt and that includes electrochemical processing is an attractive technique for recovering tritium from liquid-lithium fusion reactor blankets. It is estimated that with such a processing scheme tritium levels in

the blanket can be maintained at the low concentrations (<1 wppm) that are required by economic and safety constraints.

REFERENCES

1. F. L. RIBE, "Fusion Reactor Systems," *Rev. Mod. Phys.*, 47, 7 (1975).

2. R. W. CONN, "What is Past is Prologue: Future Directions in Tokamak Power Reactor Design Research," *Proc. 2nd Topl. Mtg. Technology of Controlled Nuclear Fusion*, September 21-23, 1976, Richland, Washington, CONF-760935, p. 539, U.S. Energy Research and Development Administration (1976).

3. V. A. MARONI, "Tritium Processing and Containment Technology for Fusion Reactors: Perspective and Status," *Proc. 2nd Topl. Mtg. Technology of Controlled Nuclear Fusion*, September 21-23, 1976, Richland, Washington, CONF-760935, p. 799, U.S. Energy Research and Development Administration (1976).

4. V. A. MARONI, "An Analysis of Tritium Distribution and Leakage Characteristics of Two Fusion Reactor References Designs," *Proc. 5th Symp. Engineering Problems of Fusion Research*, IEEE Pub. No. 73CH0843-3-NPS, November 6-9, 1973, p. 206, Princeton, New Jersey (1973).

5. J. DARVAS, "Tritium Technology in Fusion Devices," *Proc. Int. Conf. Radiation Effects and Tritium Technology for Fusion Reactors*, October 1-3, 1975, Gatlinburg, Tennessee, CONF-750989, p. III-1, U.S. Energy Research and Development Administration (1975).

6. V. A. MARONI, W. F. CALAWAY, E. VELECKIS, and R. M. YONCO, "Solution Behavior of Hydrogen Isotopes and Other Non-Metallic Elements in Liquid Lithium," *Proc. Int. Conf. Liquid Metal Technology in Energy Production*, May 3-6, 1976, Champion, Pennsylvania, CONF-760503, p. 437, U.S. Energy Research and Development Administration (1976).

7. E. VELECKIS, R. M. YONCO, and V. A. MARONI, "Solubility of Lithium Deuteride in Liquid Lithium," *J. Less-Common Met.*, 55, 85 (1977).

8. J. S. WATSON et al., "Study Session on Tritium," *Proc. Magnetic Fusion Energy Blanket and Shield Workshop*, March 29-April 2, 1976, Upton, New York, CONF-760343, Vol. I, p. 128, U.S. Energy Research and Development Administration (1976).

9. S. D. CLINTON et al., "Recent Experimental Studies Related to Controlled Thermonuclear Reactors," *Proc. Int. Conf. Radiation Effects and Tritium Technology for Fusion Reactors*, October 1-3, 1975, Gatlinburg, Tennessee, CONF-750989, p. III-519, U.S. Energy Research and Development Administration (1975).

10. J. S. WATSON, "An Evaluation of Methods for Recovering Tritium from the Blankets and Coolant Systems of Fusion Reactors," ORNL-TM-3794, Oak Ridge National Laboratory (1972).

11. J. L. ANDERSON, D. H. W. CARSTENS, and R. M. ALIRE, "CTR Related Tritium Research at LASL," *Proc. Int. Conf. Radiation Effects and Tritium Technology for Fusion Reactors*, October 1-3, 1975, Gatlinburg, Tennessee, CONF-750989, p. III-396, U.S. Energy Research and Development Administration (1975).

12. V. A. MARONI, R. D. WOLSON, and G. E. STAAHL, "Some Preliminary Considerations of a Molten Salt Extraction Process to Remove Tritium from Liquid Lithium Fusion Reactor Blankets," *Nucl. Technol.*, 25, 83 (1975).

13. W. F. CALAWAY, E. H. VAN DEVENTER, B. MISRA, C. J. WIERDAK, and V. A. MARONI, "Review of the ANL Program on Liquid Lithium Processing and Tritium Control Technology," *Proc. 2nd Topl. Mtg. Technology of Controlled Nuclear Fusion*, September 21-23, 1976, Richland, Washington, CONF-760935, p. 905, U.S. Energy Research and Development Administration (1976).

14. H. A. LAITINEN, W. S. FERGUSON, and R. O. OSTERYOUNG, "Preparation of Pure Fused Lithium Chloride-Potassium Chloride Eutectic Solvent," *J. Electrochem. Soc.*, 104, 516 (1957).

15. D. L. MARICLE and D. N. HUME, "A New Method of Preparing Hydroxide-Free Alkali Chloride Melts," *J. Electrochem. Soc.*, 107, 354 (1960).

16. P. A. NELSON et al., "High-Performance Batteries for Off-Peak Energy Storage and Electric-Vehicle Propulsion: Progress Report for the Period July-December 1975," ANL-76-9, p. 56, Argonne National Laboratory (1976).

17. J. A. PLAMBECK, J. P. ELDER, and H. A. LAITINEN, "Electrochemistry of the Lithium Hydride Cell," *J. Electrochem. Soc.*, 113, 931 (1966).

18. P. A. NELSON et al., "High-Performance Batteries for Off-Peak Energy Storage and Electric-Vehicle Propulsion: Progress Report for the Period January-March 1976," ANL-76-35, p. 42, Argonne National Laboratory (1976).

19. W. M. STACEY et al., "Fusion Power Program Quarterly Progress Report, October-December 1976," ANL/FPP-76-6, p. 61, Argonne National Laboratory (1976).

20. J. H. DeVAN, J. E. SELLE, and A. E. MORRIS, "Review of Lithium Iron-Base Alloy Corrosion Studies," ORNL/TM-4927, Oak Ridge National Laboratory (Jan. 1976).

21. R. R. HEINRICH, Argonne National Laboratory, Personal Communication (1977).

22. M. A. BREDIG, J. W. JOHNSON, and W. T. SMITH, "Miscibility of Liquid Metals with Salts: I. The Sodium-Sodium Halide System," *J. Am. Chem. Soc.*, 77, 307 (1955).

23. J. W. JOHNSON and M. A. BREDIG, "Miscibility of Metals with Salts in the Molten State: III. The Potassium-Potassium Halide System," *J. Phys. Chem.*, 62, 604 (1958).

24. C. H. LEMKE and L. B. DWORSKY, "The Solubility of Chloride Salts in Metallic Sodium and Lithium at 350-600°C," *Proc. Int. Symp. Molten Salts*, May 1976, Washington, D.C., p. 537 (1976).

25. J. E. SELLE, "Corrosion of Iron-Base Alloys by Lithium," *Proc. Int. Conf. Liquid Metal Technology in Energy Production*, May 3-6, 1976, Champion, Pennsylvania, CONF-760503, p. 453, U.S. Energy Research and Development Administration (1976).

26. J. W. KOGER, "Chromium Depletion and Void Formation in Fe-Ni-Cr Alloys During Molten Salt Corrosion and Related Processes," *Adv. Corrosion Sci. Technol.*, 4, 245 (1974).

27. P. A. NELSON et al., "High-Performance Batteries for Off-Peak Energy Storage and Electric-Vehicle Propulsion: Progress Report for the Period January-June 1974," ANL-8109, p. 63, Argonne National Laboratory (1975).

CORROSION AND MECHANICAL BEHAVIOR OF IRON IN LIQUID LITHIUM

T. A. WHIPPLE,* D. L. OLSON, W. L. BRADLEY,+
and D. K. MATLOCK *Colorado School of Mines*
Department of Metallurgical Engineering, Golden, Colorado 80401

The grain boundary of Armco Iron in liquid lithium, under the influence of steady-state creep, was investigated and showed a parabolic time dependence. An observed delay time for the grain boundary attack was correlated with the nucleation of a grain boundary corrosion product. The activation energies for creep and grain boundary penetration kinetics were found to be the same. Grain boundary penetration behavior under the influence of compressional stresses is the same as under the influence of tensile stresses, suggesting that plastic deformation controls the penetration kinetics regardless of the stress state that causes the plastic deformation.

INTRODUCTION

Early work by Popovich[1] reported that stress can enhance the liquid lithium corrosion of stainless steels. Jordan et al.[2] have investigated the effect low stresses have on the liquid lithium penetration of Armco Iron. They found that stresses as low as 12 MPa can cause a fifty-fold increase in the grain boundary penetration rate over that of unstressed specimens. The fact that such small stresses completely change the penetration behavior shows that static corrosion data could be very unreliable in the design of liquid lithium containment systems.

Figure 1 shows the stress dependence of the penetration distance at different times and temperatures.[2] The penetration, X, for these low stresses was found to be a function of time$^{1/3}$, which is the usual time dependence for primary creep. With this time dependence, the penetration rate coefficient, K, can be established as

$$X = (Kt)^{1/3} , \qquad (1)$$

and assuming

$$K = K_0 \exp(-Q/RT) , \qquad (2)$$

the activation energy can be obtained. This activation energy was found to be 74.3 kcal/mole, which is similar to the activation energy for creep in Armco Iron, namely, 73 kcal/mole (Ref. 3).

The magnitude of the stress, which had a definite influence on the penetration rate, was found to have no effect on the activation energy for penetration, but it did affect the pre-exponential term, K_0, in Eq. (2), thus increasing the penetration rate without changing the mechanism. Recently, Parkins et al.[4] suggested a mechanism for stress corrosion, where stress and temperature are only important indirectly. They state that the creep rate controls the corrosion rate. This model applied to the liquid lithium penetration of stressed Armco Iron would suggest that stress accelerates the grain boundary attack by creep strain breaking a protective corrosion product at the advancing interface. This exposes bare metal to the liquid lithium. To test the Parkins et al.[4] theory, Jordan et al. plotted total penetration versus total primary creep strain for a variety of stresses and temperatures and showed that penetration appeared to be a single valued function of creep strain.

It was the purpose of this investigation to expand and substantiate the relationship of creep to the lithium penetration behavior, by comparing penetration to creep strain, through carefully controlled creep tests performed with a wider range of stresses. Compression creep and penetration tests were performed to also assist in better defining the mechanism.
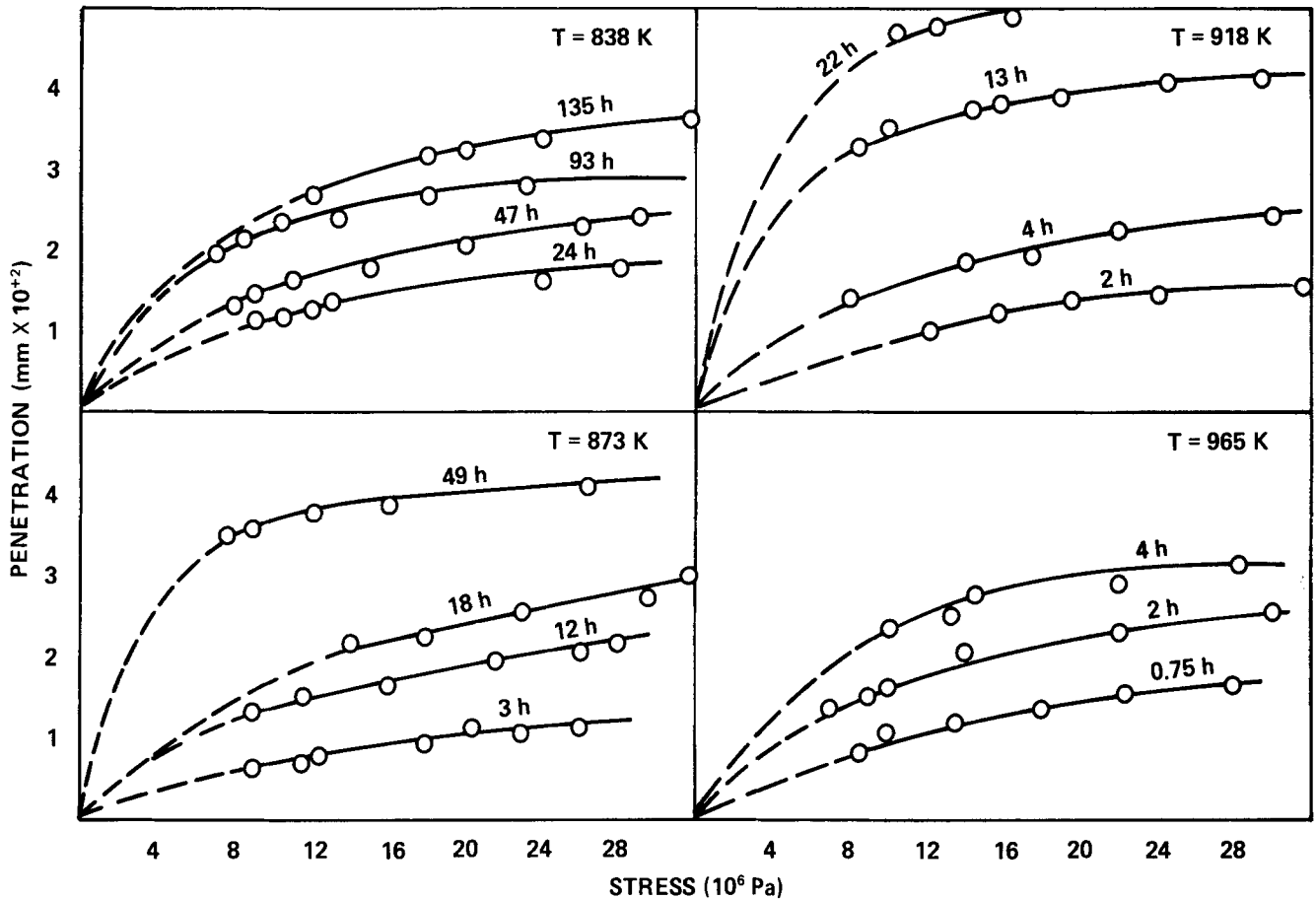
Fig. 1.   Lithium penetration into pure iron as a function of applied stress on the specimen for various times and temperatures (Ref. 2).

EXPERIMENTAL PROCEDURES

The lithium (99.9% pure) for this investigation was purchased from Research Organic-Inorganic Chemical Corporation in the form of 6.35-mm-diam, 300-mm-long rods. The lithium rods were shipped under mineral oil in stainless-steel containers. The as-received lithium was covered with a black scale, assumed to be lithium nitride. The oil and black scale were removed before charging into the test crucible.

Armco Electromagnetic Iron samples were purchased as 6.35-mm cold-drawn rods from Cory Steel Company. The maximum impurities in this iron are shown in Table I. Armco Iron was also used for the crucible construction and the loading cage assembly to guarantee that only pure iron was in contact with the lithium. The complete use of iron was to eliminate any dissimilar metal corrosion concerns.

All tests were conducted in a stainless-steel glove box. An inert atmosphere was maintained with 99.98% pure argon. To ensure that any leaks would result in an outflow of argon and no contamination, the atmosphere in the glove box was maintained at

TABLE I

Maximum Impurity Composition for the Armco Iron Specimens

Element	Maximum wt%
C	0.01
Mn	0.07
P	0.008
S	0.02
Si	0.02
Al	0.05
Ti	0.03

10 mm of water positive pressure differential. Entering argon was bubbled through a eutectic sodium-potassium alloy to remove any oxygen in the gas. The glove-box atmosphere was continually circulated through a high-temperature molten aluminum bubbler to remove oxygen and nitrogen contamination from the argon.

A schematic diagram of the crucible and furnace

arrangement is shown in Fig. 2. The furnace is designed with four 15.88-mm-diam rods for alignment of the crucible and loading assembly and to support load.

The liquid lithium was held approximately in the center of the hot zone of the furnace to minimize thermal gradients. The furnace was controlled by a Marshall model 4044 proportional controller, which provided a ±2 K temperature control. The sensing thermocouple was inserted in a hole in the crucible, ~10 mm below the liquid lithium bath, as shown in Fig. 2. The nitrogen content of the liquid lithium was above 3000 ppm.

Figure 2 also shows the loading cage assembly for testing with tensile stresses. The samples were threaded at both ends. The center bar that holds the top of the sample is held at a fixed level by being connected to the support rods of the furnace. The load is transmitted to the sample by the application of a weight to the cage. This weight is suspended from a plate under the furnace, which is connected to two 9.53-mm threaded rods on both sides of the furnace, which in turn are connected to the top plate of the cage. For compressive tests, this arrangement was reversed, the cage was held at a fixed level and 9.35-mm threaded rods, outside the furnace, were connected to the top plate of the center bar, thereby putting the sample in compression. Since the load was applied outside of the glove box, the pass-through rod was fitted with a balloon seal to prevent any reduction in the load due to friction.

Sample strain was continuously monitored using a Schaevitz model 500 HR linear variable differential transformer (LVDT). The LVDT was held stationary by connecting it to the bottom of the glove box. The core of the LVDT was connected to the plate under the furnace, thereby measuring the movement of the cage and the sample strain (see Fig. 2). This indirect method of measuring strain was necessary to minimize the effect of heat on the LVDT. The output of the LVDT was conditioned with a Schaevitz model CAS-025 signal conditioner and was continuously recorded with a Leeds and Northrup Speedomax 600 XL recorder.

The samples were machined from the 6.35-mm cold-drawn stock to the shapes shown in Fig. 3. The shorter gauge length was used for compression tests to prevent buckling. The samples were then vacuum annealed at 1123 K for 3 h. This resulted in an annealed grain size of 0.02 mm.

Lithium was placed in the crucible and heated to the test temperature. It was held at this temperature for at least 6 h to reach solubility equilibrium of the iron in lithium. Then the sample cage was placed in the lithium and the loading rods attached. After the setup had again achieved thermal equilibrium, after ~1 h, the signal conditioner and recorder were turned on and the load was applied. When the test was over,
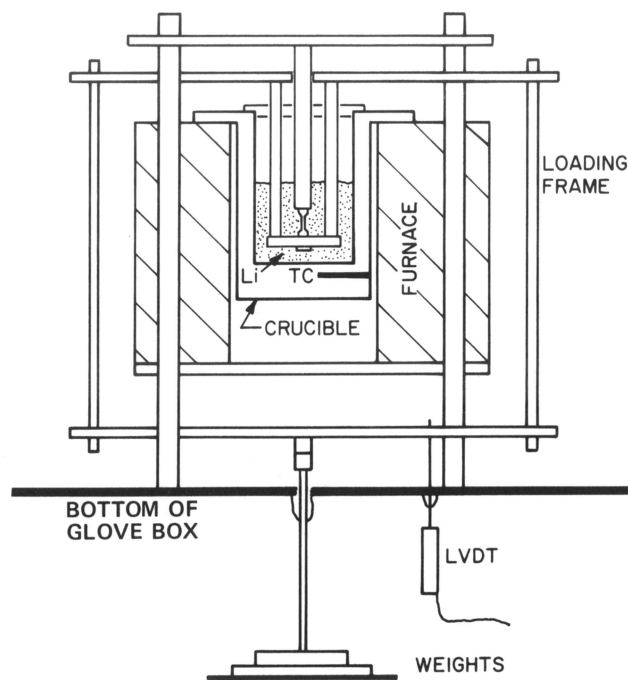
Fig. 2.   A schematic diagram of the test crucible and furnace arrangement used in this investigation.
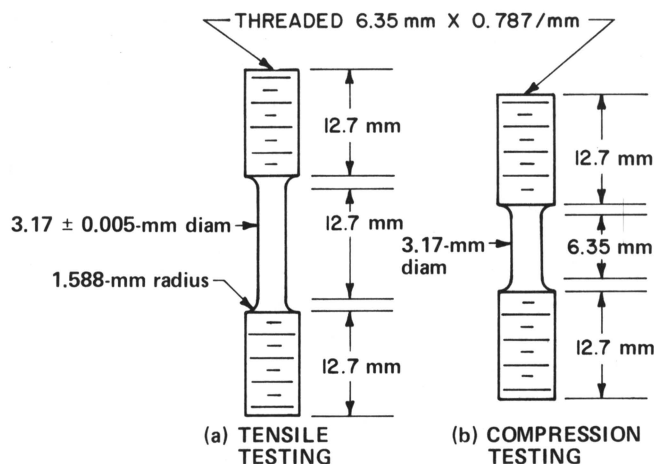
Fig. 3.   The sample geometries used for this investigation.

the load was removed and the sample was removed from the crucible.

Penetration of the sample was measured with optical metallography after removing the lithium by immersion in water, sectioning, polishing, and etching for 30 min in 8% H_3PO_4 in water.

RESULTS AND DISCUSSION

Creep strain and grain boundary penetration of Armco Iron in liquid lithium were measured for

selected temperatures and stresses. Penetration occurred only along grain boundaries, and every grain boundary was attacked approximately to the same depth.

Creep of Iron in Liquid Lithium

A typical creep curve for iron in liquid lithium is shown in Fig. 4. Most tests exhibited both primary and steady-state creep. The ones that did not were those that combined low temperature, low stress, and short times. These tests were stopped while still in primary creep and were used only for penetration data.

The temperature dependence of the steady-state creep rate was found by assuming that for creep of iron in liquid lithium, the common equation for a thermally activated creep process holds. This equation is

$$\dot{\epsilon} = A' \exp(-Q_c/RT) \ , \qquad (3)$$

where A' is a function of the stress and the structure of the iron. The activation energy, Q_c, was found by the use of the Arrhenius plots shown in Figs. 5 and 6, which are for constant stresses of 36 and 70 MPa. The activation energies are 78.2 and 74.6 kcal/mole, respectively. The average activation energy for all stresses was 75.8 kcal/mole. It is apparent that the activated process is not a function of the stress in the stress range investigated.

The stress dependence of the steady-state creep rate was found by using the following equation:

$$\dot{\epsilon} = A'' \sigma^n \ , \qquad (4)$$

where A'' is a function of the temperature. This equation assumes that the activation energy, Q_c, is not a function of the stress, as was shown previously. In Fig. 7, log creep rate is shown as a function of log stress at 883 K. The slope of this line, 4.9, is the stress exponent, n, in Eq. (4). Similar plots for 858 and 908 K gave values of 5.0 and 4.9, respectively, giving an average of 4.9. This value is very close to the accepted value for a stress exponent in creep, which is 5.0, and it should not vary much over the relatively small range of temperatures tested.

The temperature and stress dependence of the steady-state creep rate were combined into an equation of the form

$$\dot{\epsilon} = A\sigma^n \exp(-Q_c/RT) \ . \qquad (5)$$

By substituting in the activation energy, 75.8 kcal/mole, and the stress exponent, 4.9, the constant, A, can be evaluated, and the equation for the steady-state creep rate of Armco Iron in the liquid lithium is

$$\dot{\epsilon} = 3.98 \times 10^7 \, \sigma^{4.9} \exp(-75\ 800/RT) \ , \qquad (6)$$

with stress expressed in MPa, temperature in K, and $\dot{\epsilon}$ in h^{-1}.
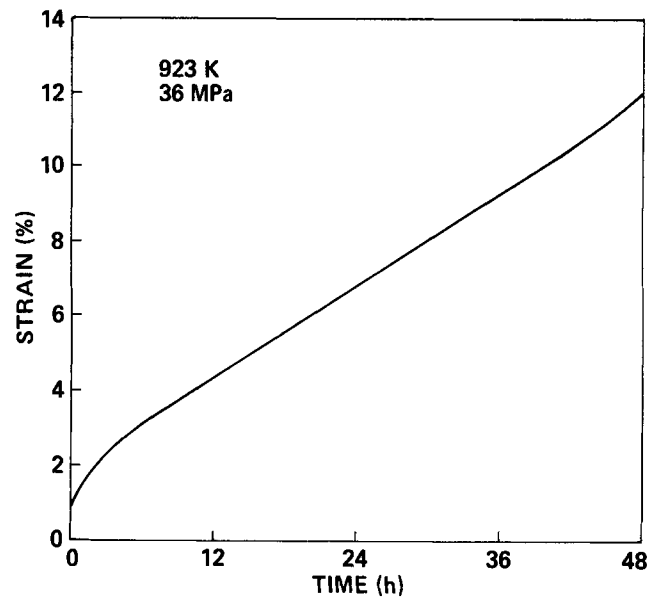
Fig. 4. The strain versus time curve for a sample tested at 923 K and a stress of 36 MPa.

The activation energy of 75.8 kcal/mole for creep of Armco Iron in lithium is close to the activation energy reported for creep of α-iron in air, namely, 73 kcal/mole (Ref. 3). This shows that the liquid lithium environment has little or no effect on the creep mechanism. The slightly higher activation energy in lithium could be attributed to the fact that the grain boundary penetration of the lithium causes a reduction in load carrying area and therefore a faster creep rate. This effect would be more pronounced at higher temperatures, since the penetration rate is greater, and would result in a higher activation energy for creep.

Creep in Compression

A limited number of creep tests were performed at 883 K and 36 MPa with the sample under compressive, rather than tensile, stresses. These tests were run to investigate the possibility that the increased penetration under stress might be due to a surface deformation mechanism, rather than a pulling apart of a corrosion product under the influence of tensile stresses. The surface deformation mechanism, the arrival of dislocations at the surface, would be the same in compression as in tension. Since a compressive constant load creep test shows a constantly decreasing creep rate, the steady-state creep rate for these tests was evaluated at a creep strain that was found to be in secondary creep by a test at the same temperature and stress in tension. The compressional creep rates were found to be essentially the same (within a factor of 2) as the creep rates for the same stress temperature in tension.
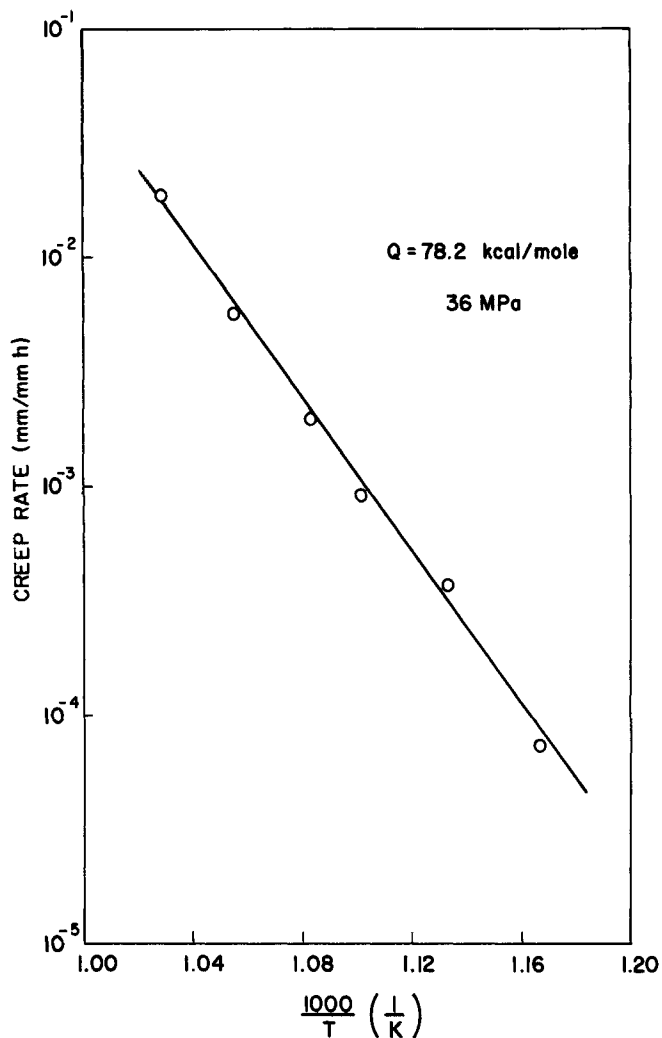
Fig. 5. The temperature dependence of the creep rate of pure iron in liquid lithium at a stress of 36 MPa.
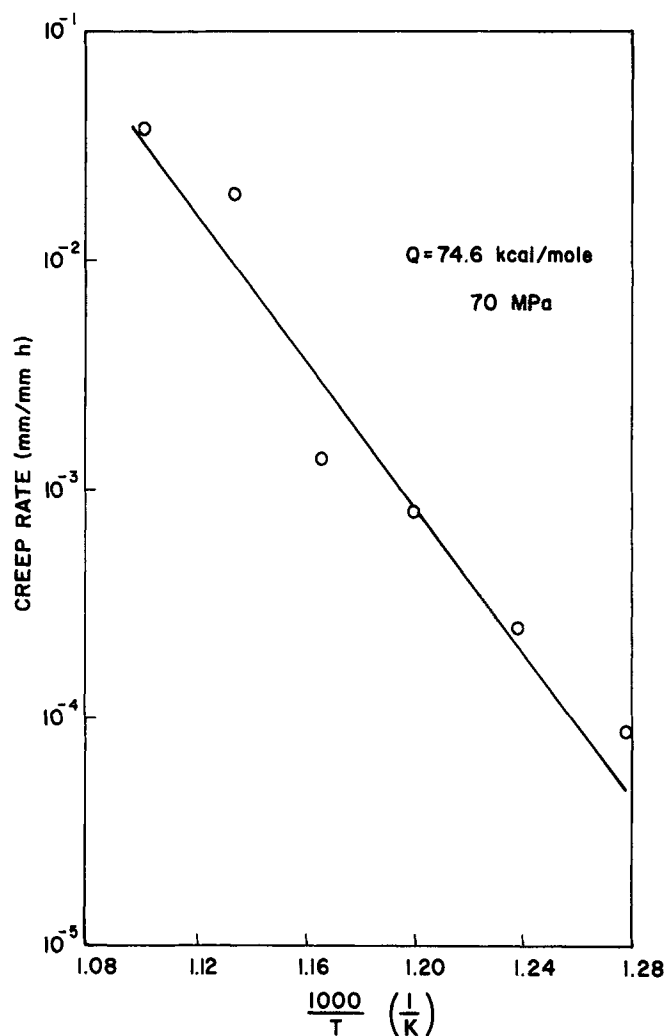
Fig. 6. The temperature dependence of the creep rate of pure iron in liquid lithium at a stress of 70 MPa.

Penetration

Jordan et al.[2] found the following equation for the stress enhanced lithium penetration of Armco Iron during primary creep:

$$X = [(K_0 t) \exp(-74\,300/RT)]^{1/3} , \qquad (7)$$

where K_0 is a function of the applied stress. If the stress and temperature are held constant, then

$$X = A t^{1/3} . \qquad (8)$$

They related this $t^{1/3}$ dependence to the fact that primary creep usually has a cube root of time dependence. However, in the current investigation higher stresses were used, and primary creep was usually only a small portion of the test. For this case, it was assumed that penetration still had the simple power relationship:

$$X = (Kt)^a . \qquad (9)$$

A log penetration versus log time plot was made to determine this time dependence (see Fig. 8), and a was found to be 0.53. This shows that penetration is proportional to the square root of time. It is interesting to note that when in primary creep, grain boundary penetration has the same time dependence as creep, $t^{1/3}$, but when the creep rate is a single-valued function of time, as in secondary creep, the grain boundary penetration time dependence returns to the same parabolic time dependence found in static liquid lithium corrosion tests.[5,6]

Figures 9 and 10 show the penetration depth versus the square root of time at the different temperatures. Note that in each case, if the line is extended to zero penetration, it intersects the axis at a finite time; this is considered to be the delay time before penetration begins. In Fig. 11, the delay time is shown as a function of temperature. This figure shows a C-shaped curve, which is commonly observed in nucleation kinetics. The curve also appears to show

Fig. 7.   The stress dependence of the creep rate of pure iron
in liquid lithium at 883 K.

Fig. 8.   Determination of the time dependence of the grain
boundary penetration of stressed pure iron.

$$K = K'_0 \exp(-Q_p/RT) \ , \tag{11}$$

the activation energy, Q_p, can be established from an Arrhenius plot (Fig. 12). The activation energy was found to be 72.8 kcal/mole.

The fact that the activation energies for creep, 75.8 kcal/mole, and penetration, 72.8 kcal/mole, are similar suggests that the two processes have the same controlling mechanism. Figure 13 is a plot of log penetration rate coefficient versus log creep rate showing a slope of 0.98, demonstrating that the penetration rate coefficient is a single-valued function of the creep rate

$$K = B\dot{\epsilon} \ , \tag{12}$$

and B was found to be 1.26. Now the total penetration equation can be written by substituting in Eq. (12) for the creep rate and combining with Eq. (9):

$$X = [5.01 \times 10^7 \ \sigma^{4.9} t \ \exp(-75 \ 800/RT)]^{1/2} \ , \tag{13}$$

where stress is expressed in MPa, time in h, and temperature in K. This equation is important in that it relates the grain boundary penetration distance to the temperature, exposure time, and applied stress. A relationship of this type would be extremely useful in the design of liquid-metal containment systems. It is important to note that the penetration is a strong function of the applied stress, σ. For design applications, this dependence means that any reduction in load will greatly improve the corrosion resistance.

Since the activation energy for the creep rate of Armco Iron in lithium is close to the reported value in air, it is concluded that the creep rate controls the penetration rate. This lends support to the stress sorption theory for stress corrosion, which states that dislocation pileups at the grain surface or grain boundary would create preferred sites for adsorption of the liquid metal. The number of dislocations

a double nose. It is possible that this is due to the change in equilibrium at 923 K reported by Popovich[7] for the reaction

$$2Li + 2Fe_3C = Li_2C_2 + 6Fe \ . \tag{10}$$

Above 923 K, Fe_3C is more stable and below 923 K, Li_2C_2 is more stable. Therefore, Fig. 11 may be showing the nucleation of two different corrosion products. Other corrosion products such as $Li_3N \cdot FeN$ have been suggested for iron in nitrogen contaminated liquid lithium.[8]

By finding the slopes of the lines in Figs. 9 and 10, the penetration rate coefficients, K, can be established. Assuming that penetration is a thermally activated process and fits an equation of the form

Fig. 9. Lithium penetration of the grain boundary of stressed pure iron as a function of time$^{1/2}$ for the three temperatures of 858, 883, and 908 K.
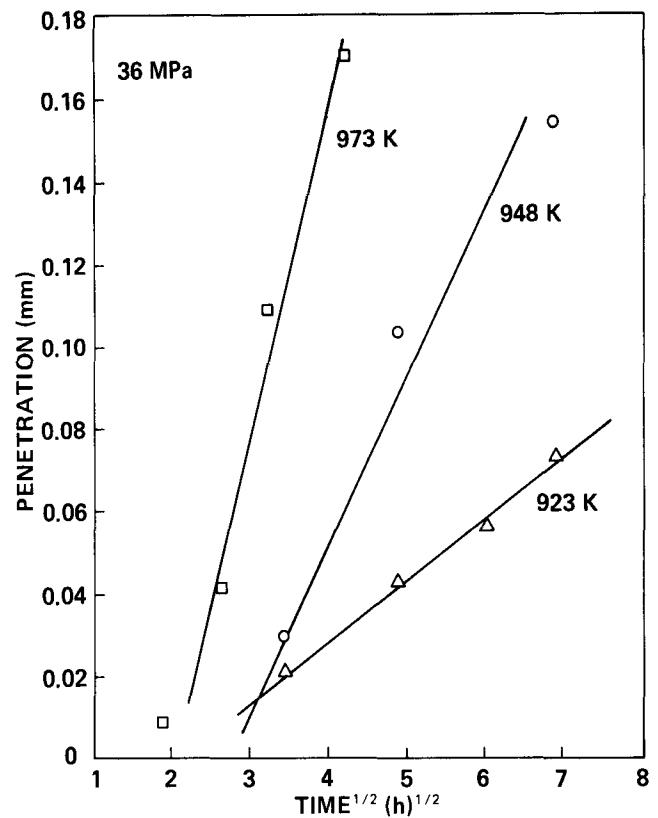
Fig. 10. Lithium penetration of the grain boundary of stressed pure iron as a function of time$^{1/2}$ for the three temperatures of 923, 948, and 973 K.

arriving at the surface would control the amount of adsorption. Therefore, the corrosion rate would be dependent on the creep rate. This model cannot, however, totally explain the stress corrosion of Armco Iron in liquid lithium.

The stress sorption theory does not take into account the effect a corrosion product would have on the mechanism. If the corrosion rate is dependent on the creep rate alone, the higher creep rate in primary creep would cause a larg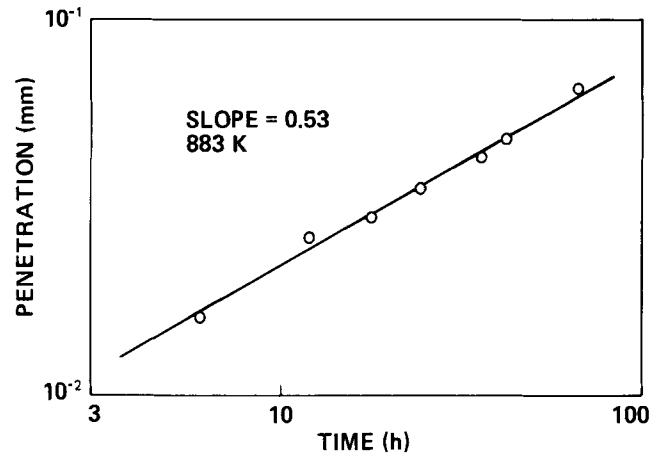er initial corrosion rate. Therefore, the apparent delay time for corrosion would be negative. The observance of a positive delay time in this investigation was related to the nucleation of a corrosion product. This suggests that a more complex mechanism must be involved. This mechanism is related to the arrival of dislocations at the surface of grains or at grain boundaries where a corrosion product exists. The plastic flow would break up the corrosion product and also provide preferred reaction sites for the chemical corrosion. This mechanism would prevent the lithium from embrittling the iron as in the original stress sorption theory, because the lithium does not diffuse into the iron and lower the bond energy. The mechanism would also still allow for a creep rate dependence after the corrosion product has been nucleated.
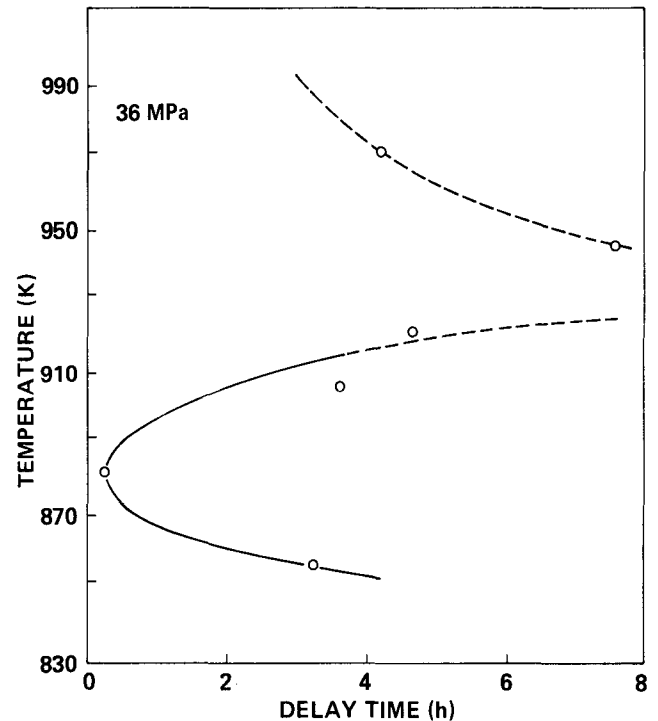
Fig. 11. The delay time for the penetration of the stressed pure iron as a function of temperature at a stress of 36 MPa.
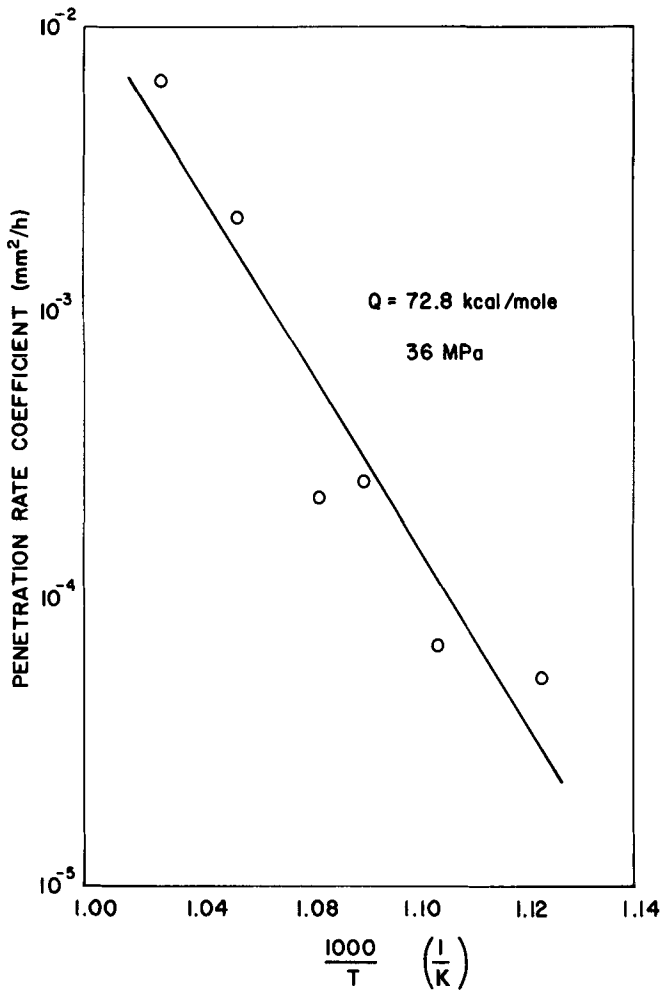
Fig. 12. The temperature dependence of the grain boundary penetration rate coefficient of stressed pure iron in liquid lithium at a stress of 36 MPa.

Fig. 13. The log grain boundary penetration rate coefficient versus log creep rate at a stress of 36 MPa.
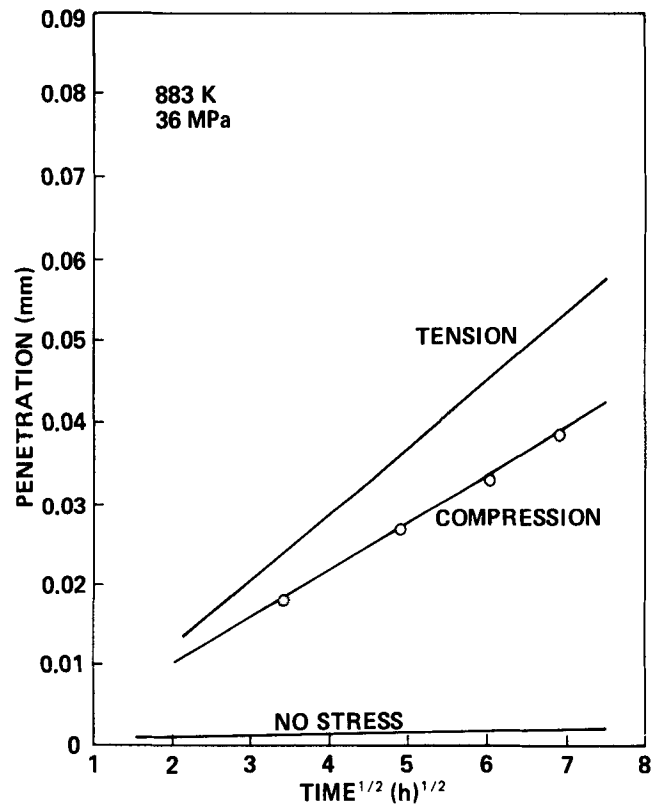
Fig. 14. A comparison of the lithium grain boundary penetration in tension, compression, and no stress test conditions as a function of the square root of time at 883 K and 36 MPa. Data for the tension line are presented in Fig. 9.

Penetration Under Compressive Stresses

If plastic flow does, in fact, increase the corrosion rate by breaking up the corrosion product and providing preferred sites for chemical action, it should not matter whether the plastic flow is caused by tensile or compressive stresses. To test this theory, the penetration was measured as a function of time at 883 K and a compressive stress of 36 MPa. The results are shown in Fig. 14. The total penetration and the penetration rate were found to be slightly lower, but still much greater than an unstressed sample. The delay time was unchanged, indicating that the same nucleation process was at work. This lower total penetration and penetration rate can be explained by considering, in conjunction with Eq. (13), the effects of the variations in true stress that occur in constant load creep tests. Due to dimensional changes, the true stress, in tension, increases with strain in a constant load creep test. Conversely, the true compressive stress decreases with strain. Equation (13) indicates that the penetra-

tion behavior is very stress sensitive, and thus the observed differences in penetration behavior shown in Fig. 14 simply reflect slight true stress variations between the two tests, since all of the data reported here were obtained from constant load creep tests.

This observation further supports the contention that corrosion depends directly on deformation, whether it be in tension or compression. There was some question as to the possibility that the penetration of compression specimens was caused by secondary tensile stresses set up by the barreling of the sample. This possibility was eliminated when the sample was sectioned through a buckled region that was definitely under a high compressive load and large penetrations were still observed.

CONCLUSIONS

The most important facts this investigation revealed are:

1. The grain boundary penetration of Armco Iron in liquid lithium, under the influence of steady-state creep, shows a parabolic time dependence with the penetration proportional to $t^{1/2}$.

2. A delay time is observed before the preferential grain boundary attack begins. This delay time was correlated with the nucleation of a corrosion product.

3. The activation energies for creep and grain boundary penetration kinetics were shown to be the same, suggesting that the creep rate controls the penetration rate.

4. Grain boundary penetration behavior under the influence of compressional stresses is the same as under the influence of tensile stresses, suggesting that plastic deformation controls the penetration behavior regardless of the stress state that causes the plastic deformation.

REFERENCES

1. V. V. POPOVICH, *Fiz. Khim Mekh. Mat.*, 5, 444 (1969).

2. W. JORDAN, W. L. BRADLEY, and D. L. OLSON, "Liquid Lithium Penetration of Stressed Armco Iron," *Nucl. Technol.*, 29, 209 (1976).

3. J. E. DORN, *Creep and Recovery*, p. 274, American Society for Metals, Metals Park, Ohio (1957).

4. R. N. PARKINS et al., "Role of Stress in the Stress Corrosion Cracking of Mg-Al Alloy," *Corrosion*, 29, 6, 251 (1973).

5. R. A. PATTERSON, R. J. SCHLAGER, and D. L. OLSON, *Nucl. Mater.*, 57, 312 (1975).

6. J. A. REEVES, Jr., D. L. OLSON, and W. L. BRADLEY, "Grain Boundary Penetration Kinetics of Nitrided Type 304L Stainless Steels," *Nucl. Technol.*, 30, 385 (1976).

7. V. V. POPOVICH, *Fiz. Khim Mekh. Mat.*, 6, 282 (1970).

8. E. E. HOFFMAN, ORNL-2924, Oak Ridge National Laboratory (1960).

EUROPIA AS A NUCLEAR CONTROL MATERIAL

PAUL C. S. WU *Westinghouse Advanced Reactors Division Box 158, Madison, Pennsylvania 15663*

The physical and nuclear properties of Eu_2O_3 were reviewed, evaluated, and compared with those of the other potential control materials for breeder reactors. Europia with a 90% theoretical density has approximately the same amount of europium atoms per unit volume as the pure metal. Consequently, the reactivity worth per unit volume of Eu_2O_3 is similar to that of pure metal. In addition, the reactivity of Eu_2O_3 is superior to tantalum and is comparable to natural B_4C. The decay heat of Eu_2O_3 is much lower than that of tantalum over the range of decay times that is of interest with respect to handling. Irradiation-induced swelling of Eu_2O_3 is lower than that of B_4C, and postirradiation examination revealed only ~1% dimensional changes in the thermal- and/or fast-neutron spectrum (8×10^{25} n/m^2). Although surface reaction between Eu_2O_3 and the fast test reactor reference cladding Type 316 stainless steel leads to the formation of a europium silicate, it is expected that Eu_2O_3 would be compatible with low-silicon Type 316 stainless steel. In addition, the Eu_2O_3-sodium system was also shown to be compatible under simulated liquid-metal fast breeder reactor conditions without significant change. Consequently, Eu_2O_3 is an excellent alternate candidate compared to B_4C as the neutron absorber for fast breeder reactors.

INTRODUCTION

The high operating temperatures and neutron fluxes in sodium-cooled fast breeder reactors (LMFBRs) have imposed very stringent requirements on the control rod materials to ensure safe, effective, and reliable operation. The main requirements are

1. large neutron capture cross sections, so that the neutron flux in a reactor can be controlled effectively

2. high resistance to radiation damage, which frequently manifests itself in undesirable changes in shape, dimensions, structure, and properties of the materials under irradiation

3. compatibility with the cladding alloy and the coolant, to ensure a reliable operation

The materials under consideration for control rods in LMFBRs are boron carbide (B_4C), pure tantalum, tantalum—10% tungsten (Ta—10% W), and rare-earth-based materials. Although B_4C has been widely used in thermal reactors and is currently the reference material for the control rods in the Fast Flux Test Facility (FFTF), there are various problems associated with its application, especially the large amount of helium gas release due to neutron irradiation and its compatibility with the cladding alloy, stainless steel.[1-3] The disadvantage with tantalum is that it releases a considerable amount of decay heat, which will introduce handling and operational difficulties. In addition, information currently available also seems to show that tantalum will swell during irradiation due to the formation and growth of voids.[4-7] Lanthanon materials absorb neutrons mainly by an (n,γ) reaction and are thus free of problems associated with gas evolution, particularly helium and radioactive tritium under irradiation. The purpose of the present task is to review the properties of potential europium absorber materials, particularly Eu_2O_3. Properties of interest include reactivity worth, resistance to radiation damage, and compatibility with stainless steel and the primary coolant, sodium. In addition, fabrication and properties of rare-earth oxides/stainless-steel dispersoid neutron absorbers are also reviewed.

EUROPIUM AS A NEUTRON ABSORBER

It was reported[8-11] that samarium, europium, gadolinium, and dysprosium all have properties that make them attractive neutron absorbers. However, europium with its unique nuclear properties is considered to be one of the best. The reasons for this will become obvious after we compare the nuclear properties of europium with those of the other potential neutron absorbers.

The decay and neutron capture sequences of the isotopes of samarium, gadolinium, dysprosium, and europium were previously reported.[8-10] It is noted in Table I that europium has a number of isotopes that have large neutron capture cross sections. In addition, all of the europium isotopes, formed from naturally occurring europium by neutron capture, decay to gadolinium, which also has large neutron capture cross section. Another major advantage of europium is that the isotopes have fairly long half-lives, which results in a very long useful service life. This effect was reported by Stevens[11] and is illustrated in Fig. 1. It shows the variation of thermal-neutron absorption cross section of natural europium as a function of the number of neutrons absorbed per initial europium atom. It is noted that the cross section remains high after the absorption of one neutron per initial europium atom. The main reason for this phenomenon is primarily due to the retention and growth of the 420-b ^{152}Eu combined with the generation of the 1500-b ^{154}Eu and 14 000-b ^{155}Eu, as shown in Table I. Consequently, the effective life-time of europium-bearing control rods can be appreciable. Although these results were obtained mainly in thermal systems, it is likely that europium may behave similarly in a fast-neutron spectrum.

The relative worths and cross sections of all potential neutron absorbers for a fast reactor were compared,[8] and it was concluded, based on the limited information reported in the literature, that europium, tantalum, rhenium, and silver all possess attractive nuclear worth relative to B_4C at practical levels of enrichment. However, tantalum releases considerable decay heat, which causes handling and operational difficulties; rhenium is economically unfeasible at the present time; and silver has a low melting point relative to its required service temperature. Consequently, europium, with its high melting point and attractive nuclear properties, discussed in detail in the subsequent section, is considered the most promising alternative fast reactor neutron absorber.

Due to the extremely reactive nature of europium with oxygen and moisture the more stable sesquioxide, Eu_2O_3, in the form of either a vibratory packed powder, pressed and sintered pellets, or as dispersed particles in metallic matrices, has been used to fabricate reactor control devices.

TABLE I

The Decay and Neutron Capture Schemes of
Europium Isotopes

Isotope	Thermal Cross Section or Abundance	Half-Life	
^{151}Eu	(47.8%)	Stable	
n	(9000 b)		
^{152}Eu	β^-	(9.2 h)	^{152}Gd
n	(5000 b)		
^{153}Eu	(52.2%)	Stable	
n	(420 b)		
^{154}Eu	β^-	(16 yr)	^{154}Gd
n	(1500 b)		
^{155}Eu	β^-	(1.7 yr)	^{155}Gd
n	(14 000 b)		
^{156}Eu	β^-	(15.4 days)	^{156}Gd
n (?)			
^{157}Eu	β^-	(15.4 h)	^{157}Gd

Europium in the metallic state and in many of its compounds is divalent; only in a few compounds is it trivalent. In Table II, the properties of selected europium compounds[12,13] are given. It is seen that the volume decrease due to decay to gadolinium is ~20% for the divalent europium compounds, whereas there is only ~1% volume change in the case of trivalent compounds. This is because the Eu^{+2} has an ionic radius of 11.2 nm (1.12 Å), while Gd^{+3} has an ionic radius of 10.2 nm (1.02 Å). On the other hand, the ionic radius of Eu^{+3} is about the same as that of Gd^{+3}. Therefore, when the divalent europium being used as a control rod material decays to gadolinium, the control rods undergo a large volume contraction, which may cause significant operational difficulties. In Table II, one finds very few compounds in which europium is trivalent. Among these, the intermetallics are chemically very active, while halides and sulfides normally have low melting points. Therefore, Eu_2O_3, with its high melting point and thermodynamic stability, is the most attractive candidate as a neutron

absorber. Europium nitride (EuN) has a density higher than that of Eu_2O_3, and it also has a fairly high melting point and thermal stability. However, since it reacts rapidly in air to form oxide, it would not be a good choice as a neutron absorber.

Europium borides, like boron carbide, have the problem of helium release during irradiation. Radiation damage of EuB_6 and other selected borides was investigated by Cummings[14] with integrated thermal-

Fig. 1. Variation of the neutron absorption cross section of natural europium with absorption of neutrons.

neutron exposures of 1.4×10^{19} to 7.9×10^{20} n/cm^2 at temperatures above 100°C. The large amount of helium release from EuB_6 makes it very undesirable as a control material. Consequently, Eu_2O_3 remains the most attractive europium compound.

PROPERTIES OF EUROPIUM SESQUIOXIDE, Eu_2O_3

Europium sesquioxide, Eu_2O_3, like its parent metal, is hygroscopic, and its chemical and physical properties are not yet completely characterized. In Fig. 2, the heats of formation of rare-earth sesquioxides are plotted from the results given by Gschneidner.[15] It is clear that both europium and ytterbium sesquioxides have values much smaller than those of the other rare earths. This is especially true in the case of europium. This peculiarity is attributed again to the electronic structures of the lanthanons. Europium and ytterbium, with seven and fourteen 4f electrons, respectively, are also stable in the divalent state; consequently, their trivalent oxides are not as stable as those of the other lanthanon sesquioxides. In Table III, the structures and properties of Eu_2O_3 are briefly summarized.[9] In addition, the structure and properties of B_4C, the reference control material for the fast test reactor (FTR) and the Clinch River Breeder Reactor Plant (CRBRP), are also included

TABLE II

Selected Properties of Europium Compounds

Group	Element	Compound	Crystal Structure	Lattice Constant, Å			Valence	Volume Decrease Due to Decay to Gadolinium, %
				a_0	b_0	c_0		
IA	H	EuH_2	Ortho.				2.4	11.2
IIA	Be	$EuBe_{13}$					3	~1.0
IIIA	B	EuB_6	Cubic	4.174			2.7	5.5
	Al	$EuAl_2$	Cubic	8.125			2.6	8.3
IVA	C	EuC_2	Hex.	4.045		6.645	2.0	20.4
		$EuSi_2$	Hex.	4.29		13.66	2.5	9.0
VA	N	EuN	Cubic	5.014			3.0	0.66
VIA	O	EuO	Cubic	5.141			2.3	~14
		Eu_2O_3	Cubic	10.865			3.0	1.41
		Eu_2O_3	Mono.	13.944	3.581	8.676	3.0	
	S	EuS	Cubic	5.968			2.0	20.1
		Eu_3S_4	Cubic	8.539			2.6	~7.0
		Eu_2S_3	Cubic	8.415			3.0	0.99
		EuS_2	Tet.	7.86		8.03	3.0	1.01
	Te	$EuTe$	Cubic	6.585			2.0	21.0
	Se	$EuSe$	Cubic	6.185			2.0	20.6
	Cu	$EuCu_2$					2.2	14.8
VIII								

for comparison. Eu_2O_3 has two crystal forms: the low-temperature body-centered cubic (bcc) form and the monoclinic high-temperature modification. The transformation temperature has been given in the range from 1075 to 1100°C or 1300 to 1400°C
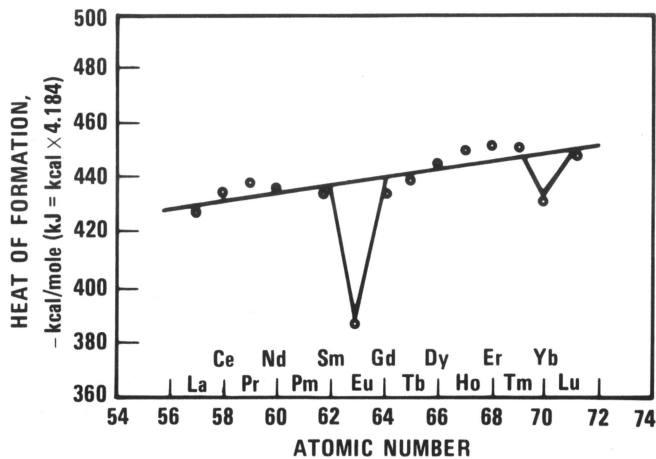
Fig. 2.   Heats of formation of the lanthanide sesquioxide.

(Ref. 13). In either case, the transformation temperature is within the operation temperature range, 1000 to 1500°C (1800 to 2800°F), for the control rods in LMFBRs. Therefore, the bcc Eu_2O_3 is not desirable due to the allotropic transformation. Since the monoclinic Eu_2O_3 has a density that is ~12% higher than that of the cubic modification, the nuclear worth of the monoclinic Eu_2O_3 would be greater. In addition, Roth and Schneider reported that the allotropic transformation is irreversible[13]; that is, once the monoclinic Eu_2O_3 formed, it remains the same structure at temperatures below the transformation point. This work is supported by the results of Ignateva and Bamburov[16] and Ross et al.[17] Consequently, no operational difficulties arising from volume change induced by allotropic transformation would be anticipated for monoclinic Eu_2O_3.

NUCLEAR PROPERTIES AND RADIATION RESISTANCE OF EUROPIUM SESQUIOXIDE, Eu_2O_3

The nuclear properties of europium were generally discussed in an earlier section. The important

TABLE III

Comparison of Structure and Properties of Eu_2O_3 and B_4C

Structure or Property	Eu_2O_3		B_4C
	Form I	Form II	
Structure type	Body-centered cubic	Monoclinic	Rhomobohedral
Lattice parameter, Å	$a_0 = 10.866$	$a_0 = 14.1133$ $b_0 = 3.6025$ $c_0 = 8.8080$ $\beta = 100.026$ deg	$a_R = 5.167$ $\alpha_R = 65.60$ deg
Theoretical density, g/cm^3	7.287	7.951	2.51
Absorber cation density, $atom/cm^3$	2.49×10^{22}	2.72×10^{22}	2.17×10^{22}
Free energy of formation, kcal/mole			
at 25°C	−374	−372	−12.55 (527°C)
at 727°C	−322.7	−322	−8.68 (2227°C)
Melting point, °C		~2300	2350-2500
Specific heat, $cal \cdot mole^{-1} (°C)^{-1}$			
0 to 800°C		33.3	16.6 (260°C)
Linear coefficient of thermal expansion, $(°C)^{-1}$			
30 to 840°C		10.5×10^{-6}	4.5×10^{-6} (25-800°C)
0 to 1000°C		10.35×10^{-6}	5.54×10^{-6} (25-1000°C)
0 to 1200°C		10.3×10^{-6}	6.02×10^{-6} (25-1500°C)
Thermal conductivity, $W \cdot m^{-1} (°C)^{-1}$			
at 25°C		3.42	33.5 (25°C)
at 1000°C		2.38	12.6 (800°C)
Young's modulus, psi at 25°C		4.5×10^6	65×10^6
Transformation rate			
at 1100°C	Several days		
at 1300°C	<1 h		

feature observed is that the naturally occurring europium isotopes, ^{151}Eu and ^{153}Eu, upon neutron capture transmute to ^{152}Eu and ^{154}Eu, respectively. These two isotopes also have large neutron capture cross sections. The nuclear properties of Eu_2O_3 are very close to those of europium metal. The reactivity worth of Eu_2O_3 is similar to that of the pure metal because the number of europium atoms per unit volume of the metal and an oxide with 90% theoretical density are approximately equal, due to the greater density of the oxide. Unfortunately, the cross sections of europium and its isotopes for fast neutrons are not well known.

Information on the activity of Eu_2O_3 after irradiation is very limited.[8] In general, decay heating in absorber materials stems from the absorption of radiation emitted during radioactive decay. The relative decay energy of Eu_2O_3 with respect to that of tantalum as a function of decay time was reported by Spenke[18] and is shown in Fig. 3. It is found that
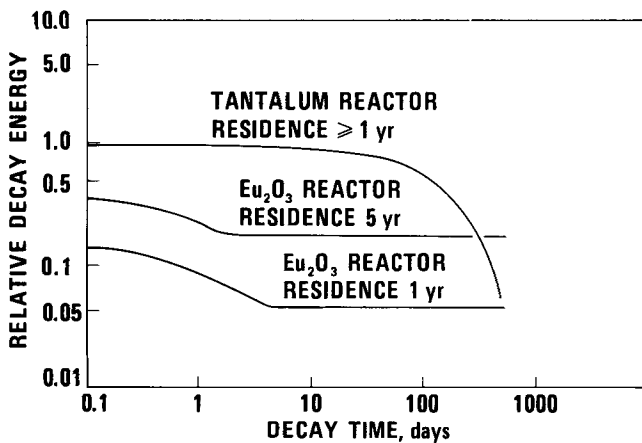
in the case of tantalum, the amount of decay heat is sufficient to require efficient forced convection cooling of the control rods after service. Note in this figure that the decay heat rates indicated for Eu_2O_3 are a factor of 10 lower than those for tantalum after a residence time of 1 yr and a factor of 5 lower than tantalum after a 5-yr residence time.

The activity values for tantalum, B_4C, and Eu_2O_3 obtained in the SNEAK core 6A and the physical properties reported in literature for these materials were summarized by Spenke[18] and are shown in Table IV. It is interesting to note that the reactivity value of Eu_2O_3 is ~30% higher than that of natural B_4C. From such data, unpublished calculations[19] have shown that a high-density Eu_2O_3 control rod would be comparable to a 40% enriched B_4C rod in terms of cost and reactivity worth.

IRRADIATION BEHAVIOR

The radiation resistance of the rare-earth oxides Eu_2O_3, Sm_2O_3, Gd_2O_3, and Dy_2O_3 was studied by Goltsev et al.[20] These compounds were irradiated to a total fluence of ~1 X 10^{22} n/cm². The thermal flux was 5 X 10^{14} n/cm²·s, while the fast-neutron flux ($E > 0.18$ MeV) was 1 X 10^{14} n/cm²·s. The surface temperatures of the specimens were in the range from 350 to 600°C, depending on their composition and location in the core. Density changes in the specimens resulting from the irradiation show that Eu_2O_3 has the least volume change (~1%). They also reported that the macro- and microstructures of all the specimens were practically unaffected by irradiation. The x-ray results also revealed that the monoclinic Sm_2O_3 and Gd_2O_3 become amorphous, while cubic structure of Dy_2O_3 was unaffected by the irradiation. Unfortunately, the structural stability of Eu_2O_3 was not discussed. X-ray diffraction studies of neutron irradiated Eu_2O_3 were also carried out by Cummings[14] with an integrated thermal-neutron exposure of 2.4 X 10^{21} n/cm². Since no peaks were

Fig. 3. Decay energy of reactivity equivalent tantalum and europium oxide absorber elements in an LMFBR (SNR).

TABLE IV

Material Data for Absorbers in the SNEAK Core 6A Fast Zero Power Reactor

Absorber Material	Theoretical Density, g/cm³	Attainable Relative Density, %	Melting Point, °C	Reactivity Values[a]		Relative Value per cm³ Abs.	$/lb	Relative Element Manufacturing Cost/Shutdown Action
				m$/g Abs.	m$/cm³ Abs.			
Tantalum	16.6	100	2996	~0.143	~2.38	1	91	1
Natural B_4C	2.52	~98	2450	~1.720	~4.33	1.82	4.8	2
90% enriched B_4C							3800	1.6
Eu_2O_3	8.18	~98	2000-2240	~0.705	~5.76	2.42	460	1.85

[a]1 m$ = 0.417 X 10^{-3}% $\Delta k/k$.

observed in the diffraction pattern obtained from Eu_2O_3, it appears that Eu_2O_3 had lost its crystallinity and gross damage occurred to the structure during irradiation. However, no quantitative data were given concerning the dimensional changes of the specimen resulting from irradiation. Leitten and Beaver[21] reported that europia/steel dispersions, irradiated in the ETR to ~70% europium burnup at 82°C and with a fast-neutron exposure of 5×10^{19} n/cm^2 ($E > 1$ MeV), have negligible dimensional change. These results were substantiated by observations of the conditions of the control rods in the SM-1 and SM-1A reactors after 10.5 and 30 MW·yr, respectively, which showed no indication of dimensional instability or structural change. Beaver and Martin[22] carried out irradiation tests in a thermal-neutron flux of 1×10^{14} $n/cm^2 \cdot s$ for 18 months on stainless-steel- and aluminum-base plate-type specimens containing europium sesquioxide and europium molybdate. The results are shown in Table V. The increase in thickness of the specimens due to irradiation was described as acceptable. The insignificant dimensional changes reported by the various investigators are consistent with the fact that neutron absorption by europium occurs by an (n,γ) reaction that would not normally lead to large dimensional changes. It is also of interest that reported dimensional changes are often similar in magnitude to normal measurement uncertainties for tests of these types.

In contrast to the results reported by Goltsev et al.,[20] the results reported by Martin et al.[23] indicate a high degree of crystallinity of Eu_2O_3 in both cubic and monoclinic forms after exposure to 6×10^{26} n/m^2 (>0.11 MeV) at ~700°C (1292°F). Most recently, a total of 103 Eu_2O_3 pellets of either cubic or monoclinic crystal structure, hot-pressed or sin-

tered products, were irradiated in row 8 of the Experimental Breeder Reactor II (EBR-II) to a fluence of 8×10^{25} n/m^2 (>0.11 MeV). Eighteen of the monoclinic-phase specimens were irradiated in row 2, achieving centerline temperatures up to ~1550°C (2822°F) and accumulating a total fluence of 18×10^{25} n/m^2. The results were summarized by Martin[24] and show that the hot-pressed monoclinic pellets were free of microcracks, but they contained many axial and circumferential macrocracks and generally exhibited poor physical integrity. The sintered monoclinic test pellets that were subjected to the highest level of thermally induced stress usually formed one axial macrocrack. For all types, however, the irradiation produced only small changes (<1%) in the dimensions of test pellets that permitted meaningful measurements. The current data further substantiate the results by Goltsev et al.[20] in terms of volume change.

COMPATIBILITY OF EUROPIA WITH STAINLESS-STEEL CLADDING

The absorber material in an LMFBR will be clad with the 20% cold-worked Type 316 stainless steel to protect it from attack by high-temperature sodium. Consequently, it is necessary that the compatibility of the absorber and the clad be characterized.

The main alloying components of Type 316 stainless steel are iron, chromium, nickel, molybdenum, and manganese. The standard free energies of formation of their oxides[25] are plotted in Fig. 4. The values for Eu_2O_3 are extrapolated from the data reported by Pasto.[9] It is important to note that the free energy of formation per oxygen atom for Eu_2O_3 is far more negative than those for the oxides of

TABLE V

Irradiation Test Results on Stainless-Steel- and Aluminum-Base Plate Specimens
Containing Europium Sesquioxide and Molybdate

Type of Dispersion	Thermal-Neutron Absorptions, $n/cm^3 \times 10^{20}$	Increase in Thickness, %
20 wt% Eu_2O_3 in Type 304 stainless steel[a]	26	0.2
	41	0.3
30 wt% Eu_2O_3 in Type 304 stainless steel	18	0.2
	57	0.1
40 wt% Eu_2O_3 in Type 304 stainless steel	40	0.2
	64	0.2
59 wt% Eu_2O_3 in Type 101 aluminum	16	0.2
	41	0.5
65 wt% $Eu_{5.3}MoO_{11}$ in Type 101 aluminum	29	0.9

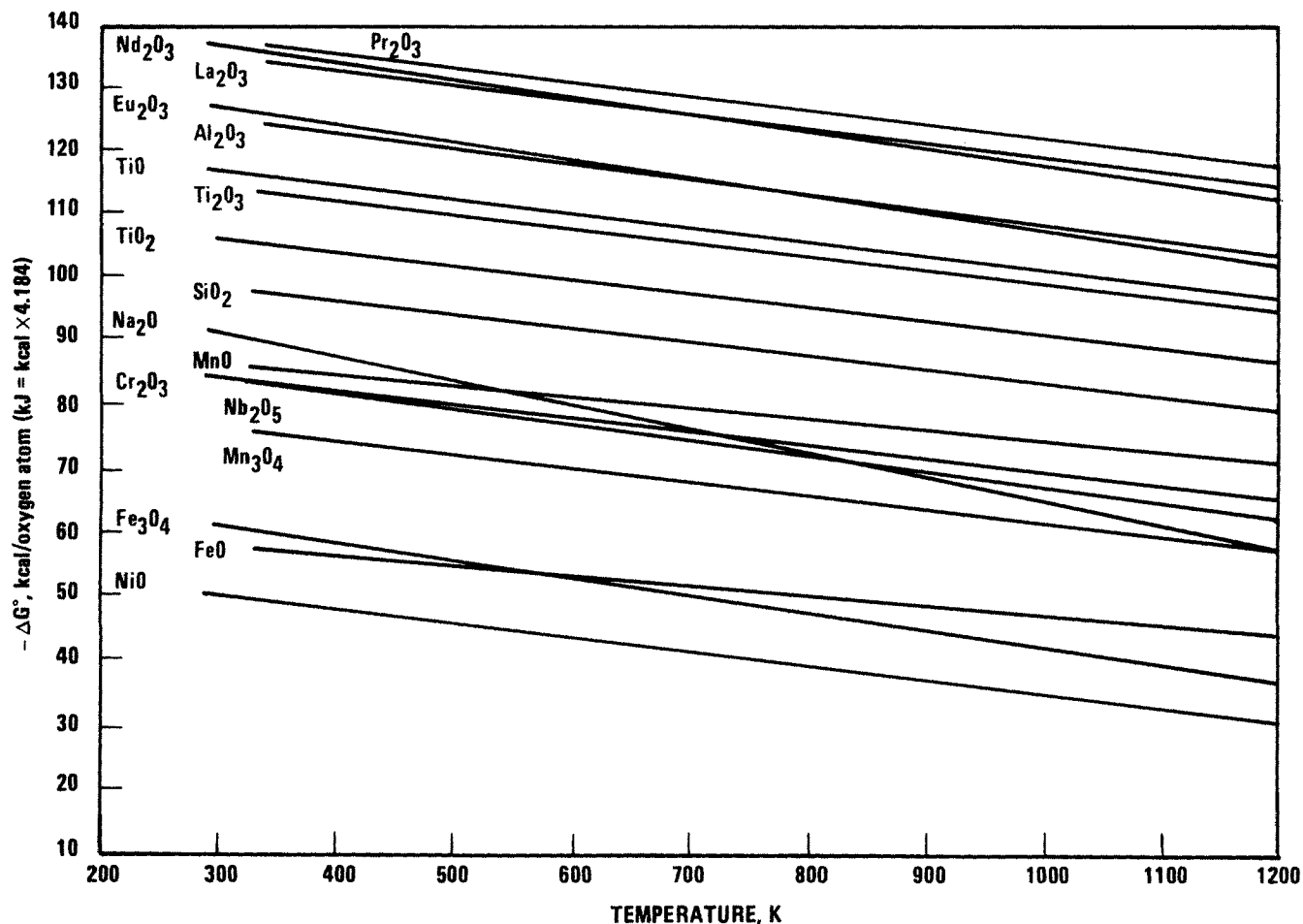[a]Silicon content in stainless steel <0.03 wt%.

Fig. 4.   Standard free energy of formation of selected oxides.

chromium, manganese, iron, and nickel. Consequently, the free energy change for Reaction (1) will be positive,

$$2M + Eu_2O_3 \rightarrow M_2O_3 + 2Eu \quad , \qquad (1)$$
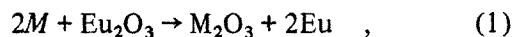
where M represents chromium, manganese, iron, molybdenum, and nickel, respectively. Therefore, reduction of Eu_2O_3 by major alloying elements in the cladding will not occur.

The free energy change of Reaction (2) is not known.

$$M_2O_3 + Eu_2O_3 \rightarrow 2EuMO_3 \quad . \qquad (2)$$

However, negative free energies at temperatures of $\sim$1000°C (1832°F) can be inferred for iron, chromium, and molybdenum because compounds such as $EuCrO_3$, $EuFeO_3$, and $EuMoO_3$ have been prepared at these temperatures.[26,27] In addition, the presence of $EuCrO_3$ in the Eu_2O_3-Type 316 stainless-steel reaction product formed at 870°C (1598°F) was also reported by Martin.[28]

The compatibility of Eu_2O_3 with Type 316 stainless-steel cladding has not been well defined. Forma-

tion of a silicon-containing europium compound at the reaction interface between Eu_2O_3 and the alloy at 900 to 1250°C (1652 to 2282°F) was first reported by Leitten.[29] A similar reaction between Eu_2O_3 and Type 304 stainless steel at 1150 and/or 1200°C (2102 and/or 2192°F) was reported by Hoyt.[30] Intergranular penetration of the Type 316 stainless steel by Eu_2O_3 was also reported by Martin[28] and by DiStefano.[31] However, the reaction product has not been characterized.

Europium is known to form various divalent europium silicates.[32] Formation of trivalent europium silicate with stoichiometry such as Eu_2SiO_5 has never been reported. However, because SiO_2 is more acidic with respect to Eu_2O_3, the formation of a double oxide such as Eu_2SiO_5 may be expected. Recently, Wu[33] reported that the x-ray diffraction analyses of the scrapings obtained from the Eu_2O_3-Type 316 stainless-steel reaction band show the presence of an unknown phase, having a Bragg reflection with an interatomic spacing of 38.2 nm (3.82 Å). This could not be accounted for on the basis of the divalent europium silicates and all the known phases, including the carbides normally present in the Type 316

stainless steel, and it appears to suggest the possibility that the reaction product might be Eu_2SiO_5 or a compound with similar stoichiometry. However, further study is necessary to substantiate this speculation.

Based on the information available to date, it can be concluded that Eu_2O_3 does react with the prototypic reference cladding alloy, 20% cold-worked Type 316 stainless steel, for the FFTF and CRBRP reactors at temperatures above 870°C. The main reaction product was identified as an europium silicate containing little or no alloying components such as iron, chromium, and nickel of the cladding alloy. However, the exact stoichiometry of this compound is not known. Consequently, further studies are necessary to characterize the reaction product, and detailed kinetic studies must be carried out to determine the reaction rate at the anticipated control rods operating temperatures, 870 to 1100°C (1598 to 2012°F), for these reactors to estimate the lifetime of the control rods for a safe reactor operation.

COMPATIBILITY OF EUROPIA WITH LIQUID SODIUM

Due to the severe conditions involved in the operation of the LMFBRs, the implications of cladding failures need to be studied. Therefore, it is important to characterize the interactions between the absorbers and the sodium coolant. Unfortunately, there was limited information available concerning the compatibility of Eu_2O_3 in liquid sodium. Based on thermodynamic considerations, Wu[8] concluded that reduction of Eu_2O_3 by liquid sodium should not occur at temperatures up to 1100°C because Eu_2O_3 is thermodynamically more stable than Na_2O. The possibility of Eu_2O_3 to form a double oxide with sodium in this temperature range is also very small, because the oxides, Eu_2O_3 and Na_2O, are both basic. Since europium has two valence states, Eu^{+2}, and Eu^{+3}, it is reasonable to expect that the lower valence state, Eu^{+2}, is more stable in the presence of a strong reducing agent such as sodium. Therefore, it is quite possible that Eu_2O_3 may be reduced to Eu_3O_4 or EuO in high-temperature sodium. Recent study by DiStefano[31] substantiated this speculation and reported the presence of Eu_3O_4 along with an unidentified face-centered cubic phase [lattice parameter a = 49.4 nm (4.94 Å)] in the reaction product of Eu_2O_3 and sodium at 650 and 760°C. In addition, he observed that all Eu_2O_3 samples were black, gained weight (due to sodium penetration) and swelled slightly (<1% diametral increase) as a result of the sodium exposure. The greatest amount of penetration occurred in cold-pressed monoclinic or hot-pressed cubic samples.

FABRICATION OF EUROPIA-CONTAINING NEUTRON ABSORBER COMPONENTS

Almost all of the Eu_2O_3-stainless-steel cermet neutron absorber elements used to date have been fabricated by dispersing the Eu_2O_3 particles in a stainless-steel matrix. These materials have been successfully used in the "SM" and "PM" reactor series sponsored by the U.S. Army. A condensed process diagram for these components summarized by Ray[10] is given in Table VI. The reason for using iron, chromium, and nickel powder instead of pre-alloyed stainless-steel powder as the matrix is to prevent the interaction of Eu_2O_3 with silicon, which is present in normal grade stainless steels. Mechanical properties of europia dispersions are not well known. The tensile properties of some selected lanthanon oxide dispersions were also summarized by Ray.[10]

The dispersion type absorbing materials for the control rods of thermal reactors were first reported by Nosov et al.[34] However, Potter et al.[35] found that additions of 15 wt% MoO_3 or WO_3 to Eu_2O_3 stabilize the Eu_2O_3 against hydration in pressurized water. They also reported that the molybdate is similar to oxide with regard to matrix compatibility, but the tungstate can be used with pre-alloyed powders that contain silicon. The superior crushing strengths of these compounds are also important from the standpoint of fabrication as described by Ray.[10] In Table VI, some characteristics of europium double oxides are compared with those of Eu_2O_3. It is noted that the europium content in these double oxides is consistently lower than that in the oxide. Consequently, higher concentrations of these complex compounds are required to achieve a given nuclear worth than is necessary with the oxide.

CONCLUSIONS

Based on the information reported here, several conclusions are made with respect to the assessment of Eu_2O_3 as an alternate to B_4C as a control material for fast reactors.

1. Europium is the best neutron absorber among the lanthanons because it has a number of isotopes that have large neutron capture cross sections. In addition, its decay product, gadolinium, also has a high capture cross section.

2. Eu_2O_3 has more europium atoms per unit volume, and is thermodynamically more stable, than europium metal. Hence, Eu_2O_3 is preferred for use as the control material. The trivalent europium compound is utilized to prevent the volume contraction that would be induced if a divalent europium compound is used.

TABLE VI

Condensed Process Outline for Hot-Rolled Stainless-Steel-Eu_2O_3 Control Rod Plate Assemblies

```
┌─────────────────────┐   ┌──────────────────────────────────────┐   ┌─────────────────────┐
│ Type 347 stainless- │   │ Blend of 71 Fe–18 Cr–11 Ni, powders  │   │   Eu₂O₃ particles   │
│  steel coverplated  │   │            (325 mesh)                │   │     (–325 mesh)     │
│       frames        │   └──────────────────────────────────────┘   └─────────────────────┘
└─────────────────────┘                    │                                    │
                         ┌──────────────────────────────────────┐   ┌─────────────────────┐
                         │          Cold press at 31 tsi         │   │ Blend Eu₂O₃ Fe, Cr, Ni │
                         └──────────────────────────────────────┘   └─────────────────────┘
                                           │                                    │
                         ┌──────────────────────────────────────┐   ┌─────────────────────┐
                         │     Dry H₂ sinter 1 h at 2100°F       │   │   Cold press at 10 tsi │
                         └──────────────────────────────────────┘   └─────────────────────┘
                                           │                                    │
                         ┌──────────────────────────────────────┐   ┌─────────────────────┐
                         │      Roll to 0.005-in.-thick foil     │   │  Dry H₂ sinter 1.5 h  │
                         └──────────────────────────────────────┘   │      at 2250°F        │
                                                                     └─────────────────────┘
                                                                                 │
                                                                     ┌─────────────────────┐
                                                                     │     Coin at 31 tsi    │
                                                                     └─────────────────────┘
                                                                                 │
                                                                     ┌─────────────────────┐
                                                                     │ Dry H₂ resinter 1.5 + h │
                                                                     │      at 2250°F        │
                                                                     └─────────────────────┘
```

Type 347 stainless-steel coverplated frames

Blend of 71 Fe–18 Cr–11 Ni, powders (325 mesh)

Cold press at 31 tsi

Dry H_2 sinter 1 h at 2100°F

Roll to 0.005-in.-thick foil

Eu_2O_3 particles (–325 mesh)

Blend Eu_2O_3 Fe, Cr, Ni

Cold press at 10 tsi

Dry H_2 sinter 1.5 h at 2250°F

Coin at 31 tsi

Dry H_2 resinter 1.5 + h at 2250°F

Stack three dispersion compacts in rolling pack frame separated by foils

Weld coverplates in place evacuate

Seal off, preheat at 2100°F

Hot roll (10% reduction per pass) from 1.64 to 0.156 in. thick

Pickle surface in H_2O–15% NHO_3–5% HF

Jig anneal in dry H_2 for 2 h at 1832°F to flatten

Shear and machine to size

Assemble control rod in jig

TIG weld assembly

Clean and inspect

3. Eu_2O_3 has two crystal structures: the low-temperature bcc form and the high-temperature monoclinic form. Since the latter structure is insensitive to thermal cycling and also has a higher density than the cubic form, the monoclinic Eu_2O_3 should be used from the standpoint of nuclear worth.

4. From the consideration of reactivity worth, based on limited experimental data, it appears that Eu_2O_3 is superior to tantalum and at least comparable to natural B_4C.

5. Europium absorbs neutrons principally by an (n, γ) reaction and, therefore, gas release, particularly helium and radioactive tritium, is not a problem. Consequently, thinner clad and larger Eu_2O_3 volume fractions can be obtained per absorber.

6. Fast-neutron (>0.11-MeV) fluence of up to 8×10^{25} or with accumulated fast-neutron fluence of up to 18×10^{25} n/m^2 produced no significant swelling of Eu_2O_3. No microcracking was observed, while the macrocracking that occurred during irradiation resulted from thermal stresses.

7. At temperatures above $870°C$, Eu_2O_3 does react with the prototypic reference cladding alloy, 20% cold-worked Type 316 stainless steel, for the FTR and CRBRP reactors. The main reaction product was identified to be a europium silicate with little or no alloying components such as iron, chromium, and nickel. Consequently, low silicon Type 316 stainless steel is recommended as cladding alloy for Eu_2O_3 absorbers. Alternatively, a "stabilized" oxide approaching (for example) the titanate composition can be used with some sacrifice in nuclear worth.

8. Sodium penetration of Eu_2O_3 was observed. However, the pellets maintained their physical integrity, and no significant attack of europia by sodium was reported. Reduction of Eu_2O_3 to Eu_3O_4 by liquid sodium was also verified.

ACKNOWLEDGMENTS

REFERENCES

1. R. VAN HOUTEN, "Fast Breeder Reactor Control, Shield, and Reflector Materials Development," GEMP-723, General Electric Company (1970).

2. G. L. COPELAND et al., "Evaluation of Fast-Reactor-Irradiated Boron Carbide Powders," ORNL-TM-3729, Oak Ridge National Laboratory (1972).

3. R. G. GRAY and L. R. LYNAM, "Irradiation Behavior of Bulk B_4C + B_4C-SiC Burnable Poison Plates," WAPD-261, Westinghouse Atomic Power Division (1963).

4. C. K. FRANKLIN et al., "Effects of Irradiation on the Mechanical Properties of Tantalum," BMI-1476, Battelle Memorial Institute (1960).

5. T. T. CLAUDSON and H. J. PESSL, "Irradiation Effects of High Temperature Reactor Structural Materials," BNWL-23, Battelle Northwest Laboratories (1965).

6. "FFTF Monthly Progress Report for April 1969," BNWL-1062, p. 4.42, Battelle Northwest Laboratories (1969).

7. W. H. HANNUM and L. D. KIRKBRIDE, "The Molten Plutonium Burn-Up Experiment," LA-3384-MS, Los Alamos Scientific Laboratory (1966).

8. P. C. S. WU, "EUROPIA as Nuclear Control Material," WARD-292, Westinghouse Advanced Reactors Division (1973).

9. A. E. PASTO, "Europium Oxide as a Potential LMFBR Control Material," ORNL-TM-4226, Oak Ridge National Laboratory (1973).

10. W. E. RAY, "The Lanthanons as Nuclear Control Materials," *Nucl. Eng. Des.*, **17**, 337 (1971).

11. H. E. STEVENS, "Nuclear Requirements for Control Materials," *Nucl. Sci. Eng.*, **4**, 373 (1958).

12. O. D. McMASTERS and K. A. GSCHNEIDNER, Jr., "Rare Earth Intermetallic Compounds," in *Compounds of Interest in Nuclear Reactor Technology*, IMD Special Report No. 13, American Institute of Mining, Metallurgical, and Petroleum Engineers (1964).

13. R. P. ELLIOT, *Constitution of Binary Alloys*, 1st suppl., McGraw-Hill Book Company, New York (1965).

14. W. V. CUMMINGS, "Irradiation Effect in Some Crystalline Ceramics," in *Advances in X-Ray Analysis*, Vol. II, pp. 418, J. B. NEWKIRK, G. R. MALLET, and H. G. PFEIFFER, Eds., Plenum Press, New York (1968).

15. K. A. GSCHNEIDNER, Jr., "On the Valences of Europium and Ytterbium in Compounds," *J. Less Comm. Met.*, **17**, 13 (1969).

16. N. I. IGNATEVA and V. G. BAMBUROV, "Thermal Behavior of Europium Oxides," *Itv. Akad. Nauk SSR, Neorg, Mater.*, **6**, 154 (1970).

17. W. A. ROSS et al., "Fabrication and Characterization of Specimens for Absorber Materials Irradiation Tests—Europium Oxide," Monthly Technical Progress Report, Hanford Engineering Development Laboratory (Sep. 1972).

18. VON H. SPENKE, "Eignung von Europium also Absorbed Material in Schnellen Reactors," *Atomwirtschaft*, 161 (May 1972).

19. T. A. PITTERLE, Westinghouse Advanced Reactors Division, Private Communication (1973).

20. V. P. GOLTSEV et al., "Radiation Resistance of Absorber Materials for Nuclear Reactors," CONF-710901-480, U.S. Atomic Energy Commission (June 1971).

21. C. F. LEITTEN, Jr. and R. J. BEAVER, "Use of Lanthanide Oxide Neutron Absorbers in Pressurized Water Reactors," *Nucl. Appl.*, 4, 399 (1968).

22. R. J. BEAVER and M. M. MARTIN, "The Status of Europium Compounds for Reactivity Control in Nuclear Reactors," ORNL-4369, Oak Ridge National Laboratory (Feb. 1969).

23. M. M. MARTIN et al., "Irradiation Behavior of Eu_2O_3 in EBR-II Experiment BICM-1," ORNL-5096, Oak Ridge National Laboratory (Jan. 1976).

24. M. M. MARTIN, "Performance of Eu_2O_3 in FTR Design-Oriented Irradiation Test in EBR-II," ORNL-TM-5400, Oak Ridge National Laboratory (June 1976).

25. *Free Energy of Formation or Oxides*, compiled by P. CHIOTTI and H. E. SHOEMAKER, from values taken from Bureau of Mines Bulletin 542.

26. G. J. McCARTHY, "Divalent Europium Compounds in the Systems Eu-Mo-O and Eu-W-O," *Mat. Res. Bull.*, 6, 31 (1971).

27. G. J. McCARTHY and R. D. FISHER, "System Eu-Fe-O: Compound Formation and Its Implications for Systematic Crystal Chemistry," *J. Solid State Chem.*, 4, 3, 340 (1972).

28. M. M. MARTIN, "Fuels and Materials Development Program Quarterly Progress Report, Sep. 30, 1972," ORNL-TM-4055, Oak Ridge National Laboratory (1972).

29. C. F. LEITTEN, "The Stability of Europium Oxide in Silicon-Bearing Stainless Steel," ORNL-2946, Oak Ridge National Laboratory (1960).

30. E. W. HOYT, "Rare Earth Oxides and Rare Earth Borates: Corrosion, Compatibility, and Radiation Effects," GEAP-3909, General Electric Company (1962).

31. J. R. DiSTEFANO, "Compatibility of Eu_3O_3 with Type 316 SS and Sodium," ORNL-TM-4780, Oak Ridge National Laboratory (1975).

32. BONDAR, TOROPOV, and KOROLEVA, "Synthesis of Silicates of Divalent Rare Earth Elements," *Inorg. Mater.*, 1, 4, 512 (1965).

33. PAUL C. S. WU, "Reaction of Europia with Austenitic Stainless Steel," *Nucl. Technol.*, 29, 215 (1976).

34. V. I. NOSOV et al., "Dispersion Type Absorbing Materials for the Control Rods of Thermal Reactors," *Proc. Conf. Physics and Materials Problems of Reactor Control Rods*, International Atomic Energy Agency, Vienna (1964).

35. R. A. POTTER, R. E. McDONALD, and C. F. LEITTEN, Jr., "Preparation and Properties of Lanthanon Molybdate and Tungstates," in *Compounds of Interest in Nuclear Reactor Technology*, IMD Special Report No. 13, p. 547, J. T. WABER and P. CHIOTTI, Eds. (1964).

ANALYSIS OF FISSILE MATERIALS BY CYCLIC ACTIVATION OF DELAYED NEUTRONS

ANALYSIS

JOHN M. JAMIESON* and GEOFFREY G. EICHHOLZ
Georgia Institute of Technology, School of Nuclear Engineering
Atlanta, Georgia 30332

A method for analyzing nuclear material for different fissile nuclides by cyclic activation has been developed and tested experimentally with samples of ^{235}U and ^{239}Pu, singly and in combination.

The method of analysis is based on the differences in the abundances and half-lives of delayed neutron groups between the various fissile nuclides. The steady-state delayed neutron response to periodic activation is independent of activation cycle period at short periods, decreases exponentially with period at long periods, and has a break point, or knee, where the response changes from constant to exponential, or from one exponential to another, with greater slope for each characteristic emitter present. The activation cycle periods at which these break points occur, the slopes of the exponential fall-off or response with cycle period between break points, and the absolute magnitude of the response at any cycle period are all functions of the effective half-lives and abundances of the delayed neutron precursors activated, so, consequently, the characteristic delayed neutron response as a function of activation cycle period is different for the various fissile species.

In the experiment, cyclic activation was accomplished by moving the samples containing fissile material cyclically through a thermal-neutron beam from the Georgia Tech Research Reactor, out of the beam and through a delayed neutron detector, and back through the beam, etc. The delayed neutron response was recorded at activation cycle periods ranging from 0.1 to 100 s for samples containing varying amounts of ^{235}U and ^{239}Pu. Deviations in the responses of the samples containing both ^{235}U and ^{239}Pu from the response of standards containing only ^{235}U or ^{239}Pu were determined to infer the ^{235}U- to-^{239}Pu ratio. After the ratio of the two fissile nuclides present was obtained, the delayed neutron response at short cycle periods was used to estimate the mass of each fissile nuclide present in the sample.

For samples containing about a gram of fissile material, accuracies on the order of 2% for ^{235}U and 4% for ^{239}Pu could be obtained for 1.5-h experiment run times when the fissile nuclides were present in about equal portions. Accuracies were dependent on the ^{235}U-to-^{239}Pu ratio and on the total mass of fissile materials present.

INTRODUCTION

Analysis of fissile nuclide content is important in nuclear operations in both fresh and spent fuel to determine as accurately as possible the initial and residual concentrations both for safeguards and criticality considerations, and for accounting purposes on a valuable and economically important resource material. Such analyses may be by element or by isotope, they may be continuous or on a selected batch basis, and they may be averaged over a substantial volume or be related to a well-defined area or thickness layer. The precision attainable and the analytical accuracy for most existing methods are probably adequate for fresh fuel analyses, but for rapid analyses of spent fuel, which have to be nondestructive and sensitive enough to give indications of minor deficiencies or diversions, present methods are only marginally adequate and the search for new or improved methods continues.[1]

---

*Present address: Technical Analysis Corporation, Atlanta, Georgia 30342.

The methods used to assay special nuclear material should incorporate several characteristics.[2] Ideally, an assay should be fast and accurate. Time is essential in process control situations, and quick detection of a diversion is necessary for credible safeguards. Unfortunately, speed and accuracy are sometimes mutually incompatible parameters. For methods where accuracy is dependent on counting statistics, longer counts usually mean better accuracy per sample but may mean that fewer samples can be taken of a given process or shipment. Insensitivity to self-shielding effects is important when nuclear materials may be hidden by the finite thickness of the sample. In some applications, such as spent fuel elements, the assay system must tolerate intense gamma-ray fields. Some situations, such as analysis of fresh fuel elements, require a nondestructive assay method if a substantial part of the throughput is to be measured. Nondestructive analysis is also often desirable to decrease sampling problems by allowing a larger fraction of the material flow to be assayed.

The accuracy with which material flow can be measured is limited in many instances by sampling biases. Solids often are found to be not homogeneous in isotopic makeup or particle size; liquids, particularly solutions of plutonium, contain suspended or settled-out solids or sludge.[3] Methods that infer the compositions of large volumes of materials from small samples suffer the most from sampling problems. Some materials, such as pellets inside assembled fuel elements, cannot be sampled in practice.

In a closed materials balance for safeguards accountability, all materials moving into and out of each step in the nuclear fuel cycle must be measured; any discrepancy, called *material unaccounted for* (MUF), represents material lost (or gained) by unknown channels, or material that may have been diverted.[3] The assay method discussed in the following is a candidate for use in a closed materials balance where more than one fissionable isotope is present, such as plutonium recycle fuel, light water reactor discharge fuel, high-temperature gas-cooled reactor (HTGR) fuel, where ^{233}U and ^{235}U can be found together, fuel refabrication, and reprocessing waste. It may also be used in conjunction with another method, such as calorimetry, where precise knowledge of the ratio of two fissile isotopes can improve the accuracy of another measurement.

The method that is described here is based on cyclic excitation of delayed neutrons by thermal neutrons from a neutron source, such as a nuclear reactor.[4] These delayed neutrons are characteristic of the fiss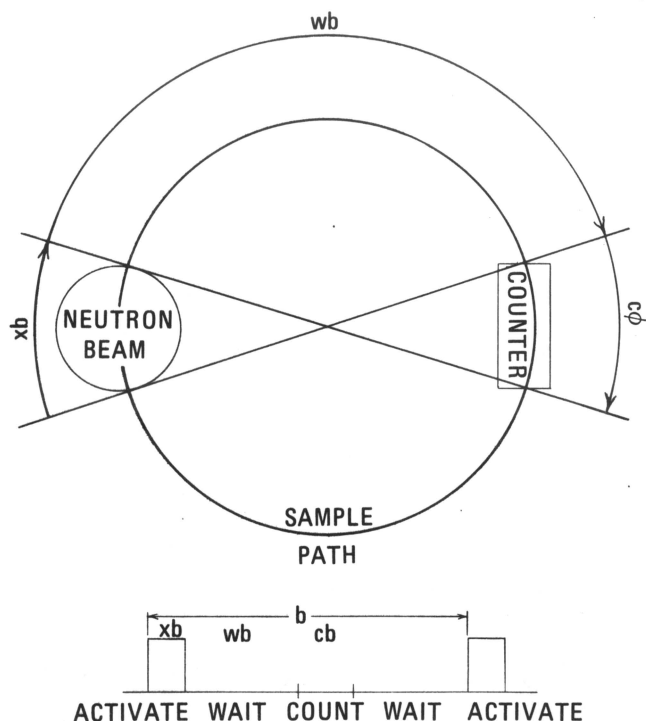ile nuclides and can be used to determine the fissile composition with respect to ^{235}U and/or ^{239}Pu in the test sample. Delayed neutrons are produced when a member of a fission product decay chain decays to an energy level for a nuclide whose excitation energy is greater than the binding energy of a neutron. The half-lives, decay constants, and yields of delayed neutrons from fission events induced by thermal and fast neutrons for the more important fissile nuclides have been presented by Keepin.[5] The neutrons can be assumed to die away as a linear superposition of exponential decays. If a least-squares fitting to delayed neutron data is done, it is seen that six exponential periods, neither less nor more, generate a good fit for fissioning materials.[6] It is also found that variations in group yields are much greater than the variations among group periods for the isotopes considered. The total delayed neutron yield increases with neutron-proton difference for a given fissioning nuclide due, primarily, to short-half-life groups; it also generally decreases with atomic number.[2] It is these variations that are the basis of the particular method described here.

When fissions are induced in a sample by repeated activation at a variable period, the steady-state delayed neutron response is independent of activation cycle period at short periods, decreases exponentially with period at long periods, and has break points where the response changes from constant to exponential or from one exponential to another for each delayed neutron emitter present. Consequently, a time- or period-dependent activity plot can be obtained that is characteristic of the particular fissile composition of the sample; in the present context, this is referred to as the "signature" of the sample.[7,8]

EXPERIMENTAL DETAILS

In the work reported here, cyclic activation was achieved by moving the sample rather than chopping the neutron beam. Disk or foil samples were moved on a circular path through the neutron beam. Figure 1 shows the sample path and the timing sequence for activation and activity detection for an arbitrary cycle period. The total steady-state delayed neutron response as a function of cycle time is

$$\frac{\lambda N_{ss}}{\phi \sigma P} = \sum_{i=1}^{n} \frac{[1 - \exp(-\lambda_i bx)] \, [\exp(-\lambda_i bw)] \, [\exp(-\lambda_i bc) - 1] \, [1 - \exp(-\lambda_i bw)]}{\lambda_i b \, [1 - \exp(-\lambda_i b)]} \quad ,$$

where

λ_i = i'th delayed neutron decay constant

n = total number of delayed neutron decay constants

ϕ = neutron flux in the beam

σ = fission cross section for producing this delayed neutron

Fig. 1.   Sample path and timing sequence for activation of sample in a neutron beam and detection of delayed neutron activity.

Fig. 2.   Drawing of detectors, moderator, and shield. (Entire assembly, including sample slot, was sheathed in cadmium. Dimensions in millimetres.)

P = parent atom concentration (assumed constant)

N_{ss} = steady-state concentration of activated daughter atoms of interest

b = cycle period

x = portion of a cycle spent in the beam

w = portion of a cycle between activation and counting

c = portion of a cycle spent counting.

Having established that the response to a cyclic activation as a function of cycle period is determined by the activation products and is different for different abundances and half-lives of the activation products, we devised an experiment to find the composition of samples containing various proportions of ^{235}U and ^{239}Pu. Similar experiments have been done at Los Alamos Scientific Laboratory using fast neutrons for activation and inferring sample composition from delayed neutron response at two times after an interrogation pulse in a cycle that was long compared to the half-lives of the delayed neutron groups.[9]

A linear servo-amplifier controlled the speed of a motor and gear train driving the sample holder in a circular path through the neutron beam and the
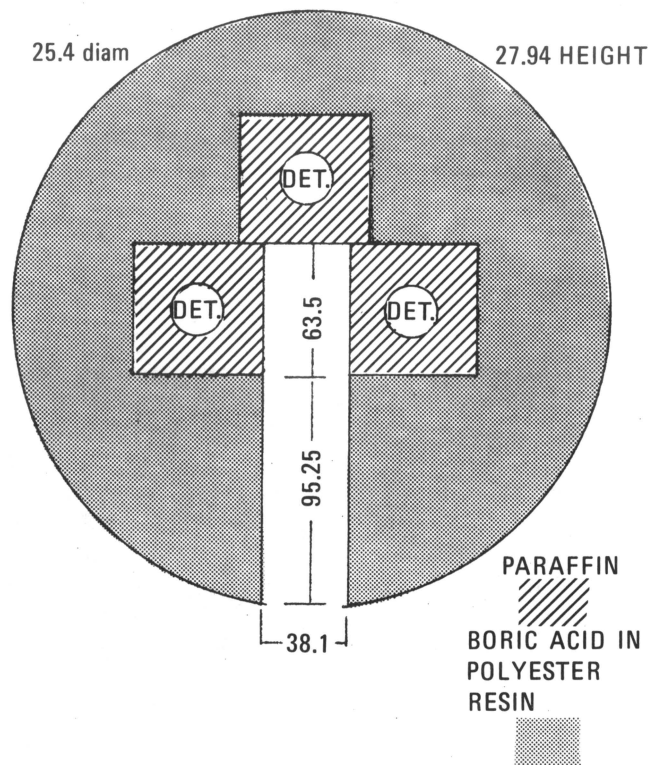
detector at cycle periods adjustable between 0.10 and 150.0 s. The neutron beam intensity was $\sim 5 \times 10^8$ n/cm²·s. Figure 2 is a diagram of the detector assembly that consists of three BF_3 detectors in a paraffin moderator surrounded by a boric acid-in-polyester-resin shield. There was a channel in the shield to allow the sample to swing into the active region of the moderator. The entire assembly including the sample channel was encased in a sheet of cadmium to exclude the thermal-neutron background, while admitting epithermal delayed neutrons into the moderator. Gating the detector on only during the time that a sample was in the active region helped hold the background to a few counts per second. The samples were made up of foils of uranium and plutonium (the plutonium foils were sheathed in stainless steel) and were arranged on the sample arm to prevent shielding of one foil by another.

The data collected by recording the steady-state delayed neutron response at various frequencies of sample rotation, with periods ranging from 0.1 to 100.0 s, were analyzed for sample content of ^{239}Pu and ^{235}U by comparing sample data with data collected using foils containing only ^{235}U or only ^{239}Pu rather than trying to unfold the delayed neutron

group half-lives and abundances from the sample data alone.

Using thermal neutrons for activation resulted in high reaction rates with the intense reactor source available and the high cross sections for thermal neutrons, although it also resulted in considerable self-shielding. The technique of analyzing unknown samples by comparison with dimensionally similar known samples made it possible to incorporate the self-shielding factors in the physical experiment rather than having to calculate them in the analysis of the data.

Figure 3 shows a typical set of data plotted on log-log axes and normalized to one at short activation periods. Because ^{239}Pu has a greater ratio of long-to-short half-life delayed neutrons than ^{235}U, at cycle periods between 0.1 and 100 s the curves of normalized delayed neutron activity as a function of cycle period (signatures) of samples containing ^{235}U were, within statistical deviations, less than or equal to the signature of ^{239}Pu alone. Overlap of the curves occurs only at short periods where the response is saturated, that is, the delayed neutron response does not show a dependence on cycle frequency, and for long cycle periods where differences are lost in the statistics of small response. Similarly, samples containing ^{239}Pu always, in the range of cycle periods of interest, yielded normalized curves that were greater than or equal to the normalized curve of samples containing ^{235}U alone. These differences reflect the number of delayed neutrons contributed to the total delayed neutron response by each of the two fissioning nuclides in the sample. Figure 4 is a plot of the differences between the delayed neutron signatures of three samples containing ^{239}Pu and the signature of ^{235}U. The area under these curves was used to find the atom ratio of plutonium to uranium.

At short cycle periods, all of the delayed neutron groups contribute to the delayed neutron response, so the short-period, high-frequency response is proportional to the quantity of fissioning nuclides in the sample, the total abundance of delayed neutrons, and the self-shielding factor. Since we took our reference curves from known samples physically similar to our unknowns, our normalization factor for delayed neutron signatures was of the form response per gram, and total delayed neutron abundance and self-shielding factors were not necessary to deduce the quantity of fissioning nuclides present in the sample. With the normalization factor for a sample and the ratio of uranium to plutonium calculated from the differences in signatures, it was possible to estimate the total mass of uranium and plutonium in the sample.

Analyzing samples containing about a gram of fissionable material and count times of 100 s per point for 50 different cycle frequencies led to nor-
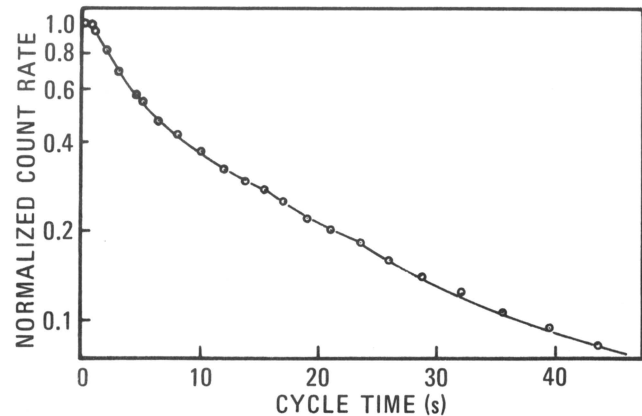

Fig. 3. Delayed neutron count rate versus cycle period for ^{239}Pu, normalized to 1.0 at short cycle periods.
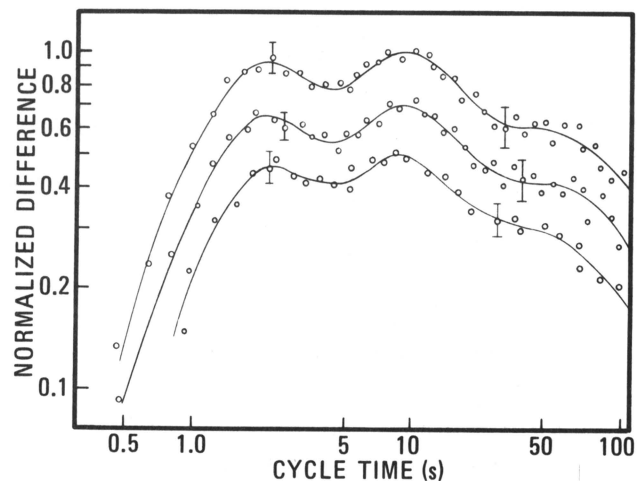

Fig. 4. Differences between the signatures of three samples containing ^{239}Pu and the signature of ^{235}U, normalized to 1.0 at the cycle period of maximum difference.

malization factors between 13 678 and 66 529, depending on sample mass and composition. About 1.5 h was needed to collect a signature for a sample.

Counting statistics play the major role in the accuracy to which an assay can be made; longer counts and larger samples yield better results.[10] With the gram-sized samples used and 1.5-h run times, we were able to deduce the uranium content of samples with an error (1 sigma) as small as 2% and the plutonium content with an error as small as 4%. Figures 5 and 6 show the accuracy of ^{235}U analysis in the presence of 0.612 g of ^{239}Pu, and ^{239}Pu analysis in the presence of ^{235}U. The solid lines in these figures have a 45-deg slope, indicating close correspondence between measured values and the actual composition of the samples. Agreement
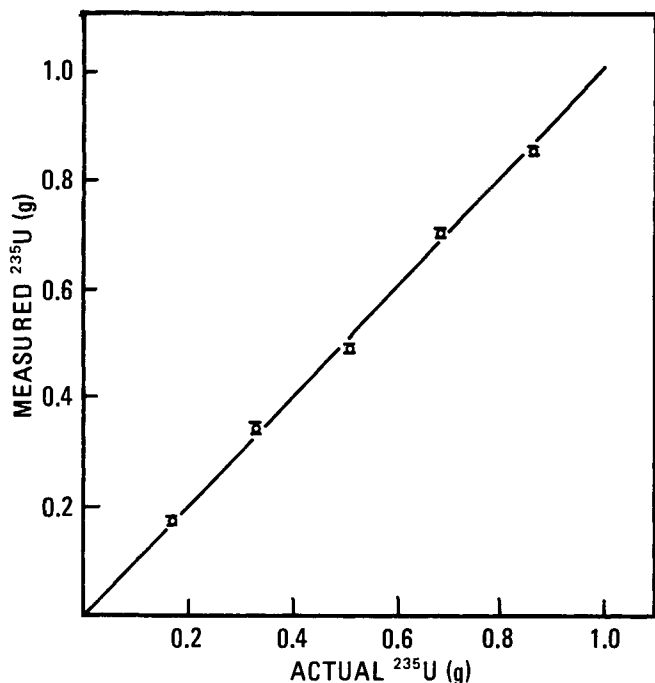
Fig. 5. Accuracy observed in the analysis of ^{235}U in the presence of 0.150 g of ^{239}Pu. The solid line with the 45-deg slope indicates perfect correspondence between measured values and actual sample composition. Error bars indicate the standard deviation expected from statistical considerations.
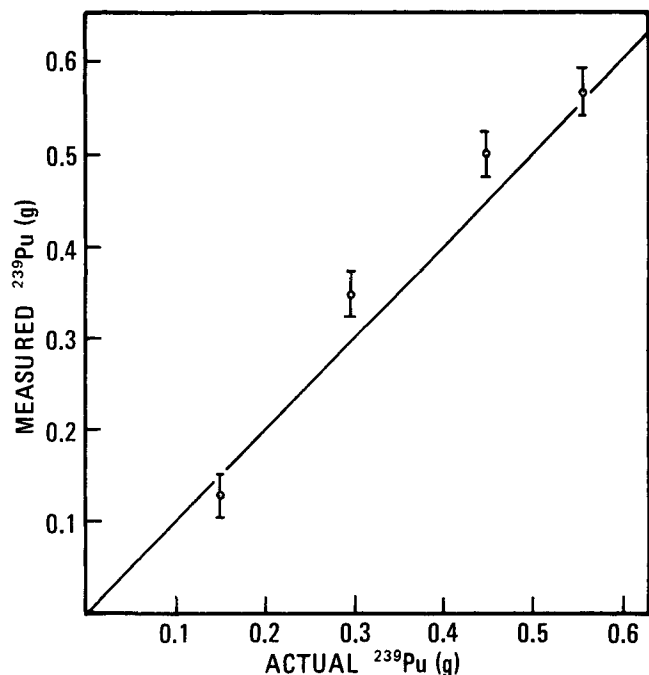

Fig. 6. Accuracy observed in the analysis of ^{239}Pu in the presence of 0.8665 g of ^{235}U. The solid line with the 45-deg slope indicates perfect correspondence between measured values and actual sample composition. Error bars indicate the standard deviation expected from statistical considerations.

between the points and solid line shows good linearity of the method and scatter shows decreased accuracy for smaller samples and for increased percentages of interfering fissioning isotopes, ^{235}U in the assay of ^{239}Pu and ^{239}Pu in the assay of ^{235}U. As expected, errors tend to be proportional to the square root of the delayed neutron response.

CONCLUSIONS

The method described appears to have certain advantages over other interrogative, nondestructive methods. By detecting delayed neutrons, it largely overcomes the problems arising from high gamma-ray intensities associated with spent fuel elements or stationary neutron sources.[11] To be a practical device, further engineering development will be required to provide for oscillatory motion of fuel elements or for use of pulsed neutron sources and detectors. Source intensity will be a limiting factor. Although portable sources such as ^{252}Cf are available,[11] it may be preferable for fuel safeguards analyses at the power plant to derive an interruptable neutron beam from the power reactor for this purpose. Such a method would be capable of higher sensitivity than photoneutron methods[12] or spectrography on induced fission product gamma radiation. It can be automated fairly easily by means of a small, dedicated on-line computer.

REFERENCES

1. "Safeguarding Nuclear Materials," *Proc. Vienna Symp. 1975*, International Atomic Energy Agency, Vienna (1976).

2. G. R. KEEPIN, "Non-Destructive Detection, Identification and Analysis of Fissionable Material," LA-3741, Los Alamos Scientific Laboratory (1967).

3. F. X. HAAS and W. W. STROHM, "Gamma-Ray Spectrometry for Calorimetric Assay of Plutonium Fuels," *IEEE Trans. Nucl. Sci.*, NS-22, 734 (1975).

4. J. M. JAMIESON, "Analysis of Fissionable Material by Delayed Emissions," Thesis, Georgia Institute of Technology, Atlanta (1976).

5. G. R. KEEPIN, *Physics of Nuclear Kinetics*, Addison-Wesley Publishing Co., Inc., Reading, Massachusetts (1965).

6. G. R. KEEPIN, T. F. WIMETT, and K. R. ZIEGLER, "Delayed Neutrons from Fissionable Isotopes of Uranium, Plutonium and Thorium," *Phys. Rev.*, 107, 1044 (1957).

7. W. W. GIVENS, W. R. MILLS, Jr., and R. L. CALDWELL, "Cyclic Activation Analysis," *Proc. Int. Conf. Modern Trends of Activation Analysis*, p. 139 (1968).

8. J. M. JAMIESON and G. G. EICHHOLZ, "Analysis of Fissile Material by Cyclic Activation of Delayed Neutrons," *Trans. Am. Nucl. Soc.*, 23, 96 (1976).

9. C. N. HENRY, H. O. MENLOVE, and R. H. AUGUSTON, "Delayed Neutron Kinetic Response Methods for Nonde-structive Analysis of Reactor Fuel Elements," CA-DC-9758, Los Alamos Scientific Laboratory (1967).

10. J. L. JAECH, "Case Studies on the Statistical Analysis of Safeguards Data," *Proc. Vienna Symp. 1975*, International Atomic Energy Agency, Vienna (1976).

11. H. O. MENLOVE, R. A. FORSTER, J. L. PARKER, and D. B. SMITH, "CF-252 Assay System for FBR Fuel Pins," LA-5071-M, Los Alamos Scientific Laboratory (1972).

12. G. L. RAGAN, R. S. BOOTH, T. J. BURNS, J. D. JEN-KINS, C. R. WEISBIN, and L. R. WILLIAMS, "System for Assay of Fissile Content of Spent LMFBR Fuel Subassem-blies," *Trans. Am. Nucl. Soc.*, 23, 95 (1976).